Analytic On-Body Antenna and Propagation Models

Von der Fakultät für Elektrotechnik und Informatik
der Gottfried Wilhelm Leibniz Universität Hannover
zur Erlangung des akademischen Grades

Doktor-Ingenieur
(abgekürzt Dr.-Ing.)

genehmigte Dissertation

von

Dipl.-Ing. Markus Grimm
geboren am 22.11.1980
in Neumünster

2019

Referent:
Prof. Dr.-Ing. Dirk Manteuffel

Korreferent:
Prof. William Scanlon

Prüfungsvorsitz:
Prof. Dr.-Ing. Stefan Zimmermann

Tag der Promotion:
07. November 2018

Abstract

The use of wireless communication technologies for the intercommunication of body-worn applications is increasing rapidly nowadays. In accordance with the ongoing miniaturization of wearable devices, the interaction between the antenna and the user becomes more and more intense. As a result of the inability of the traditional free-space antenna theory to describe the excitation of on-body surface waves, this has so far led to insufficient insights into the development of such body-centric systems. Hence, the aim of this thesis is to derive on-body antenna parameters and physically motivated EM propagation models that can be used to develop scalable path gain models as well as optimized design strategies.

Considering planar dissipative surfaces, an intuitive propagation model is discussed, which follows the classical Sommerfeld problem. An appropriate solution for quasi-static ranges is adapted and consulted to discuss basic principles of electromagnetic propagation of on-body line-of-sight scenarios for selected frequencies between 400 MHz and 60 GHz. Based on these results, an antenna de-embedding is introduced in the course of this thesis, which is capable of modeling the average radiated antenna far field. Furthermore, a decomposition of the total on-body far field into a TM field component and a TE one is discussed to define two equivalent electric dipole sources. This approach enables the definition of the on-body directivity as well as the effective antenna area to discuss the radiation properties of the corresponding antenna geometry in terms of on-body communications. While this approach is primarily limited to line-of-sight propagations, a cylindrical dielectric phantom is introduced to cover non-line-of-sight links as well. In this case, the introduced de-embedding method is used to model the quasi-static range while the bended propagation path is treated by an adapted cylindrical model, which emphasizes the TM/TE-related far field decomposition of the planar model. Finally, the theory that is derived is verified by numerical full human body examples as well as by measurement setups in an anechoic chamber.

Keywords: Body Area Networks, On-Body, Antenna Theory

Zusammenfassung

Funkapplikationen im und am Körper werden zunehmend in unterschiedlichen Lebensbereichen eingesetzt. Die fortschreitende Miniaturisierung solcher Geräte führt häufig dazu, dass der Nutzer selbst zum prägenden Teil der Funkanwendungen wird. Die primär der Körperkontur folgenden Übertragungsstrecken sind hierbei nicht durch herkömmliche Freiraumfunkfelddämpfungsmodelle nachzubilden, da der dominante Ausbreitungsmechanismus auf Oberflächenwellen zurückzuführen ist. Ziel der vorliegenden Dissertation ist die Definition adaptierter Antennenparameter und die Entwicklung skalierbarer physikalisch motivierter Kanalmodelle.

Die theoretischen Grundlagen zur Wellenausbreitung entlang ebener verlustbehafteter Grenzschichten werden durch das klassische Sommerfeldproblem eingeführt. Diesbezüglich wird eine Lösung für den quasi-stationären Funkfeldbereich aufgezeigt und zur Diskussion grundlegender elektromagnetischer Ausbreitungsphänomene im Frequenzbereich zwischen 400 MHz und 60 GHz herangezogen. Basierend hierauf wird eine Methode zum Antennen-de-embedding vorgestellt, welche die Abschätzung des durchschnittlich zu erwartenden Antennenfernfeldes ermöglicht. Des Weiteren wird das körpergebundene Fernfeld in eine TM und eine TE Komponente zerlegt, um seine Wirkung auf zwei äquivalente elektrische Dipole abzubilden. Dieser Ansatz ermöglicht die Definition von On-Body Antennenparameter, u.a. Direktivität und Antennenwirkfläche, welche zur systematischen Klassifikation körpergetragener Antennen herangezogen werden. Während dieser Ansatz hinreichend zur Beschreibung direkter Ausbreitungspfade verwendet werden kann, ist ihre Verwendung bei gekrümmten Ausbreitungspfaden durch das zugrunde gelegte ebene Modell beschränkt. Diese Limitation wird durch Einführung eines zylindrischen Phantommodells umgangen, indem das ebene Modell zur Modellierung des quasistationären Feldbereichs verwendet wird und das Zylindermodel weiter entfernte Distanzen beschreibt. Die Modellentwicklung wird hierbei komplementär zum TM/TE-Ansatz des ebenen Modells gehalten. Die gesamte Theorie wird durch numerische Ganzkörpersimulationen und Messungen in einer Antennenmesskammer verifiziert.

Schlagwörter: Körpergebundene Funknetzwerke, On-Body, Antennentheorie

Danksagung

Der Schwerpunkt der Ergebnisse dieser Dissertation wurde während meiner Tätigkeit als wissenschaftlicher Mitarbeiter an der Christian-Albrechts-Universität zu Kiel gebildet. Diese Ergebnisse konnte ich im Anschluss an der Leibniz Universität Hannover in Form der vorliegenden Dissertation zusammenfassen.

Deshalb möchte ich mich als Erstes bei Prof. Dr.-Ing. Dirk Manteuffel bedanken, da er meine Promotion im Bereich der Funkkommunikation von der Initiation in Kiel bis hin zur Finalisierung in Hannover ermöglicht hat. Ich bin sowohl für die fachlichen Diskussionen, als auch für das in mich gesetzte Vertrauen dankbar. Insbesondere möchte ich ihm jedoch für die vermittelte wissenschaftliche Methodik danken, welche weit über die Promotion hinauswirkt.

Für das Interesse an dieser Arbeit, und die Übernahme des Korreferates, möchte ich Prof. William Scanlon danken. Ebenso bin ich Prof. Dr.-Ing. Stefan Zimmermann für den Vorsitz der Prüfung dankbar.

Weiterhin möchte ich allen Arbeitskollegen in Kiel für die gute Zusammenarbeit, die angeregten Diskussionen und den fachlichen Perspektivenwechsel danken, der als Anstoß zur Lösung einiger Schlüsselsituation entscheidend beitrug. Ein ganz besonderes Dankschön gilt daher Dr.-Ing. Robert Ledig, Dr.-Ing. Yi Chen, Dr.-Ing. Eugen Safin, Dipl.-Ing. Wolfgang Taute, Dipl.-Ing. Florian Marx und M. Sc. Thade Wunderlich.

In diesem Kontext danke ich meinen Kollegen in Hannover, insbesondere für die unmittelbare und freundliche Aufnahme in ihren Reihen. Besonderer Dank gilt hierbei M. Sc. Lukas Berkelmann und M. Sc. Saba Meshksar für ihre fachlichen Anregungen.

Zudem danke ich allen Studierenden, mit denen ich zusammengearbeiteten konnte. Ihr fachlicher Wissensdrang hat meine eigene Forschung zusätzlich beflügelt.

Zuletzt gilt meinem Dank Freunden und Familie, die Rat und Ausgleich bereithielten. Herbei möchte ich meine ganz besondere Dankbarkeit gegenüber meinen Eltern, Marlies und Wolfgang Grimm, ausdrücken. Sie haben durch ihre stete Unterstützung meinen Werdegang erst ermöglicht und mir stets unersetzlichen Rückhalt geboten.

Contents

List of Author's Publications and Contributions I

List of Abbreviations X

Introduction 1

1.1 Background 1

1.2 Objective of this Work 2

1.3 Content and Organization of the Thesis 3

The Electromagnetic Field on a Dissipative Planar Dielectric Surface 7

2.1 Helmholtz Equation and Vector Potential of an Electric Source 9

2.1.1 Connection to the Hertz Vector Potential 9

2.2 Approach of Arnold Sommerfeld 10

2.2.1 General Solution by the Example of a Normally Orientated Hertzian Dipole 12

2.3 Hertzian Vector Potential 14

2.3.1 Normally Orientated Small Electric Dipole 15

2.3.2 Tangentially Orientated Small Electric Dipole 16

2.4 Calculation of the Electromagnetic Field 16

2.4.1 Approach for Quasi-Static to Far Field Ranges adapted from P. Bannister 18

2.4.2 Electromagnetic Field Quantities and Minor Reformulations 25

2.5 Separation of Wave Components 28

The Electromagnetic Field on a Dissipative Dielectric Cylinder 33

3.1 General Definitions and Denotations 34

3.1.1 Electric Field of a Line Source in Free Space 35

3.1.2 Connection between Line and Point Sources 36

3.2 Transversal Components of the Electromagnetic Field 38

3.3 Tangential Transversal Orientated Source 39

3.3.1 Incident Field Components 40

3.3.2 Scattered Field Components 40
3.3.3 Total Field Components 41
3.3.4 Coefficient Calculation by Applied Boundary Conditions 42
3.4 Tangential Longitudinal Orientated Source 43
3.4.1 Incident Field Components 44
3.4.2 Scattered Field Components 45
3.4.3 Total Field Components 45
3.4.4 Coefficient Calculation by Applied Boundary Conditions 46

Basics of Model Body-Centric Communications and Related Applications 49
4.1 Propagation Constant and Related Quantities 51
4.1.1 Connected Quantities 52
4.2 Modeling Aspects of Biological Tissues 53
4.2.1 Cole-Cole Dispersion Approximation and Gabriel Parameters 55
4.2.2 Properties of Human Dermis Tissues 56
4.3 Coordinate System 57
4.4 The FDTD Method 60
4.4.1 The Basic FDTD Algorithm 60
4.4.2 Discretization in Space 61
4.4.3 Discretization in Time 64
4.4.4 Numeric Stability and Dispersion 67
4.4.5 Anatomical Human Body Models 68
4.4.6 Vast Solution Spaces and Appropriate Boundary Conditions 69
4.4.7 End Criterion Estimation 72
4.4.8 Estimation of Memory Allocation 74

Modeling Line-of-Sight On-Body Propagations 77
5.1 The Planar Model in Relation to Full Human Body Models 80
5.1.1 Comparison between Theoretical and Numerical Models 80
5.2 Norton Surface Waves in Context of Body-Centric Applications 83
5.2.1 Applicability in Terms of Human Dermis Tissues 83
5.2.2 Numerical Distance of Fat, Muscle and Skin Tissue 84
5.2.3 Ratio of the Norton Surface Wave to the Space Wave in Relation to Tissue Type and Frequency 86
5.2.4 Ratio of the Norton Surface Wave to the Space Wave in Relation to the Effective

Antenna Height 87
5.3 Radiated Antenna Field of Body-Worn Antennas 88
5.3.1 Electric Dipole Antennas 89
5.3.2 Arbitrarily Shaped Antennas 92
5.4 On-Body Antenna Parameters 97
5.4.1 Far Field Distance 97
5.4.2 Far Field Components 97
5.4.3 Equivalent Electric Sources Approach 98
5.4.4 On-Body Directivity 101
5.4.5 On-Body Effective Antenna Area 104
5.4.6 On-Body Path Gain 104
5.4.7 Estimation of the Effective Antenna Height 105
5.4.8 Example: Antenna: Half-Wave Dipole 106
5.4.9 Example: Planar Inverted-F Antenna 111
5.5 Limitations of the Theory 114

Non-Line-of-Sight On-Body Propagations 119
6.1 The Cylindrical Model in Relation with Full Human Body Models 120
6.1.1 Comparison between Theoretical and Numerical Models 121
6.2 Modeling of the Radiated NLOS Antenna Field 123
6.2.1 Analogy Considerations in Terms of the Planar Model 123
6.2.2 Non-Line-of-Sight Far Field Model 125
6.2.3 Discussion on Channel Parameters as a Function of the Body Geometry 127
6.2.4 Example: On-Body PIFA on Human Trunk 128

Conclusion 131

Appendix

A1 Recurrence Formula of the Bessel Equation 135
B1 Gabriel Parameters of Human Body Tissues 136
C1 Ground Wave Attenuation Factors 137
D1 Recursive Field Components of the FDTD Method 140

Bibliography 142

List of Author’s Publications and Contributions

This dissertation contains textual materials and figures from the author’s publications listed below. The relevant publications are cited at corresponding passages, including captions of respective figures. The use of those materials requires the permission of the Institute of Electrical and Electronics Engineers (*IEEE*). The three key publications are:

I. **Grimm, M. and Manteuffel, D., “Norton Surface Waves in the Scope of Body Area Networks,” *Antennas and Propagation, IEEE Transactions on*, Vol. 62, No. 5, pp. 2616–2623, May 2014.**
The author was responsible for developing the idea, the numeric evaluation and content of the paper. Prof. Manteuffel supervised the work.

II. **Grimm, M. and Manteuffel, D., “Body Worn Antenna Systems for Health Care related On- and Off-body Communications,” *4th International Conference von Wireless Mobile Communication and Healthcare*, Athens, Greece, November 2014.**
The author was responsible of developing the idea, the numeric evaluation and the content of the paper. Prof. Manteuffel supervised the work.

III. **M. Grimm and D. Manteuffel, “On-Body Antenna Parameters,” in *IEEE Transactions on Antennas and Propagation*, Vol. 63, No. 12, pp. 5812–5821, December 2015.**
The author was responsible for developing the idea, the numeric evaluation and the content of the paper. Prof. Manteuffel supervised the work.

Other related publications—authored by the author of this dissertation—are [Gri10, Gri11, Gri12a, Gri12b, Gri13a, Gri13b, Gri14a, Gri15a]. They are listed in the bibliography in detail and contain preceding aspects as well as additional examples.

Remarks on Notations

Through this paper, a clear system of notations is used to clarify the usage of the equations to the reader. All scalar values are denoted with italic letters. Vectors and matrixes are denoted with bold and capital letters. Any italic subscript letter denotes a count index that is typically used within a summation. The regular subscript is used to specify the quantity.

The entire work assumes a time harmonic dependence of the form $e^{j\omega t}$ in terms of electromagnetic fields quantities and the surface currents. If the negative time convention is required, j has to be replaced by $-i$.

List of Constants

ε_0	$8.8541878176\times10^{-12}$ [As/Vm]
μ_0	$4\pi\times10^{-7}$ [Vs/Am]
π	3.14159265 [1]
η_0	376.730 [Ω]
c_0	299792458 [m/s] $\approx 3\cdot10^8$ m/s

List of Latin Symbols

a	Cylinder radius [m]
$\mathbf{A}$	Vector potential [Vs/m]
A	Bannister's electric field attenuation function [1]
$A_{\mathrm{eff,TM}}$	TM on-body effective antenna area [m^2]
$A_{\mathrm{eff,TE}}$	TE on-body effective antenna area [m^2]
A_m	Electric field scaling factors [V/m]
$\mathbf{B}$	Magnetic flux density [Vs/m^2]
B	Bannister's magnetic field attenuation function [1]
B_m	Magnetic field scaling factors [V/m]
c	Speed of light within a medium [m/s]
C_m	Electric field excitation factors [V/m]
C	Contour path variable [1]
d	Depth of the quasi-static reflection plane [m]
d_{p}	On-Body path along the body surface [m]
$\mathbf{D}$	Electric flux density [As/m^2]
D_m	Magnetic field scaling factors [V/m]
D_{TM}	TM on-body directivity [1]
D_{TE}	TE on-body directivity [1]
$\mathbf{E}$	Electric field [V/m]
E_{DW}	Direct wave component of the electric field [V/m]
E_{RW}	Reflected wave component of the electric field [V/m]
E_{SW}	Norton surface wave component of the electric field [V/m]
E_{SP}	Space wave component of the electric field [V/m]
$\mathbf{E}^{\mathrm{inc}}$	Incident electric field [V/m]

$\mathbf{E}^{\mathrm{sct}}$	Scattered electric field [V/m]
$\mathbf{E}^{\mathrm{total}}$	Total electric field [V/m]
f	Frequency [1/s]
$F(w)$	Sommerfeld's attenuation function [1]
h	Effective antenna height [m]
$\mathbf{H}$	Magnetic field [V/m]
$\mathbf{H}^{\mathrm{inc}}$	Incident magnetic field [A/m]
$\mathbf{H}^{\mathrm{sct}}$	Scattered magnetic field [A/m]
$\mathbf{H}^{\mathrm{total}}$	Total magnetic field [A/m]
I	Electric current [A]
$\mathbf{J}$	Electric surface current density [A/m^2]
k	Scalar wave number [1/m]
k_ρ	Scalar wave number in ρ-direction [1/m]
k_z	Scalar wave number in z-direction [1/m]
ℓ	Length element [m]
n	Reflection index [1]
N^{E}	Electric field attenuation factor [1]
N^{H}	Magnetic field attenuation factor [1]
p	Electric dipole momentum [Am]
$\mathbf{p}_1$	Normally orientated electric dipole [Am]
$\mathbf{p}_2$	Tangential longitudinal orientated electric dipole [Am]
$\mathbf{p}_3$	Tangential transversal orientated electric dipole [Am]
P	Norton integral [1/m]
PG	Path gain [1]
P_{rad}	Radiated power [W]
P_{RX}	Received power [W]
$\mathbf{r}$	Spatial vector pointing at the observation point [m]
$\mathbf{r}'$	Spatial vector pointing at the source [m]
R	Distance between coordinate origin and observation point [m]

R_0	Direct path [m]
R_1	Ground reflected path [m]
R_2	Image plane reflected path [m]
s_i	Weighting factor of the *i*-th cell [1]
$\mathbf{S}$	Power flux density [W/m^2]
S_1	Sommerfeld integral [1/m]
t	Time [s]
$u_{0/1}$	Sommerfeld's media functions [1/m]
$U_{1/3}$	Normalization factor [V]
w	Sommerfeld's numerical distance [1]

List of Greek Symbols

α	Attenuation constant [m^{-1}]
α_n	Gabriel parameter, dispersion width [1]
$\alpha_{\mathrm{E,TM}}$	NLOS attenuation factor of the TM electric field [1/m]
$\alpha_{\mathrm{E,TE}}$	NLOS attenuation factor of the TE electric field [1/m]
α_{S}	NLOS attenuation factor of the power flux density [1/m]
β	Phase constant [m^{-1}]
γ	Propagation constant [m^{-1}]
γ_1	Propagation constant of the ground, resp. human body [1/m]
$\Gamma_{\parallel}$	Fresnell reflection coefficient for vertical polarizations [1]
δ	Penetration depth [m]
Δ	Medium difference [1]
ε_0	Free space permittivity [As/Vm]
ε	Permittivity [As/Vm]
ε_{r}	Relative permittivity [1]
$\varepsilon_{\mathrm{s},n}$	Gabriel parameter, permittivity for $\omega\tau >> 1$ [As/Vm]
$\varepsilon_{\infty,n}$	Gabriel parameter, permittivity for $\omega\tau << 1$ [As/Vm]
$\Delta\varepsilon_n$	Gabriel parameter, intensity of the dispersion region [As/Vm]
η_0	Intrinsic impedance of free space [V/A]
η_{i}	Intrinsic impedance [V/A]
κ_{ε}	Permittivity factor in free space [A/V]
$\kappa_{\mathrm{t}\varepsilon}$	Permittivity factor within the cylinder [A/V]
κ_{μ}	Permeability factor in free space [V/A]
$\kappa_{\mathrm{t}\mu}$	Permeability factor within the cylinder [V/A]
λ	Wavelength [m]

λ_0	Free space wavelength [m]
λ_S	Sommerfeld integration term [1/m]
μ_0	Free space permeability [Vs/Am]
μ_r	Relative permeability [1]
μ	Permeability [Vs/Am]
ψ_0	Angle direct path [rad]
ψ_1	Angle ground reflected path [rad]
ψ_2	Angle image plane reflected path [rad]
σ	Total electric conductivity [S/m]
σ_i	Ionic conductivity [S/m]
σ_a	Alternating conductivity [S/m]
σ_s	Static conductivity [S/m]
σ_1	Electric conductivity of the ground, resp. human body[S/m]
τ_n	Gabriel parameter, relaxation time constant [s]
ω	Angular frequency [1/s]
Π	Hertzian vector potential [Vm]
Π_0	Hertzian vector potential within free space region [Vm]
Π_1	Hertzian vector potential within ground, resp. human body [Vm]

List of Mathematic Operations and Functions

$\mathbf{r}\cdot\mathbf{r}$	Scalar multiplication between two vectors
$\mathbf{r}\times\mathbf{r}$	Cross product of two vertexes in 3D space
$\lvert\mathbf{r}\rvert$	Norm of a vector
$\mathbf{A}\cdot\mathbf{r}$	Matrix multiplication with a vector
∇A	Gradient of a scalar function A
∇_{S}	Transverse Nabla-operator
$\nabla\cdot\mathbf{A}$	Divergence of a vector function **A**
$\nabla\times\mathbf{A}$	Curl of a vector function **A**
$\mathbf{A}^{\mathrm{T}}$	Transpose of a vector or matrix
x, y, z	Cartesian coordinates
ρ, ϕ, z	Cylindrical coordinates
r, Θ, φ	Spherical coordinates
$\mathbf{e}_x, \mathbf{e}_y, \mathbf{e}_z$	Cartesian unit vectors

List of Abbreviations

BAN	Body-Area Network
FDTD	Finite-Difference Time-Domain
HED	Horizontal Electrical Dipole
IEEE	Institute of Electrical and Electronics Engineers
IFA	Inverted F-Antenna
ISM	Industrial, Scientific, and Medical
ITIS	Information Technologies in Society
LOS	Line-of-Sight
MICS	Medical Implant Communication Service
NLOS	Non-Line-of-Sight
PEC	Perfectly Electric Conductor
PIFA	Planar Inverted F-Antenna
PML	Perfectly Matched Layer
RMS	Root-Mean-Square
RX	Receiving Antenna
TX	Transmitting Antenna
UWB	Ultra-Wide-Band
VED	Vertical Electric Dipole
WBAN	Wireless Body-Area-Network
WLAN	Wireless Local Area Network

Chapter 1

Introduction

1.1 Background

The intercommunication of body-worn applications by use of wireless communication technologies is increasing rapidly nowadays. Related to [Hal06] and [Hal10], these applications range from security technologies, multimedia products and telemetric sports applications to healthcare systems. In addition, the ongoing miniaturization of wearable computer systems, such as smartphones, enables a multidisciplinary combination of these fields of application. A good indicator of the underlying heterogeneity is the large variation in covered frequency bands. Depending on the specific wireless system, the frequency of interest may range from the MICS band (Medical Implant Communication Service) at 400 MHz, over several ISM bands (Industrial Medical Scientific) in the lower GHz range, up to 60 GHz [Cha13] and 94 GHz [Pel12]. One common aspect of body-worn applications is the need for low-profile antennas, which is a primary demand to realize integrated and user-convenient systems. As a consequence thereof, the antenna properties as well as the propagation channel are physically connected to the body of the user. This fact prohibits the usage of the traditional free-space antenna theory to describe the resulting propagation scenario, where, for instance, the path gain can be directly calculated by the Friis formula from the separated antenna and channel characteristics. Instead, in terms of on-body communications, the antenna and channel characteristics overlap with each other. This exacerbates the problem to find a representative theoretical description to model the behavior of each component and their contribution to the total communication link. Inevitably, this has so far led to insufficient insight into the development of body-centric applications. To circumvent this problem, a common approach entails the modeling of the entire on-body link, consisting of transmitting antenna, human body and receiving antenna, as a whole. Typically, this is realized by complex numerical simulations or measurement set-ups of the entire system [Abb12]. While this approach delivers a concrete solution of a specific setup, minor insight is obtained regarding the general radiation and propagation mechanisms. More general information on how different configurations of antennas and channel behave can be obtained by the systematic variation of various setup parameters using statistical analysis [Gal11]. Despite the fact that this method extends the results that are obtained to a wider application field, it is still limited to the specific setups under test. To compensate this, a metric-like radiation characteristic would be preferable, which would give an adequate measure to evaluate the radiated power flow along the body curvature. The first steps into this direction are realized in [Akh10] and [Ber14]. These approaches use electromagnetic near-field observations of different antenna configurations in the presence of the human body to estimate the wave species of the related on-body far field. The aim of this thesis is to sharpen this approach, i.e. to realize an antenna de-embedding with connected antenna parameters. With this, antenna and channel characteristics can be characterized independently by concentrated measures and can be combined to model the desired communication setup. Moreover, the measures can be consulted to evaluate a specific antenna configuration or to derive general design demands for the applications desired.

1.2 Objective of this Work

The primary objective of this thesis is to define on-body antenna parameters and physically motivated EM propagation models, which enable the derivation of scalable path gain models as well as optimized design strategies. The key point of the underlying approach is the separation of the on-body far field into its wave species, i.e. into a transversal magnetic and transversal electric field component, for line-of-sight (LOS) as well as for non-line-of-sight conditions (NLOS).

The main issues in this thesis are:

- Uniformed Norton surface wave theory
- Enhanced model to solve the EM field around cylindrical dielectric structures
- Basics to model body-centric wireless applications
- Definition of concentrated on-body antenna measures
- Parameter discussion of related EM propagation effects
- Uniform theory to model LOS as well as NLOS on-body links
- Verification by numerical examples and measurement setups

1.3 Content and Organization of the Thesis

Chapter 2 takes up the basics of the Sommerfeld problem, the enhancements in terms of Norton surface waves, and the adaption to quasi-static ranges. Hereby, a unified theory is intended to deliver an adequate recapitulation of the thematic complex and to model the on-body antenna field as well as the derivation of related measures.

While the Sommerfeld theory is based on a planar propagation model, Chapter 3 discusses the solution of the electromagnetic field of a small dipole sources near a dissipative dielectric cylinder to represent heavily bended body surfaces. The solution derived is developed in such a way that the results can be adapted to the planar model of Chapter 2.

In general, the presented antenna de-embedding approach can be realized by different methods. In our case, the selected solution is based on the FDTD method to calculate the electric current distribution on the corresponding antenna structure. Hence, Chapter 4 summarizes the basic concepts of this numerical method and illustrates modeling considerations through different examples. In addition, basic measures are listed that are essential to model electromagnetic propagation effects in terms the wireless body-centric communications.

The basic concept of the developed de-embedding technique is presented in Chapter 5. While the first part discusses a volume cell-based approach to model the on-body far field of arbitrarily shaped antennas, the second part suggests a separation of the radiated field into its TM and TE components. Based on this approach, two equivalent sources are defined to represent an on-body antenna by its connected antenna parameters. This theory is evaluated with reference to the example of different antenna concepts and the accuracy of our achieved path gain model is evaluated by the FDTD method as well as by an equivalent measurement setup in an anechoic chamber.

Up to this point, the defined on-body antenna theory is capable of only modeling line-of-sight links. To enhance the applicability in terms of propagation links into body shadowed regions, the so-called non-line-of-sight links, the planar model is modified in Chapter 6. In this case, the line-of-sight technique is used to model the antenna coupling, i.e. the antenna near field. In terms of farther distances, separated propagation channel measures are consulted, which are based on the TM and TE field solution of dielectric cylinders of Chapter 3. By this, NLOS links can be modeled by scalable propagation parameters.

Chapter 2

The Electromagnetic Field on a Dissipative Planar Dielectric Surface

The solution of the radiated electromagnetic field of an antenna located above a dissipative planar surface is of interest in terms of its wide range of applications. The first attempts to find an adequate method of description can be traced back to the origins of radio science itself. The basis to calculate the radiated field of terrestrial communication setups was laid by Arnold Sommerfeld at the beginning of the 20th century [Som09]. At this early stage, the primary intention was laid onto the general far field description of an antenna located directly on the earth. The results indicate a ground wave at far distances, which is guided by the air-ground interface and significantly surpasses the wave components that are directly propagating through the air. In the following years, the solution was verified and modified by several authors. Kenneth Norton especially reshaped this work to find a clear separation of the connected wave components. Moreover, his contribution enables an interpretation of the radiated field by the superposition of an electromagnetic space and ground-bound wave [Nor37]. While, up to this point, the related research focused on terrestrial communications, the following work was also motivated by layered media, as can be found in dielectric substrates. Major contributions to this theory were made by many authors, and the reformulations and approximations made by James R. Wait, in particular, generalized the underlying theory [Wai61]. These definitions were used by Peter Bannister to enhance the range of applicability of the derived theory to quasi-static ranges [Ban78]. The focus of recent research aspects can be found on plasmonics [Mic16], as well as on body-centric communications [Akh10]. In terms of body-centric communications, the theory is consulted to model the influence of the user with respect to the communication link, where the model seems to be a promising starting point to represent more complex scenarios step by step [Gri10]. As seen in Fig. 2-1, the general approach models the propagation path along the human body by an equivalent dielectric half-space.

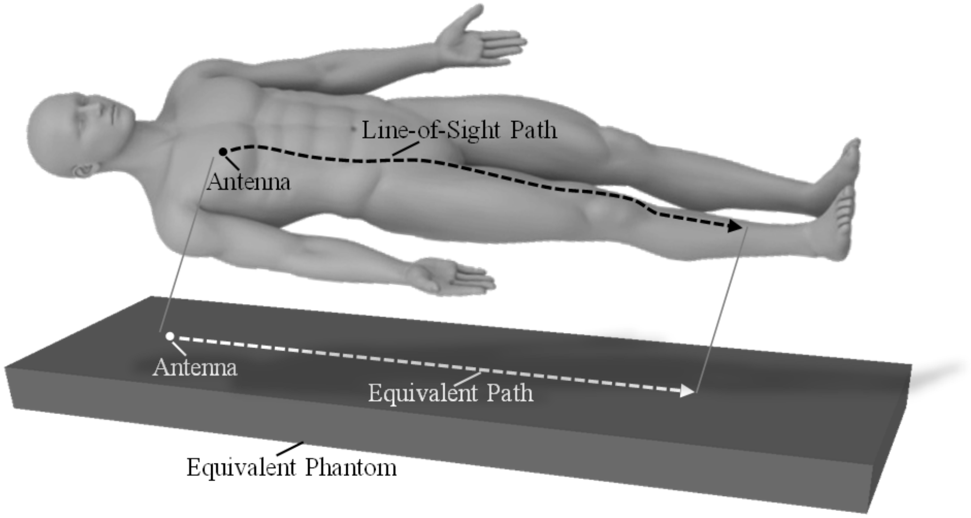

Fig. 2-1 General geometry of a planar dissipative dielectric phantom of infinite size to model the dominant propagation effects of line-of-sight paths along the human body in free space.

In terms of the Norton surface wave theory, the general contribution of this thesis is split into two parts. This chapter deals with the origin of the theory, briefly summarizes the theoretical background as well as defines a unified theoretical background. It starts with the original Sommerfeld problem, and then leads to the modifications made by Norton and Bannister. The benefits in terms of body-centric communications are discussed in Chapter 5 by the definition of derived antenna measures and the analysis of general propagation aspects by parameter variations. Finally, the evidence of the theory is evaluated for different numerical examples, where the practical relevance is underlined by measurements. In addition, the related mathematical field equations, i.e. the solution of the final Bannister approach, is listed in the appendix.

2.1 Helmholtz Equation and Vector Potential of an Electric Source

The electric current distribution of a radiating antenna structure can be linked to the related radiated antenna field. A probate method is to derive the electromagnetic field values by the source-related vector potentials. The potential functions may be given by the vector function **A**, which is commonly used nowadays. An equivalent approach, which was commonly used in the past, is the description by the Hertz potential **Π**. Both description methods are, in general, equivalent. As seen in [Bal05], knowing the electric current distribution **J** of the source **p**, assuming a negligible small magnetic current contribution, the vector potential **A** can be expressed by

$$\nabla^2\mathbf{A} - \gamma^2\mathbf{A} = -\mu\mathbf{J}\,. \tag{2.1}$$

Here, the magnetic field quantities are connected to the vector **A** with

$$\mathbf{H} = \frac{1}{\mu}\nabla\times\mathbf{A}\,, \tag{2.2}$$

and, using the Lorentz condition, to the electric field

$$\mathbf{E} = -j\omega\mathbf{A} - j\frac{1}{\omega\mu\varepsilon}\nabla(\nabla\cdot\mathbf{A})\,. \tag{2.3}$$

The propagation constant γ of the propagation medium is defined by the material parameters ε, μ, σ and the angular frequency ω through

$$\gamma^2 = j\omega\mu\sigma - \omega^2\mu\varepsilon\,. \tag{2.4}$$

In terms of body-centric communications, we assume now a magnetic transparent body, i.e. the permeability μ is equal to the free space permeability μ_0 throughout the following context. The permittivity, on the other hand, can either be real or complex. If the free space case is discussed, then the permittivity ε_0 of vacuum is assumed.

2.1.1 Connection to the Hertz Vector Potential

Corresponding to [Str41], the vector potential **A** is linked through its time derivative to the Hertz potential **Π** with

$$\mathbf{A} = \mu\varepsilon \frac{\partial \mathbf{\Pi}}{\partial t} . \tag{2.5}$$

Also, we can rearrange (2.5) and use the equivalent notation in the frequency domain to enable a direct calculation of the field quantities (2.2) and (2.3) from the Hertzian vector potential

$$\mathbf{A} = j\omega\mu\varepsilon\, \mathbf{\Pi} . \tag{2.6}$$

As a comparison of (2.5) and (2.6) reveals, a solution of (2.1) is indeed independent from the used vector potential formulation. In the following context, we follow the solution approach of A. Sommerfeld and his successors, who use a formulation based on the Hertz vector potential. Using (2.6), the magnetic field of (2.2) can be expressed in terms of the Hertzian vector potential by

$$\mathbf{H} = j\omega\varepsilon\, \nabla \times \mathbf{\Pi} . \tag{2.7}$$

An equivalent formulation can be found for the electric field. In this case, if we assume (2.4) for free space conditions, (2.3) can be expressed by

$$\mathbf{E} = -\gamma_0^2\, \mathbf{\Pi} + \nabla(\nabla \cdot \mathbf{\Pi}) . \tag{2.8}$$

2.2 Approach of Arnold Sommerfeld

The first discussion of a Hertzian dipole located above a planar dissipative ground was solved by A. Sommerfeld [Som09, Som26]. The general geometry is shown in Fig. 1, where the dipole is located at the coordinate origin, i.e. just above the dissipative medium.

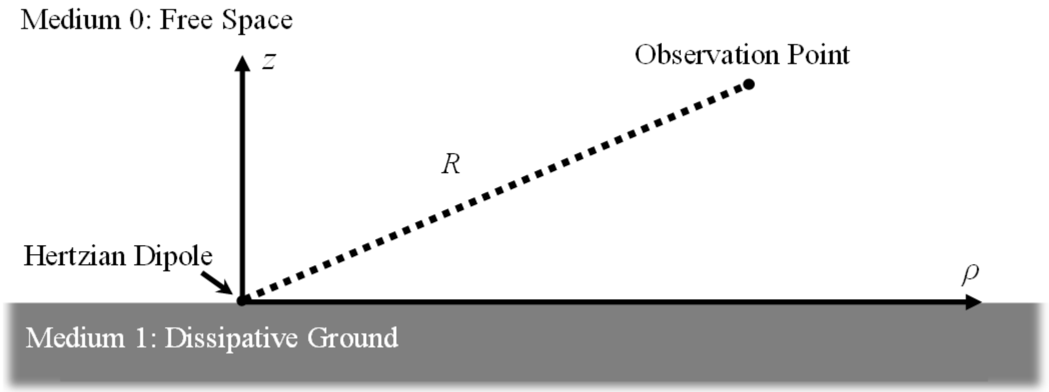

Fig. 2-2 Sommerfeld geometry [Som26]: Hertzian dipole on a dissipative medium.

The electromagnetic field of the defined geometry may be calculated by (2.7) and (2.8), solving the differential equation of the Hertzian vector potential **Π**:

$$\nabla^2 \mathbf{\Pi} - \gamma^2 \mathbf{\Pi} = 0, \tag{2.9}$$

where γ denotes the complex propagation constant of the corresponding medium. If the distance between the coordinate system origin and an arbitrary observation point is expressed in cylindrical coordinates by $R = (z^2+\rho^2)^{1/2}$, a solution of (2.9) is given by a z-orientated Hertzian dipole with momentum p with

$$\mathbf{\Pi} = \frac{p}{4\pi j\omega\varepsilon_0} \frac{e^{-\gamma R}}{R} \mathbf{e}_z. \tag{2.10}$$

In general, (2.10) can be found using the general potential function [Bal05], where the Hertzian vector potential is acquired by the use of (2.6). To find an appropriate solution of (2.9) in terms of the geometry, as shown in Fig. 2-2, (2.10) has to fulfill the following boundary conditions for the free space (γ_0) and the dissipative ground (γ_1) regions:

$$\begin{aligned} \nabla^2 \Pi_0 + \gamma_0^2 \Pi_0 &= 0 \quad \text{for } z > 0 \\ \nabla^2 \Pi_1 + \gamma_1^2 \Pi_1 &= 0 \quad \text{for } z < 0, \end{aligned} \tag{2.11}$$

$$\left.\begin{aligned}\Pi_0 &= \Pi_1\\ \frac{\mu_0}{\gamma_0^2}\frac{\partial \Pi_0}{\partial z} &= \frac{\mu_0}{\gamma_1^2}\frac{\partial \Pi_1}{\partial z}\end{aligned}\right\}\text{ for } z=0, \tag{2.12}$$

$$\begin{matrix}\Pi_0 = 0 & \text{for} & z>0, r\to+\infty, z\to+\infty\\ \Pi_1 = 0 & & z<0, r\to+\infty, z\to-\infty,\end{matrix} \tag{2.13}$$

$$\left.\begin{aligned}&\Pi_0 + \frac{e^{-\gamma_0 R_0}}{R_0}\\ &\Pi_1 + \frac{e^{-\gamma_1 R_1}}{R_1}\end{aligned}\right\}\begin{matrix}\text{has to be finite and continuous,}\\ \text{involving its first derivative.}\end{matrix} \tag{2.14}$$

A detailed discussion of the equations given above is presented in [Som26]. Here, equations (2.11) to (2.14) are given as an elementary reference to determine the electromagnetic field of a radiating source near a dissipative planar ground. Other, extended approaches follow the same procedure to formulate the related field equations. Even in the case of a stratified medium, the solution of (2.9) has to satisfy the boundary conditions related to the additional layers. A detailed solution is presented in [Wai98] and is discussed for a given on-body scenario in [Lea09]. The further analysis assumes a homogeneous ground in general.

2.2.1 General Solution by the Example of a Normally Orientated Hertzian Dipole

In the following, Sommerfeld's original work—considering a normally orientated Hertzian dipole, positioned directly on the surface—is briefly summarized to show the general procedure to calculate the related field quantities. As shown in [Som26], to solve (2.9), the total Hertz vector potential can be led back to the effect of two components: a primary excitation and a secondary one. The primary Hertz vector potential is related to the potential function of a Hertzian dipole in free space. While the vector potential within the ground is zero, in general, the potential function of a Hertzian dipole can be interpreted as an infinite sum of weighted Bessel functions within the corresponding media [Wey19]. In our case, this yields

$$\Pi_{0,\mathrm{prim}} = \frac{p}{4\pi j\omega\varepsilon_0}\frac{e^{-\gamma_0 R}}{R} = \frac{p}{4\pi j\omega\varepsilon_0}\int\limits_{\lambda_\mathrm{S}=0}^{\infty}\frac{\lambda_\mathrm{S}}{\sqrt{\lambda_\mathrm{S}^2+\gamma_0^2}}J(\lambda_\mathrm{S}\rho)\,e^{-\sqrt{\lambda_\mathrm{S}^2+\gamma_0^2}\,z}\,\mathrm{d}\lambda_\mathrm{S} \quad z>0, \tag{2.15}$$

$$\Pi_{1,\mathrm{prim}} = 0 \qquad z<0. \tag{2.16}$$

Generally speaking, the right side of (2.15) is called the Sommerfeld integral. Consistent with Fig. 2-2, γ_0 denotes the propagation constant of free space. The variable λ_S has been introduced by Sommerfeld as an integration constant and should not be misinterpreted with the electric wave length at this point. The secondary excitation component, as denoted in [Som26], can be defined along (2.15) by assuming the arbitrary functions f_0 and f_1. This results in:

$$\Pi_{0,\mathrm{sec}} = \frac{p}{4\pi j\omega\varepsilon_0}\int\limits_{\lambda_\mathrm{S}=0}^{\infty}\frac{\lambda_\mathrm{S}}{\sqrt{\lambda_\mathrm{S}^2+\gamma_0^2}}f_0(\lambda_\mathrm{S})J(\lambda_\mathrm{S}\rho)\,e^{-\sqrt{\lambda_\mathrm{S}^2+\gamma_0^2}\,z}\,\mathrm{d}\lambda_\mathrm{S} \qquad z>0, \tag{2.17}$$

$$\Pi_{1,\mathrm{sec}} = \frac{p}{4\pi j\omega\varepsilon_0}\int\limits_{\lambda_\mathrm{S}=0}^{\infty}\frac{\lambda_\mathrm{S}}{\sqrt{\lambda_\mathrm{S}^2+\gamma_1^2}}f_1(\lambda_\mathrm{S})J(\lambda_\mathrm{S}\rho)\,e^{-\sqrt{\lambda_\mathrm{S}^2+\gamma_1^2}\,z}\,\mathrm{d}\lambda_\mathrm{S} \qquad z<0. \tag{2.18}$$

The arbitrary functions f_0 and f_1 depend on the media parameters of medium 0, i.e. free space, and Medium 1, the dissipative ground. As stated by Sommerfeld, the primary, i.e. direct excitation component of the source, is now given in the form of (2.10), while the secondary excitation term, which is related to the influence of the ground, is expressed by (2.17) and (2.18). The total Hertzian vector potential results from the superposition of (2.15) and (2.17), resp. (2.16) and (2.18) and can be written by

$$\Pi_0 = \frac{p}{4\pi j\omega\varepsilon_0}\left[\frac{e^{-\gamma_0 R}}{R} + \int\limits_{\lambda_\mathrm{S}=0}^{\infty} f_0(\lambda_\mathrm{S})\,J(\lambda_\mathrm{S}\rho)\,e^{-\sqrt{\lambda_\mathrm{S}^2+\gamma_0^2}\,z}\,\lambda_\mathrm{S}\,\mathrm{d}\lambda_\mathrm{S}\right] \qquad z>0, \tag{2.19}$$

$$\Pi_1 = \frac{p}{4\pi j\omega\varepsilon_0}\left[\frac{e^{-\gamma_1 R}}{R} + \int\limits_{\lambda_\mathrm{S}=0}^{\infty} f_1(\lambda_\mathrm{S})\,J(\lambda_\mathrm{S}\rho)\,e^{-\sqrt{\lambda_\mathrm{S}^2+\gamma_1^2}\,z}\,\lambda_\mathrm{S}\,\mathrm{d}\lambda_\mathrm{S}\right] \qquad z<0. \tag{2.20}$$

The exact expression of f_0 and f_1 can be found by satisfying the boundary conditions (2.11) to (2.14) at $z = 0$. Finally, the resultant magnetic and electric field components can be found using (2.7), resp. (2.8). A more general solution, considering an antenna with significant effective antenna height above the ground, is discussed in the next paragraph. With this, the results have a wider range of applicability and some complex problems, which are related to the position of the source on the surface, are avoided. If the field quantities for an antenna at $h = 0$ are required, the corresponding field equations of the next paragraph (and the appendix) can be used.

2.3 Hertzian Vector Potential

Descending from the origins of this theory, where the major focus was on terrestrial communications, a vertical dipole orientation and a horizontal one were introduced within the original terminology. This terminology reaches down to the present days, and may be sufficient over a wide range of applications. But, if we compare Norton's and Bannister's formulations, even the terminology of the horizontal dipole differs—as the dipole of Bannister is rotated by 90° in comparison with Norton's definition. In addition, if we assume body-centric scenarios, the use of the terminology "vertical" may either refer to the ground or the body surface, and this ambiguity may yield misleading interpretations.

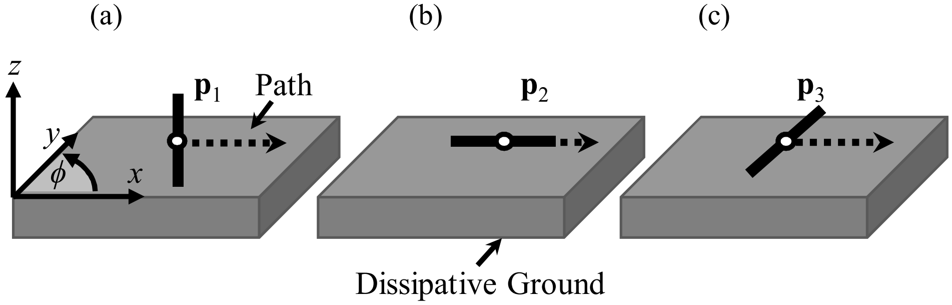

Fig. 2-3 Definition of three general dipole orientations in terms of body-centric propagations. in relation to the body surface and an observation path: (a) normal, (b) tangential longitudinal, (c) tangential transversal.

In the following, we define an observation path which proceeds at constant height parallel above the dissipative dielectric half-space. In general, we distinguish between a normal and tangential antenna orientation in relation to the ground (later body) surface. In addition, the tangential orientation is distinguished in relation to the applied observation path, a longitudinal (long) and transversal (trans) alignment; see Fig. 2-3.

2.3.1 Normally Orientated Small Electric Dipole

As seen in [Nor37], Kenneth Norton has solved (2.9) for Hertzian dipoles at a certain effective antenna height *h* above the dissipative ground. In comparison with the Sommerfeld geometry, shown in Fig. 2-2, the geometry of Norton, as seen in Fig. 2-4, includes not only the direct path R_0, but also consists of the reflected propagation path R_1. This approach enables an intuitive discussion of the far field behavior.

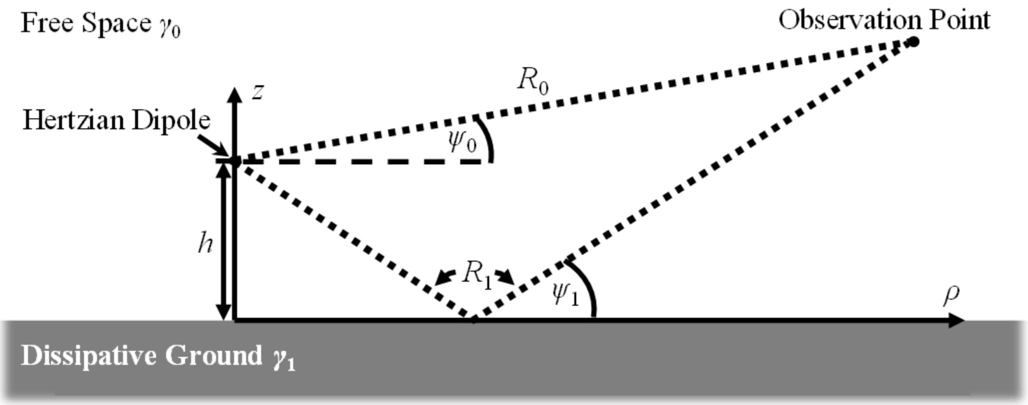

Fig. 2-4 Norton geometry [Nor41]: Hertzian dipole in free space above a dissipative medium at effective antenna height *h*.

The solution of (2.9) is based on the general method of Sommerfeld to satisfy (2.11)–(2.14), where the primary excitation considers the effect of the direct path R_0 as well as the reflected propagation path R_1. In this case, the Hertzian vector potential of a normally orientated dipole source consists only of a *z*-component and can be given by

$$\Pi_z\Big|_{\mathbf{p}_1} = \frac{p}{4\pi j\omega\varepsilon_0}\left[-\frac{e^{-\gamma_0 R_0}}{R_0}+\frac{e^{-\gamma_0 R_1}}{R_1}-\int_{\lambda_S=0}^{\infty}\frac{2}{u_0+\dfrac{\gamma_0}{\gamma_1}u_1}e^{-u_0(z+h)}J_0(\lambda_S\rho)\,\lambda_S\,\mathrm{d}\lambda_S\right], \quad (2.21)$$

where R_0, R_1, u_0, u_1, γ_0, and γ_1 are defined by

$$\begin{aligned} R_0^2 &= \rho^2 + (z-h)^2, \\ R_1^2 &= \rho^2 + (z+h)^2, \\ u_0^2 &= \lambda_{\mathrm{S}}{}^2 + \gamma_0^2, \\ u_1^2 &= \lambda_{\mathrm{S}}{}^2 + \gamma_1^2, \\ \gamma_0^2 &= -\omega^2 \mu_0 \varepsilon_0, \\ \gamma_1^2 &= \omega \mu_0 \sigma_1 - \omega^2 \mu_0 \varepsilon_1. \end{aligned} \tag{2.22}$$

Other than the original formulations of Norton, which employ a normalization factor to determine the radiated field in terms of the connected source, this formulation is linked to the dipole momentum $p = I\ell$ as defined in [Ban84b].

2.3.2 Tangentially Orientated Small Electric Dipole

The corresponding tangentially orientated vector potential solution of (2.9) possesses a component in x-direction as well as a component in z-direction [Nor37]. Following the steps along to (2.15)–(2.20) as seen in [Som26], the x-component of the vector potential is

$$\Pi_x\Big|_{\mathrm{P}_2} = \frac{p}{4\pi j\omega\varepsilon_0} \left[\frac{e^{-\gamma_0 R_0}}{R_0} - \frac{e^{-\gamma_0 R_1}}{R_1} + \int\limits_{\lambda_{\mathrm{S}}=0}^{\infty} \frac{2}{u_1 + u_0} e^{-u_0(z+h)} J_0(\lambda_{\mathrm{S}}\rho)\, \lambda_{\mathrm{S}}\, \mathrm{d}\lambda_{\mathrm{S}} \right], \tag{2.23}$$

where R_0, R_1, u_0, u_1, γ_0, and γ_1 are defined by (2.22). The z-component of the vector potential is

$$\Pi_z\Big|_{\mathrm{P}_2} = \frac{p}{4\pi j\omega\varepsilon_0} \cos\phi \int\limits_{\lambda_{\mathrm{S}}=0}^{\infty} \frac{2\,(u_1 - u_0)}{\gamma_1^2 u_0 + \gamma_0^2 u_1} e^{-u_0(z+h)} J_0{}'(\lambda_{\mathrm{S}}\rho)\, \lambda_{\mathrm{S}}{}^2\, \mathrm{d}\lambda_{\mathrm{S}}, \tag{2.24}$$

using again the definitions of R_0, R_1, u_0, u_1, γ_0, and γ_1 of (2.22). In addition, J_0’ denotes the recurrence function of the first kind Bessel function J_0.

2.4 Calculation of the Electromagnetic Field

Considering the lower ISM frequency bands, the length of the propagation path along the human body is in the range of the electromagnetic free space wave length. Considering the results of the previous formulations, which is restrict to distances of several free space wave lengths, the general use of these formulations is limited to smaller ranges. A suitable solution of this problem is given by Peter R. Bannister. The formulation derived is based on the extension of Norton's formulation for the quasi-static-range, i.e. below a free space wave length but larger than a penetration depth of the ground. The underlying theory assumes a finitely conducting ground of the depth $d/2$ where an additional layer of a perfect ground is inserted. Resulting from the added image plane, the solution includes an additional reflection path R_2 and reveals additional equation terms, which are capable of representing the underlying electromagnetic effects.

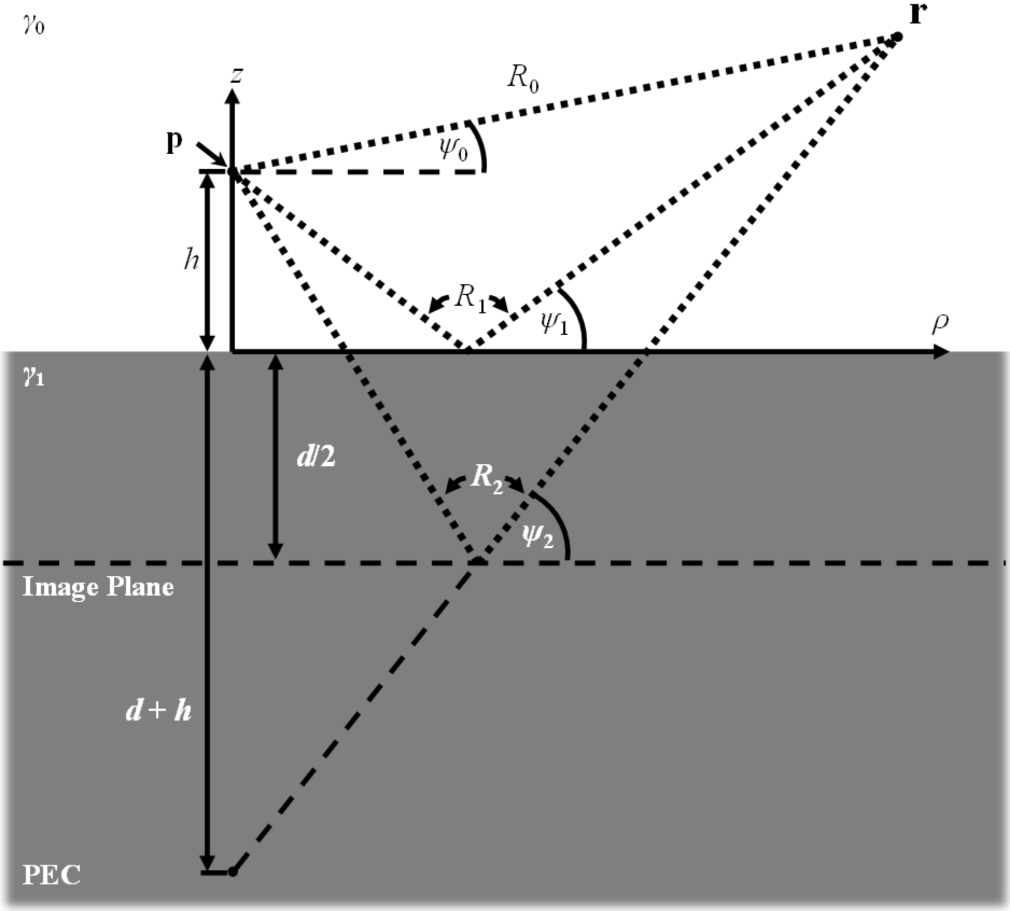

Fig. 2-5 Bannister geometry [Ban84b]: Hertzian dipole above a dissipative medium at effective antenna height h.

Considering the solution of the tangentially orientated small electric dipole $\mathbf{p}_2$ which points in propagation direction (x-direction), the total Hertzian vector potential can be expressed using (2.23) and (2.24) by

$$\mathbf{\Pi}\Big|_{\mathrm{P}_2} = \Pi_x\Big|_{\mathrm{P}_2} \mathbf{e}_x + \Pi_z\Big|_{\mathrm{P}_2} \mathbf{e}_z\,. \tag{2.25}$$

While the divergence of the vector potential (2.25) is given by

$$\nabla \cdot \mathbf{\Pi}\Big|_{\mathrm{P}_2} = \frac{1}{\rho}\frac{\partial}{\partial \rho}\left(\rho\ \Pi_x\Big|_{\mathrm{P}_2} \cos\phi\right) + \frac{\partial}{\partial z}\ \Pi_z\Big|_{\mathrm{P}_2}\,, \tag{2.26}$$

we can express the recurrence function of (2.24) by its ρ-derivative and apply the z-derivative of the second term of (2.26). Using (2.22), we can show that

$$\left(u_1 - u_0\right)\left(u_1 + u_0\right) = \gamma_1^2 - \gamma_0^2\,, \tag{2.27}$$

and, therefore, reformulate (2.26) into

$$\nabla \cdot \mathbf{\Pi}\Big|_{\mathrm{P}_2} = \frac{p\cos\phi}{4\pi j\omega\varepsilon_0}\frac{\partial}{\partial\rho}\left[\frac{e^{-\gamma_0 R_0}}{R_0} - \frac{e^{-\gamma_0 R_1}}{R_1} + 2\int\limits_{\lambda_\mathrm{S}=0}^{\infty} \frac{\gamma_0^2 e^{-u_0(z+h)}}{\gamma_1^2 u_0 + \gamma_0^2 u_1} J_0(\lambda_\mathrm{S}\rho)\,\lambda_\mathrm{S}\,\mathrm{d}\lambda_\mathrm{S}\right]. \tag{2.28}$$

Solving the modified Sommerfeld integral of (2.28) now, the related electric and magnetic field quantities can be found directly with the help of (2.7) and (2.8). In addition, if we consider a normally orientated small dipole and calculate the corresponding divergence by (2.26), the solution shows a remarkable similarity with (2.28). This enables the use of similar steps to solve the corresponding modified Sommerfeld integral to calculate the connected field quantities.

2.4.1 Approach for Quasi-Static to Far Field Ranges adapted from P. Bannister

The calculation of the electromagnetic field from the equations given above is, in general, feasible. However, the solution of the Sommerfeld integral and its ρ-derivation especially may not be evident by itself. Therefore, the following paragraph aims for a reformulation of (2.28) in terms of quasi-static ranges to far field ranges and follows the example of [Ban84b]. In contrast to the underlying derivations of P. Bannister, the discussed topic is rearranged into two sections. The first section lists common definitions and approximations with respect to the corresponding references and the second part deals with the reformulation of (2.28).

First, we consider the material difference Δ between the propagation constant of the dielectric ground γ_1 and free space γ_0, which is also related to the reflection index n [Bal89]. In general, we can define the material difference Δ by

$$\frac{\gamma_0^2}{\gamma_1^2} = \frac{1}{n^2} = \Delta^2 \tag{2.29}$$

and we can show in addition that

$$\Delta^2 \gamma_1 = \Delta \gamma_0 . \tag{2.30}$$

Furthermore, assuming a high difference between the media, i.e. $|n^2| >> 1$, we can set the definition of u_1 of (2.22) equal to γ_1. Under this assumption, (2.30) leads to

$$\Delta^2 u_1 \approx \Delta \gamma_0 . \tag{2.31}$$

Taking into account the media-related term of the integral of (2.28), we can show that

$$\frac{1}{u_0 + \Delta^2 u_1} \approx \frac{1}{u_0} - \frac{\Delta^2 u_1}{u_0 (u_0 + \Delta^2 u_1)} . \tag{2.32}$$

Using the approximation of (2.31), this leads to

$$\frac{1}{u_0 + \Delta^2 u_1} \approx \frac{1}{u_0} - \frac{\Delta \gamma_0}{u_0 (u_0 + \Delta^2 u_1)} . \tag{2.33}$$

As demonstrated in [Ban78], [Ban80], [Ban81], [Ban82] the condition $|n^2| >> 1$ leads to the approximation

$$\frac{u_1 - u_0}{u_1 + u_0} \approx e^{-u_0 d} , \tag{2.34}$$

and so also to

$$1 - \frac{u_1 - u_0}{u_1 + u_0} = \frac{2u_0}{u_1 + u_0} \approx 1 - e^{-u_0 d} , \tag{2.35}$$

where d can also be approximated by the dielectric properties of the ground with

$$d \approx \frac{2}{\gamma_1}. \tag{2.36}$$

Along with [Som26], considering Sommerfeld's integral

$$S_1 = \int_{\lambda_S=0}^{\infty} e^{-u_0(z+h)} J_0(\lambda_S \rho) \frac{\lambda_S}{u_0} \, \mathrm{d}\lambda_S = \frac{e^{-\gamma_0 R_1}}{R_1}, \tag{2.37}$$

and as shown in [Ban80], [Ban81], [Ban82], in addition to (2.35), the Hertzian vector potential in *x*-direction of (2.23) can be reduced to

$$\Pi_x\Big|_{\mathrm{P}_2} \approx \frac{p}{4\pi j\omega\varepsilon_0}\left[\frac{e^{-\gamma_0 R_0}}{R_0} - \frac{e^{-\gamma_0 R_2}}{R_2}\right], \tag{2.38}$$

where R_2 is defined by $R_2^2 = \rho^2 + (d+z+h)^2$. Taking (2.38) into account, the divergence of the Hertzian vector potential (2.28) can be reformulated as

$$\nabla \cdot \mathbf{\Pi}\Big|_{\mathrm{P}_2} \approx \frac{p\cos\phi}{4\pi j\omega\varepsilon_0} \frac{\partial}{\partial\rho}\left[\frac{e^{-\gamma_0 R_0}}{R_0} - \frac{e^{-\gamma_0 R_1}}{R_1} + I_{\mathrm{DIV}}\right] \tag{2.39}$$

where I_{DIV} is given by

$$I_{\mathrm{DIV}} = \int_{\lambda_S=0}^{\infty} \frac{2\,\Delta^2}{u_0 + \Delta^2 u_1} e^{-u_0(z+h)} J_0(\lambda_S \rho)\, \lambda_S \, \mathrm{d}\lambda_S \,. \tag{2.40}$$

If we now apply (2.32) and (2.37) to (2.40), I_{DIV} can be developed into

$$I_{\mathrm{DIV}} = 2\Delta^2\left[\frac{e^{-\gamma_0 R_1}}{R_1} - \int_{\lambda_S=0}^{\infty} \frac{\Delta^2 u_1}{u_0(u_0 + \Delta^2 u_1)} e^{-u_0(z+h)} J_0(\lambda_S \rho)\, \lambda_S \, \mathrm{d}\lambda_S\right]. \tag{2.41}$$

Using (2.31), (2.41) can be approximated by

$$I_{\mathrm{DIV}} \approx 2\Delta^2\left[\frac{e^{-\gamma_0 R_1}}{R_1} - \underbrace{\int_{\lambda_S=0}^{\infty} \frac{\Delta\gamma_0}{u_0(u_0 + \Delta\gamma_0)} e^{-u_0(z+h)} J_0(\lambda_S \rho)\, \lambda_S \, \mathrm{d}\lambda_S}_{=P}\right]. \tag{2.42}$$

As shown in [Ban84b], since $|\gamma_0\Delta| << 1$, the integral P has only a significant contribution when $|\gamma_0 R_1| >> 1$. Along with [Wai61] and [Wai96], when $|\gamma_0 R_1| >> 1$ and $|\gamma_0\Delta| << 1$ are satisfied, the integral P of (2.41) can be expressed by

$$P \approx \left(\frac{1-\Gamma_{||}}{2}\right)\left[1-F(w)\right]\frac{e^{-\gamma_0 R_1}}{R_1}, \tag{2.43}$$

where the Sommerfeld attenuation function is defined by

$$F(w) \approx \left[1-j\sqrt{\pi w}e^{-w}\mathrm{erfc}\left(-j\sqrt{w}\right)\right], \tag{2.44}$$

and the numerical distance w by

$$w \approx -\frac{\gamma_0 R_1}{2}\sin\left(\psi_1+\Delta\right)^2. \tag{2.45}$$

Owing to our assumption $|n^2| >> 1$, the Fresnel reflection coefficient $\Gamma_{||}$ for vertical polarizations can be reduced to

$$\Gamma_{||} \approx \frac{\sin\psi_1-\Delta}{\sin\psi_1+\Delta}, \tag{2.46}$$

where the angle ψ_1 is defined by

$$\tan\psi_1 = \frac{z+h}{\rho}. \tag{2.47}$$

Using (2.43) to (2.47), the integral (2.42) of (2.39) can be expressed by

$$I_{\mathrm{DIV}} \approx 2\Delta^2\frac{e^{-\gamma_0 R_1}}{R_1}\underbrace{\left[1-\left(\frac{1-\Gamma_{||}}{2}\right)\left[1-F(w)\right]\right]}_{=:A}. \tag{2.48}$$

Now, using the expression of (2.47), we can reformulate (2.39) as

$$\nabla\cdot\mathbf{\Pi}\Big|_{\mathrm{P}_2} \approx \frac{p\cos\phi}{4\pi j\omega\varepsilon_0}\frac{\partial}{\partial\rho}\left[\frac{e^{-\gamma_0 R_0}}{R_0}-\frac{e^{-\gamma_0 R_1}}{R_1}+2\Delta^2 A\frac{e^{-\gamma_0 R_1}}{R_1}\right]. \tag{2.49}$$

The factor A, as defined in (2.47), has been developed from (2.46), where the equality of

$$\frac{1-\Gamma_{\|}}{2}=\frac{\Delta}{\sin\psi_1+\Delta} \tag{2.50}$$

is used. Under consideration of (2.50), we can eliminate the Fresnel reflection coefficient $\Gamma_{\|}$ and express A as function of the angle ψ_1 by

$$A=\left(\frac{1+\Gamma_{\|}}{2}\right)+\left(\frac{1-\Gamma_{\|}}{2}\right)F(w)=\frac{\sin\psi_1+\Delta F(w)}{\sin\psi_1+\Delta}. \tag{2.51}$$

While the factor A is of major importance if the magnetic field values have to be calculated, Bannister defines a factor that comes in handy if the electric field is of interest. Following [Ban84b], the corresponding factor B is defined by

$$B=\sin\psi_1-\Delta A=\frac{\sin^2\psi_1-\Delta^2F(w)}{\sin\psi_1+\Delta}. \tag{2.52}$$

Bannister has illustrated that the factor A of (2.51) is different from unity only if two conditions are fulfilled. First of all, the angle ψ_1 has to be very small, and in the second place, the Sommerfeld attenuation function $F(w)$ has to be different from unity. Therefore, it is evident that A, resp. B, is a far field Norton surface-wave term only. In this case, all derivatives of A, resp. B, can be neglected which are not far field terms. Following this example, i.e. assuming far field conditions for $|n^2| >> 1$ and $|\Delta \sin\psi_1| << 1$, the derivative of the last term of (2.49) can be approximated as

$$\begin{aligned}\frac{\partial}{\partial\rho}\left(A\frac{e^{-\gamma_0R_1}}{R_1}\right)&=-A\left(1+\gamma_0R_1\right)\cos(\psi_1)\frac{e^{-\gamma_0R_1}}{R_1^2}+\frac{e^{-\gamma_0R_1}}{R_1}\frac{\partial A}{\partial\rho}\\&\approx-A\left(1+\gamma_0R_1\right)\cos(\psi_1)\frac{e^{-\gamma_0R_1}}{R_1^2}\\&\approx-\left(1+\gamma_0R_1A\right)\cos(\psi_1)\frac{e^{-\gamma_0R_1}}{R_1^2}.\end{aligned} \tag{2.53}$$

Combining the approximation of (2.53) with (2.49) we achieve

$$\begin{aligned}\nabla\cdot\mathbf{\Pi}\big|_{\mathrm{P}_2} \approx -\frac{p\cos\phi}{4\pi j\omega\varepsilon_0}\Bigg[&\left(1+\gamma_0 R_0\right)\cos(\psi_0)\frac{e^{-\gamma_0 R_0}}{R_0^2}+\\ &-\left(1+\gamma_0 R_1\right)\cos(\psi_1)\frac{e^{-\gamma_0 R_1}}{R_1^2}+\frac{2}{n^2}\cos(\psi_1)\frac{e^{-\gamma_0 R_1}}{R_1^2}\left(1+\gamma_0 R_1 A\right)\Bigg].\end{aligned} \tag{2.54}$$

Considering (2.32), (2.54) can be used to reformulate (2.24) to

$$\begin{aligned}\Pi_z\big|_{\mathrm{P}_2} = \frac{p\cos\phi}{4\pi j\omega\varepsilon_0}\frac{\partial}{\partial\rho}\Bigg[&\underbrace{2\int\limits_{\lambda_\mathrm{S}=0}^{\infty}\frac{e^{-u_0(z+h)}}{u_0(u_0+u_1)}J_0(\lambda_\mathrm{S}\rho)\,\lambda_\mathrm{S}\,\mathrm{d}\lambda_\mathrm{S}}_{=:I_{21}}+\\ &\underbrace{-2\Delta^2\int\limits_{\lambda_\mathrm{S}=0}^{\infty}\frac{e^{-u_0(z+h)}}{u_0(u_0+\Delta^2 u_1)}J_0(\lambda_\mathrm{S}\rho)\,\lambda_\mathrm{S}\,\mathrm{d}\lambda_\mathrm{S}}_{=:I_{22}}\Bigg],\end{aligned} \tag{2.55}$$

where I_{21} has a major contribution for small numerical distances w and I_{22} has an impact for large numerical distances. We can also write

$$\Pi_z\big|_{\mathrm{P}_2} = \frac{p\cos\phi}{4\pi j\omega\varepsilon_0}\frac{\partial}{\partial\rho}\left[I_{21}-I_{22}\right], \tag{2.56}$$

where I_{21} is defined by

$$I_{21} = 2\int\limits_{\lambda_\mathrm{S}=0}^{\infty}\frac{e^{-u_0(z+h)}}{u_0(u_0+u_1)}J_0(\lambda_\mathrm{S}\rho)\,\lambda_\mathrm{S}\,\mathrm{d}\lambda_\mathrm{S} \tag{2.57}$$

and I_{22} by

$$I_{22} = 2\Delta^2\int\limits_{\lambda_\mathrm{S}=0}^{\infty}\frac{e^{-u_0(z+h)}}{u_0(u_0+\Delta^2 u_1)}J_0(\lambda_\mathrm{S}\rho)\,\lambda_\mathrm{S}\,\mathrm{d}\lambda_\mathrm{S}\,. \tag{2.58}$$

The ρ-derivate of (2.57) is then given by

$$\frac{\partial I_{21}}{\partial \rho} = -\int\limits_{\lambda_S=0}^{\infty} \left(\frac{2u_0}{u_0+u_1} \right) e^{-u_0(z+h)} J_1(\lambda_S \rho) \frac{\lambda_S^2}{u_0^2} \, \mathrm{d}\lambda_S \, . \tag{2.59}$$

If now (2.35) is used, (2.59) can be reformulated to

$$\frac{\partial I_{21}}{\partial \rho} \approx -\int\limits_{\lambda_S=0}^{\infty} \left(1 - e^{-u_0 d} \right) e^{-u_0(z+h)} J_1(\lambda_S \rho) \frac{\lambda_S^2}{u_0^2} \, \mathrm{d}\lambda_S \, , \tag{2.60}$$

where [Ban81] and [Ban82] can be used to solve the integral of (2.60). The result is then given by

$$\frac{\partial I_{21}}{\partial \rho} \approx -\frac{1}{\rho} \left[\sin(\psi_2) e^{-\gamma_0 R_2} - \left(\sin(\psi_1) - \gamma_0 d \right) e^{-\gamma_0 R_1} \right]. \tag{2.61}$$

Here, the corresponding angles ψ1 and ψ2 are defined by

$$\begin{aligned} \sin(\psi_1) &= \frac{z+h}{R_1} \\ \cos(\psi_1) &= \frac{\rho}{R_1} \\ \sin(\psi_2) &= \frac{d+z+h}{R_2} \\ \cos(\psi_2) &= \frac{\rho}{R_2} . \end{aligned} \tag{2.62}$$

Along with [Ban84b], we can now reformulate (2.61) into

$$\frac{\partial I_{21}}{\partial \rho} \approx \frac{\cos(\psi_2) e^{-\gamma_0 R_2}}{R_2 + d + z + h} - \frac{(1+\gamma_0 d) \cos(\psi_1) e^{-\gamma_0 R_1}}{R_1 + z + h} \, . \tag{2.63}$$

As seen from the definitions of (2.62), the benefit of this notation is the clear separation of the (2.61) into the path R_2 and R_1, representing the quasi-static range term and a far field range term.

To solve the ρ-derivative of (2.58), we can first use the solution of (2.41) and the approximation of (2.36) to express (2.58) by

$$\begin{aligned} I_{22} &= 2\Delta^2 \int\limits_{\lambda_S=0}^{\infty} \frac{e^{-u_0(z+h)}}{u_0(u_0+\Delta)} J_0(\lambda_S\rho)\,\lambda_S\;\mathrm{d}\lambda_S \\ &= \frac{2\Delta^2 P}{\gamma_0\Delta} = \frac{2P}{\gamma_1} = Pd, \end{aligned} \tag{2.64}$$

where d denotes the depth of the image plane as defined in Fig. 2-5. Considering (2.64), the related ρ-derivative is

$$-\frac{\partial I_{22}}{\partial\rho} \approx \gamma_0 dP\cos(\psi_1) = \gamma_0 d\cos(\psi_1)\left(\frac{1-\Gamma_{\|}}{2}\right)\left[1-F(w)\right]\frac{e^{-\gamma_0 R_1}}{R_1}. \tag{2.65}$$

Considering (2.51), (2.55), (2.61), and (2.65), the z-component of the Hertzian vector potential can be reformulated as

$$\begin{aligned} \Pi_z\Big|_{\mathbf{p}_2} = -\frac{p\cos\phi}{4\pi j\omega\varepsilon_0\rho}\Big[&\sin(\psi_2)\,e^{-\gamma_0 R_2} - \sin(\psi_1)\,e^{-\gamma_0 R_1} + \\ &+\gamma_0\;d\;e^{-\gamma_0 R_1}\left(\sin^2(\psi_1) + A\cos^2(\psi_1)\right)\Big] \end{aligned}. \tag{2.66}$$

Considering our solutions (2.38), (2.54) and (2.65), we can now calculate the electromagnetic field quantities, applying (2.7) and (2.8). Using the same procedure and approximations, a solution of all electric dipole orientations is feasible. As shown by [Ban84b], even magnetic dipoles can be solved. However, owing to the fact that the solution of electric dipoles is sufficient for the desired scope of this thesis, the related equations are listed only in the appendix, while the solutions of the magnetic dipoles are unattended at this point.

2.4.2 Electromagnetic Field Quantities and Minor Reformulations

The general solution of the Hertzian vector potential depends—in general—on the orientation of the Hertzian dipole in terms of the ground and the suggested coordinate system. At this point, we follow the proposed theory of P. Bannister, the solution of which is based on the normally orientated dipole $\mathbf{p}_1$ and the tangential dipole $\mathbf{p}_2$; see Fig 2-3. As demonstrated in the previous paragraph, considering (2.7) and (2.8), the general solution procedures of (2.21), (2.23), and (2.24) lead to field quantities of [Ban84a] and

[Ban84b]. In contrast with the references, we perform two minor reformulations of the listed field equations of Bannister. Focusing on the outer factor, i.e. suppressing the factor within the square brackets, we can express (2.66) by

$$\Pi_z\Big|_{\mathrm{P}_2} = -\frac{p\cos\phi}{4\pi j\omega\varepsilon_0\rho}[\ldots]. \tag{2.67}$$

As the following example illustrates, (2.67) can be denoted as a function of the propagation constant γ_0 and the intrinsic impedance of free space η_0 by

$$\begin{aligned}\Pi_z\Big|_{\mathrm{P}_2} &= -\frac{p}{4\pi j\omega\rho}\sqrt{\frac{\mu_0}{\varepsilon_0^2\mu_0}}\cos\phi[\ldots]\\ &= -\frac{p}{4\pi\rho}\underbrace{\sqrt{\frac{\mu_0}{\varepsilon_0}}}_{=\eta_0}\underbrace{\frac{1}{j\omega\sqrt{\varepsilon_0\mu_0}}}_{=\gamma_0^{-1}}\cos\phi[\ldots]\\ &= -\frac{p\eta_0}{4\pi\gamma_0}\frac{\cos\phi}{\rho}[\ldots].\end{aligned} \tag{2.68}$$

This reformulation is considered for all further solutions. In addition, the field equations are restructured in such a way that the attenuation of the field can be led back to a spatial and a ground-wave attenuation term. This enables a direct comparison with other propagation scenarios, e.g. the free space or in-body case. To achieve such an adaption, the definitions of (2.62) are used with

$$\begin{aligned}R_0 &= \frac{\rho}{\cos\psi_0}\\ R_1 &= \frac{\rho}{\cos\psi_1}\\ R_2 &= \frac{\rho}{\cos\psi_2}.\end{aligned} \tag{2.69}$$

Defining the unit-less electric and magnetic field attenuation terms N^{E}, resp. N^{H}, we can describe the electric field components, in general, by

$$E_\nu = \frac{p\eta_0\gamma_0}{4\pi\rho} N_\nu^{\mathrm{E}}, \tag{2.70}$$

where $\nu \in \{\rho, \phi, z\}$, and magnetic field components by

$$H_\nu = \frac{p\gamma_0}{4\pi\rho} N_\nu^{\mathrm{H}}. \tag{2.71}$$

In fact, both attenuation terms depend on the corresponding dipole orientation as well as on all connected quantities, like frequency, dielectric properties of the ground and effective dipole height. Corresponding to the three basic dipole orientations, as defined in Fig. 2-3, Table 2-1 shows the related field quantities defined by (2.70) and (2.71), where the attenuation factors are listed in Appendix C.

TABLE 2-1
ELECTRIC AND MAGNETIC FIELD COMPONENTS
OF THE THREE BASIC DIPOLE ORIENTATIONS

	p1	**p**2	**p**3
E_ρ	$N_{1,\rho}^{\mathrm{E}}$	$\cos(\phi) N_{2,\rho}^{\mathrm{E}}$	$\cos\left(\phi - \frac{\pi}{2}\right) N_{2,\rho}^{\mathrm{E}}$
E_ϕ	$N_{1,\phi}^{\mathrm{E}} = 0$	$\sin(\phi) N_{2,\phi}^{\mathrm{E}}$	$\sin\left(\phi - \frac{\pi}{2}\right) N_{2,\phi}^{\mathrm{E}}$
E_z	$N_{1,z}^{\mathrm{E}}$	$\cos(\phi) N_{2,z}^{\mathrm{E}}$	$\cos\left(\phi - \frac{\pi}{2}\right) N_{2,z}^{\mathrm{E}}$
H_ρ	$N_{1,\rho}^{\mathrm{H}} = 0$	$\sin(\phi) N_{2,\rho}^{\mathrm{H}}$	$\sin\left(\phi - \frac{\pi}{2}\right) N_{2,\rho}^{\mathrm{H}}$
H_ϕ	$N_{1,\phi}^{\mathrm{H}}$	$\cos(\phi) N_{2,\phi}^{\mathrm{H}}$	$\cos\left(\phi - \frac{\pi}{2}\right) N_{2,\phi}^{\mathrm{H}}$
H_z	$N_{1,z}^{\mathrm{H}} = 0$	$\sin(\phi) N_{2,z}^{\mathrm{H}}$	$\sin\left(\phi - \frac{\pi}{2}\right) N_{2,z}^{\mathrm{H}}$

2.5 Separation of Wave Components

The following paragraph discusses the benefits of Norton's contribution and corresponds to [Gri14b].

One key point of K. Norton's approach [Nor37] is that the radiated electromagnetic field of a Hertzian dipole on or above a dissipative planar ground can be decomposed into a space wave component and a so-called Norton surface wave component. While the space wave component consists of the direct and ground-reflected wave components, the Norton surface wave can lead back to effects of the media boundary. In the past, the nature of this wave component was discussed controversially [Wai89]. Therefore, the terminology of these wave components was set by IEEE standard 211-1997 [Iee98], using its effect, and not directly by the cause. In this standard, the Norton surface wave component is defined as the difference that occurs between the total radiated electromagnetic field and the geometric optical field.

The total field can, therefore, be written as a superposition of the electric field components of the direct wave E_{DW}, the ground reflected component E_{RW}, and the Norton surface wave component E_{SW}:

$$E_{\mathrm{total}} = \underbrace{E_{\mathrm{DW}} + E_{\mathrm{RW}}}_{\text{Space Wave}} + \underbrace{E_{\mathrm{SW}}}_{\text{Norton Surface Wave}} . \tag{2.72}$$

The sum of the first and second terms of (2.72) is often called space wave. For an antenna height of $h = 0$, the direct wave and the ground reflected wave cancel each other out and only a Norton surface wave is excited. As seen in the previous section, the corresponding components can be directly identified by the connected path variables of (2.69), where the indices 0, 1, and 2 of the path and angle factors indicate the direct, ground-reflected and quasi-static terms of our solution in Appendix C. The remaining term, in general a function of the Sommerfeld attenuation term $F(w)$, is then the Norton surface wave component. The general geometry in terms of this terminology is shown in Fig. 2-6.

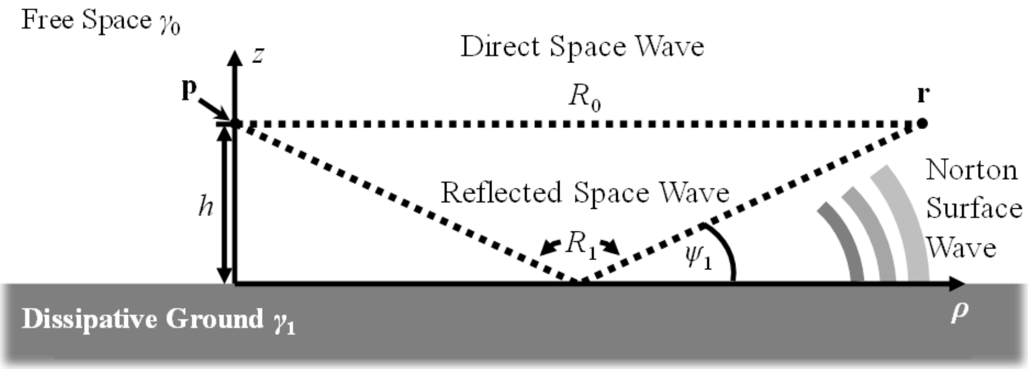

Fig. 2-6 Modified Norton Geometry [Nor41]: Ground wave separation into space and surface wave components for propagation paths parallel to the ground surface.

Based on (2.21)–(2.24), Norton has derived in [Nor41] an expression for the magnitude of the electric field $E_{1/3}$ generated by a dipole antenna, located at the effective antenna height h above the ground. As indicated by the indices, the related solution deals with a normal dipole orientation as well as with a tangential one: to be exactly $\mathbf{p}_1$, resp. $\mathbf{p}_3$. Considering the geometry of Fig. 2-6, i.e. the propagation path proceeds parallel along the surface, and his solution leads to

$$E_{1/3} = \frac{U_{1/3}}{\rho}\left[\underbrace{\cos^3(\psi_0)e^{-\gamma_0 R_0}}_{\text{DW: direct wave}} + \underbrace{\Gamma_{1/3}\cos^3(\psi_1)e^{-\gamma_0 R_1}}_{\text{RW: ground-reflected wave}} + \underbrace{(1-\Gamma_{1/3})F(w)\cos^2(\psi_1)e^{-\gamma_0 R_1}}_{\text{SW: Norton surface wave}}\right]. \tag{2.73}$$

As defined by Norton, in (2.73), the value $U_{1/3}$ is a normalization factor which represents primarily the dipole excitation, and can be, in principle, defined by our right-sided factor in (2.70) as well. The Fresnel plane-wave reflection coefficient of the boundary between the free space and the dissipative ground is defined by $\Gamma_{1/3}$ and related as well to the dipole orientations, while in (2.73), the Sommerfeld attenuation function is denoted by

$$F(w) \approx \left[1 - j\sqrt{\pi w}e^{-w}\mathrm{erfc}\left(-j\sqrt{w}\right)\right], \tag{2.74}$$

where the numerical distance w is

$$w \approx -\frac{\gamma_0 R_1}{2}\sin\left(\psi_1 + \frac{\gamma_0}{\gamma_1}\right)^2 . \tag{2.75}$$

Both definitions are equivalent to our definitions in (2.44) and (2.45). Considering (2.75), the numerical distance w can be understood as an effective distance, taking into account the antenna height, the frequency and the constitutive parameters on both sides of the boundary.

Notice that (2.73), (2.74) and (2.75) are not exactly conformal to the formulation discussed by Norton. In fact, these expressions correspond to the definitions of Wait and Bannister [Ban84b], [Ban79] which enable a consistent terminology in the scope of the whole theory presented above. In principle, the definition of (2.74) yields Norton's expression by a factor of minus one in front of the square root for a complex conjugate numerical distance. A closer look at how Norton derived (2.73) in [Nor41] reveals simplifications where he neglects electric field components of second and third order, which vanish for far distances. Therefore, his assumptions are partially equivalent to the approximations of Bannister, i.e. neglecting only the quasi-static derivations, and so are valid only for the far field region. From Norton's perspective, this is fair enough for terrestrial propagation over large distances. In the scope of on-body propagation, such far field limitations, e.g. referring to distances which are greater than a wavelength, would be quite restrictive, but can help in the identification of the major propagation effects. For a stratified medium, the solution of (2.21)–(2.24) has to consider additional propagation paths related to the reflections at the multilayer boundaries. A detailed approach is presented in [Wai98] and discussed for a given on-body scenario in [Lea09]. Our further analysis assumes a homogeneous ground.

Chapter 3

The Electromagnetic Field on a Dissipative Dielectric Cylinder

With the planar far field model of Chapter 2 in mind, the effect of the curvatures of small degree along the human body surface may result in a wider, irregularly distributed spread around the modeled average mean value [Nor41]. Therefore, the model is still applicable if the bending radius is significantly larger than a free space wave length. Otherwise, a suitable solution to model diffraction effects of bended non-line-of-sight propagation links may be given by the general diffraction theory (GDT) [Bal05]. But in case of body-centric propagations, the small distance between radiation source, i.e. the antenna structure, and the body, prohibits the adequate transfer of this theory and may be limiting.

In terms of non-line-of-sight propagations along bended body curvatures, an intuitive model is given by a dissipative dielectric cylinder to represent the human body curvature [For10], [Alv11]. To find a straightforward solution to this geometry, the following approach is restricted to paths which progress at a fixed height—in general, the effective antenna height h—above the cylinder surface. In addition, the assumed path is chosen in such a way that the coordinates are transverse to the cylinder axis. Owing to the origin of the underlying approach tangentially polarized sources can be modeled only. In this manner, both sources are distinguished by their alignment in relation to the propagation path, a parallel and a perpendicular orientation. Contrary to the solution of line-of-sight propagation scenarios, which are based on Hertzian potential equations, the following approach leads back to a scattering problem. As illustrated by [Bal89], the total electromagnetic field, denoted by $\mathbf{E}^{\text{total}}$ and $\mathbf{H}^{\text{total}}$, can be decomposed into an excitation-related incident field and a geometry-related scattered field. Therefore, the expression of the electric field yields

$$\mathbf{E}^{\text{total}} = \mathbf{E}^{\text{inc}} + \mathbf{E}^{\text{sct}}, \tag{3.1}$$

where the incident and scattered components are represented by $\mathbf{E}^{\text{inc}}$ and $\mathbf{E}^{\text{sct}}$. The magnetic field can be expressed by equivalent sub-indices by

$$\mathbf{H}^{\text{total}} = \mathbf{H}^{\text{inc}} + \mathbf{H}^{\text{sct}}. \tag{3.2}$$

According to the symmetric cylinder geometry, the incident component, as well as the scattered component, can be modeled by a superposition of Bessel functions of different kind and order. Owing to the nature of the underlying geometry, the initial solution is derived for line sources, as stated by [Che90]. General notation remarks and definitions are given in the following chapter. The extension to point sources is made analogous to [For10] by the use of the inverse Fourier transformation in k_z-domain, while the explicit solution of both tangentials to the cylinder surface aligned sources is derived at the end of the chapter.

3.1 General Definitions and Denotations

The underlying model assumes a dissipative dielectric cylinder of infinite length and radius a in free space. The cylinder axis is aligned in z-direction at the origin of the coordinate system. Therefore, the transverse solution path can be found within the xy-plane. The general geometry is shown in Fig. 3-1, where the solution is restricted to a parallel path proceeding with constant distance h around the cylinder surface.

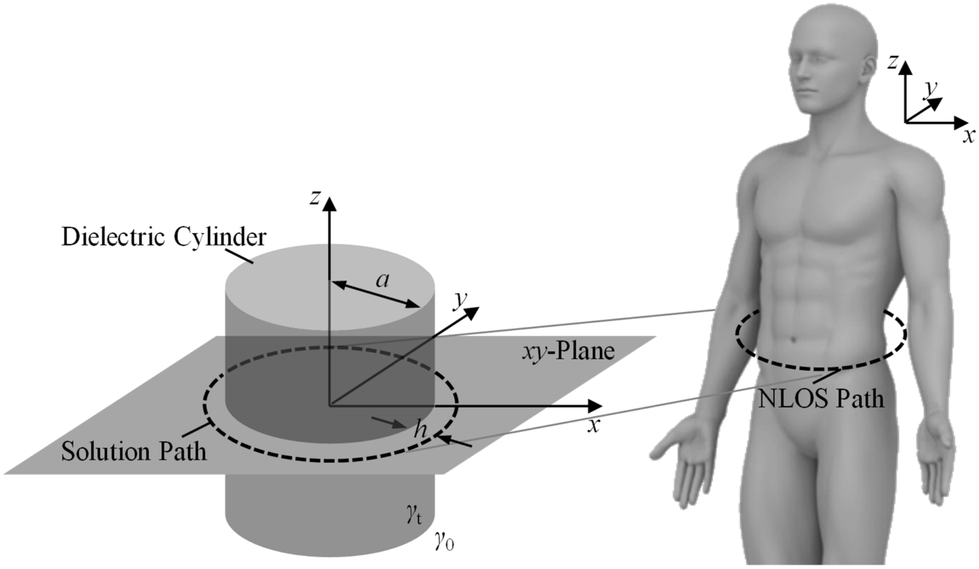
Dielectric Cylinder
z
a
y
xy-Plane
x
h
Solution Path
γ_t
γ_0
NLOS Path
z
y
x

Fig. 3-1 General geometry of a dielectric cylinder of infinite length aligned in *z*-direction in free space to model the dominant propagation effects of non-line-of-sight paths around the human body.

3.1.1 Electric Field of a Line Source in Free Space

At first, the incident field can be led back to an infinite electric line source in free space, which proceeds in *z*-direction, and is shifted by the special vector $\mathbf{r}'(\rho',\phi')$: see Fig. 3-2.

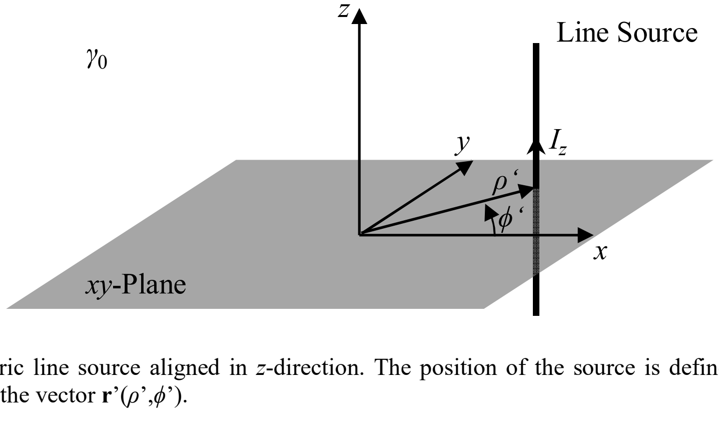
γ_0
z
Line Source
y
I_z
ρ'
ϕ'
x
xy-Plane

Fig. 3-2 Electric line source aligned in *z*-direction. The position of the source is defined within the *xy*-plane at $z = 0$ by the vector $\mathbf{r}'(\rho',\phi')$.

Due to the given symmetry, which is connected to the electric current distribution in *z*-direction, the electric field consists of only a *z*-component. Corresponding to [Bal89], the electric field can be given, using the addition theorem of Hankel functions with

$$E_z^{\text{line}} = \frac{\gamma_0^2 I_z}{4\pi\varepsilon_0} \begin{cases} \sum\limits_{m=-\infty}^{\infty} H_m^{(2)}(\gamma_0\rho')J_m(\gamma_0\rho)\,\mathrm{e}^{jm(\phi-\phi')} & \rho \le \rho' \\ \sum\limits_{m=-\infty}^{\infty} J_m(\gamma_0\rho')H_m^{(2)}(\gamma_0\rho)\,\mathrm{e}^{jm(\phi-\phi')} & \rho \ge \rho' \end{cases} \tag{3.3}$$

where γ_0 denotes the propagation constant of free space and I_z the magnitude of the electric current of the line source. As intended, we consider only on-body propagation paths, meaning the solution space can be found at $\rho = \rho'$ in general. Therefore, the following solution only considers the first term of (3.3), and thus, is restricted to $\rho \le \rho'$. The restricted electric field is then given by

$$E_z^{\text{line}} = \sum_{m=-\infty}^{\infty} C_m J_m(\gamma_0\rho)\,\mathrm{e}^{jm(\phi-\phi')} \tag{3.4}$$

while the factor C_m is related only to the position and excitation of the source. In case of a current I_z in z-direction, it is defined by

$$C_m = \frac{\gamma_0^2 I_z}{4\pi\varepsilon_0} H_m^{(2)}(\gamma_0\rho')\,. \tag{3.5}$$

If the outer space is of interest, i.e. $\rho \ge \rho'$, and the second term of (3.3) is focused, an equivalent expression can be found following the same solution concept.

3.1.2 Connection between Line and Point Sources

The form of (3.4) implies that a superposition of infinite harmonic Bessel function elements is sufficient to describe the related electric field of an infinite expanded line source. Contrariwise, it seems evident to follow the effect of a single point source from the solution of a corresponding line source. As demonstrated in detail in [For10], this can be realized by applying an inverse Fourier transformation in k_z-domain with

$$\mathbf{E}^{\text{point}} = \frac{1}{2\pi} \int_{k_z=-\infty}^{\infty} \mathbf{E}^{\text{line}}\,\mathrm{d}k_z\,. \tag{3.6}$$

Having lossless media in mind, in the following context, the propagation constant γ is expressed by the equivalent definition of the wave-number k, which are linked to each other by $\gamma = jk$. In addition, without the loss of generality, we assume different wave numbers in ρ- and z-directions, k_ρ resp. k_z, which are generally related by

$$k_\rho = \sqrt{k^2 - k_z^2}\,. \tag{3.7}$$

The corresponding reformulation of (3.4) yields

$$E_z^{\text{line}} = \sum_{m=-\infty}^{\infty} C_m J_m(k_\rho \rho)\,\mathrm{e}^{jm(\phi-\phi')}\mathrm{e}^{-jk_z z} \tag{3.8}$$

with

$$C_m = \frac{k_\rho^2 I_z}{4\pi\varepsilon_0} H_m^{(2)}(k_\rho \rho')\,. \tag{3.9}$$

Owing to the fact that a singularity occurs at $k_z = k$, the integration of (3.6) is problematic if an analytical approach is intended. Alternatively, a solution can be achieved by a numerical solution. Following [For10], a parabolic contour integral of the form

$$\operatorname{Im}\{k_z\} = C\left(1 - \left(\frac{\operatorname{Re}\{k_z\} - k_0}{k_0}\right)^2\right) \tag{3.10}$$

is used in the complex k_z plain to circumvent the singularity of (3.6) with distance C—see Fig. 3-3.

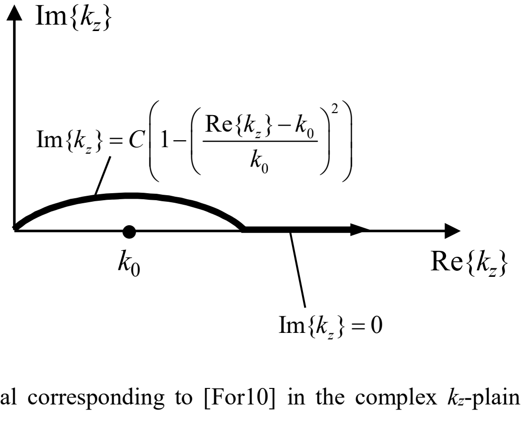
$\operatorname{Im}\{k_z\}$
$\operatorname{Im}\{k_z\} = C\left(1 - \left(\frac{\operatorname{Re}\{k_z\} - k_0}{k_0}\right)^2\right)$
k_0
$\operatorname{Re}\{k_z\}$
$\operatorname{Im}\{k_z\} = 0$

Fig. 3-3 Contour integral corresponding to [For10] in the complex k_z-plain to avoid the singularity at $k_z = k_0$.

In the following context, the applied theory is, in general, related to line sources. However, having the connection to point sources via (3.6) in mind, and because of the significance of point sources in the scope of the evaluated antenna properties, we shall primarily address these sources in the following context.

3.2 Transversal Components of the Electromagnetic Field

Till now, only the electric field component has been considered. The electromagnetic field components that are transversal to the *z*-direction can be found within the *xy*-plane. Generally, the transverse electric field $\mathbf{E}_\mathrm{s}$ is then given by

$$\mathbf{E}_\mathrm{s} = E_\rho \mathbf{e}_\rho + E_\phi \mathbf{e}_\phi , \tag{3.11}$$

and the transverse magnetic field $\mathbf{H}_\mathrm{s}$ by

$$\mathbf{H}_\mathrm{s} = H_\rho \mathbf{e}_\rho + H_\phi \mathbf{e}_\phi . \tag{3.12}$$

Along with [Che90], the transverse electromagnetic field values are linked to the *z*-components by

$$\mathbf{E}_\mathrm{s} = \frac{1}{k_\rho^2}\left[-jk_z \nabla_\mathrm{s} E_z + j\omega\mu \mathbf{e}_z \times \nabla_\mathrm{s} H_z\right], \tag{3.13}$$

$$\mathbf{H}_\mathrm{s} = \frac{1}{k_\rho^2}\left[-jk_z \nabla_\mathrm{s} H_z - j\omega\varepsilon \mathbf{e}_z \times \nabla_\mathrm{s} E_z\right]. \tag{3.14}$$

By letting $\nabla = \nabla_\mathrm{s} + \mathbf{e}_z \frac{\partial}{\partial z}$ the operator ∇_s represents the transverse Nabla-operator with

$$\nabla_\mathrm{s} = \mathbf{e}_\rho \frac{\partial}{\partial \rho} + \mathbf{e}_\phi \frac{1}{\rho}\frac{\partial}{\partial \phi} . \tag{3.15}$$

As seen later, we can generally assume a Bessel or Hankel function as the driving element behind the field components of our geometry. Keeping this fact in mind, we can solve (3.13) and (3.14) using the corresponding derivative. In this case, the transverse electric field components are

$$E_\rho = \frac{1}{k_\rho^2}\left[-jk_z \frac{\partial E_z}{\partial \rho} + \frac{\omega\mu m}{\rho} H_z\right], \tag{3.16}$$

$$E_\phi = \frac{1}{k_\rho^2}\left[\frac{k_z m}{\rho}E_z + j\omega\mu\frac{\partial H_z}{\partial \rho}\right]. \tag{3.17}$$

Analogously, we can reformulate the transverse magnetic field components

$$H_\rho = \frac{1}{k_\rho^2}\left[-jk_z\frac{\partial H_z}{\partial \rho} - \frac{\omega\varepsilon m}{\rho}E_z\right], \tag{3.18}$$

$$H_\phi = \frac{1}{k_\rho^2}\left[\frac{k_z m}{\rho}H_z - j\omega\varepsilon\frac{\partial E_z}{\partial \rho}\right]. \tag{3.19}$$

3.3 Tangential Transversal Orientated Source

To evaluate the electromagnetic field distribution of a point source polarized in the *z*-direction, we consider the infinite electric line source of the previous paragraph with current flow **I**$_z$ near an infinite, *z*-directed dielectric cylinder. In terms of the underlying geometry, the source is polarized parallel to the cylinder surface and perpendicular to the on-body path and the position is defined by the spatial vector **r**'(ρ',ϕ'). The general setup is depicted in Fig.3-4.

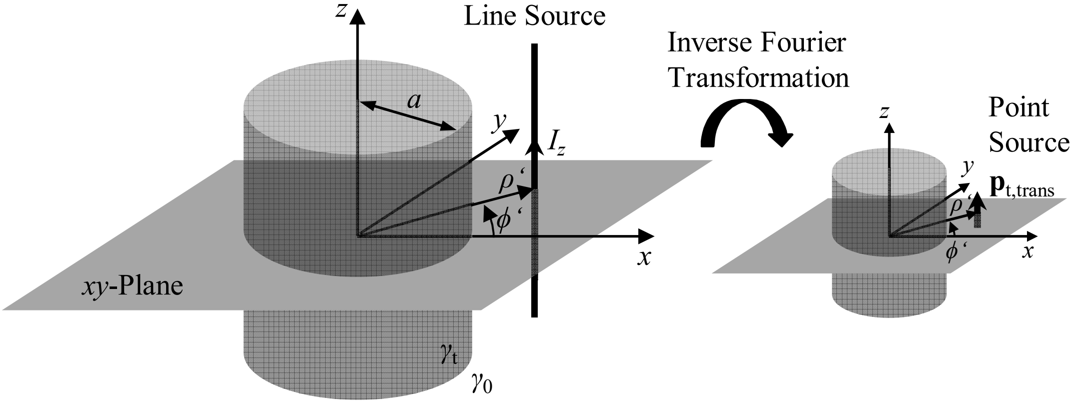

Fig. 3-4 An infinite electric line source aligned in *z*-direction is positioned parallel to a dissipative dielectric cylinder of infinite length.

The cylinder is assumed to consist of a homogenous dissipative dielectric with propagation constant γ_t, and the outer space is considered to have perfect free space properties.

3.3.1 Incident Field Components

As shown by [For10], the incident electric field of this geometry can be led back to (3.4), which describes the electric field of the line source in free space, i.e. the presence of the dielectric cylinder is neglected. Owing to the underlying geometry, the electric field consists only of a *z*-component. In terms of on-body propagations, we have limited the solution space to radii greater than the cylinder radius *a* and smaller than the position distance of the source *ρ*'. The electric field can be expressed by

$$E_z^{\text{inc}}\Big|_{\mathbf{I}_z} = \sum_{m=-\infty}^{\infty} C_m J_m(k_\rho \rho)\, \mathrm{e}^{jm(\phi-\phi')} \mathrm{e}^{-jk_z z} \qquad a \le \rho \le \rho', \tag{3.20}$$

where C_m is defined by (3.5). Because of the transverse nature of the field components, the magnetic field can be acquired by using (3.18) and (3.19). Since H_z is zero, the equations can be reduced to

$$H_\rho = -\frac{\omega \varepsilon m}{k_\rho^2 \rho} E_z \tag{3.21}$$

$$H_\phi = -\frac{j\omega\varepsilon}{k_\rho^2} \frac{\partial E_z}{\partial \rho}. \tag{3.22}$$

Therefore, the related magnetic field components of this geometry are

$$H_\rho^{\text{inc}}\Big|_{\mathbf{I}_z} = -\frac{\omega \varepsilon_0}{k_\rho^2 \rho} \sum_{m=-\infty}^{\infty} m C_m J_m(k_\rho \rho)\, \mathrm{e}^{jm(\phi-\phi')} \mathrm{e}^{-jk_z z} \qquad a \le \rho \le \rho' \tag{3.23}$$

$$H_\phi^{\text{inc}}\Big|_{\mathbf{I}_z} = -\frac{j\omega \varepsilon_0}{k_\rho \rho} \sum_{m=-\infty}^{\infty} C_m J'_m(k_\rho \rho)\, \mathrm{e}^{jm(\phi-\phi')} \mathrm{e}^{-jk_z z} \qquad a \le \rho \le \rho'\ . \tag{3.24}$$

3.3.2 Scattered Field Components

As shown in [For10], the scattered electromagnetic field components on the cylinder, i.e. $\rho \le a$, can be obtained from the Helmholtz equations using the separation of variables. Assuming our z-directed electric line source, the electric field consists only of a *z*-component

$$E_z^{\mathrm{sct}}\Big|_{\mathbf{I}_z} = \sum_{m=-\infty}^{\infty} A'_m H_m^{(2)}(k_\rho \rho)\,\mathrm{e}^{jm(\phi-\phi')}\mathrm{e}^{-jk_z z} \qquad \rho \geq a\,. \tag{3.25}$$

The coefficient A'_m depends on the excitation and position of the source, as well as on the properties and size of the cylinder. And an explicit solution is given in Subchapter 3.3.4. Using (3.21) and (3.22), the transverse components of the scattered magnetic field can be given with

$$H_\rho^{\mathrm{sct}}\Big|_{\mathbf{I}_z} = -\frac{\omega\varepsilon}{k_\rho^2 \rho} \sum_{m=-\infty}^{\infty} m A'_m H_m^{(2)}(k_\rho \rho)\,\mathrm{e}^{jm(\phi-\phi')}\mathrm{e}^{-jk_z z} \qquad \rho \geq a \tag{3.26}$$

$$H_\phi^{\mathrm{sct}}\Big|_{\mathbf{I}_z} = -\frac{j\omega\varepsilon}{k_\rho} \sum_{m=-\infty}^{\infty} A'_m H'^{(2)}_m(k_\rho \rho)\,\mathrm{e}^{jm(\phi-\phi')}\mathrm{e}^{-jk_z z} \qquad \rho \geq a\,. \tag{3.27}$$

3.3.3 Total Field Components

As internally stated by (3.1) and (3.2), the total electromagnetic field results from the superposition of the incident and scattered fields. If we combine the results of (3.20) and (3.25), the total electric field of the *z*-directed source is

$$\mathbf{E}^{\mathrm{total}}\Big|_{\mathbf{I}_z} = \left.\begin{bmatrix} 0 \\ 0 \\ \mathbf{E}_z^{\mathrm{inc}} + \mathbf{E}_z^{\mathrm{sct}} \end{bmatrix}\right|_{\mathbf{I}_z} \qquad \rho \geq a\,. \tag{3.28}$$

In the same way, the corresponding magnetic field values result from the superposition of (3.23)–(3.24), and (3.26)–(3.27)

$$\mathbf{H}^{\mathrm{total}}\Big|_{\mathbf{I}_z} = \left.\begin{bmatrix} \mathbf{H}_\rho^{\mathrm{inc}} + \mathbf{H}_\rho^{\mathrm{sct}} \\ \mathbf{H}_\phi^{\mathrm{inc}} + \mathbf{H}_\phi^{\mathrm{sct}} \\ 0 \end{bmatrix}\right|_{\mathbf{I}_z} \qquad \rho \geq a\,. \tag{3.29}$$

As seen, the total field shows a TE-characteristic within our suggested solution space in the *xy*-plane. This can be stated for the z-orientated line source as well as for the related point source.

3.3.4 Coefficient Calculation by Applied Boundary Conditions

To calculate the electromagnetic field values outside the cylinder, the coefficient *A*’ is required to determine the scattered field contribution. Along with [For10], the coefficients are calculated by the boundary conditions which are related to the continuous field values of the tangential components. In addition, the *z*-components of the total field within the cylinder can be assumed as a superposition of Bessel function elements. In case of the line source $\mathbf{I}_\mathrm{z}$, this results in:

$$E_z^{\mathrm{total}}\Big|_{\mathbf{I}_z} = \sum_{m=-\infty}^{\infty} A_m J_m(k_{\mathrm{t}\rho}\rho)\,\mathrm{e}^{jm(\phi-\phi')}\mathrm{e}^{-jk_z z} \qquad \rho \le a\,, \tag{3.30}$$

where $k_{\mathrm{t}\rho}$ is the wave number in ρ-direction within the dielectric cylinder. The factor A_m depends on the excitation and the geometry, and can be seen as a weighting factor of the field values within the cylinder. According to (3.22), the tangential magnetic field component in ϕ-direction can be calculated, and is of the form:

$$H_\phi^{\mathrm{total}}\Big|_{\mathbf{I}_z} = -\frac{j\omega\varepsilon_\mathrm{t}}{k_{\mathrm{t}\rho}} \sum_{m=-\infty}^{\infty} A_m J'_m(k_{\mathrm{t}\rho}\rho)\,\mathrm{e}^{jm(\phi-\phi')}\mathrm{e}^{-jk_z z} \qquad \rho \le a\,, \tag{3.31}$$

If we now suppress the sigma sign, as well as the factors $\mathrm{e}^{jm(\phi-\phi')}\mathrm{e}^{-jk_z z}$, the boundary conditions can be expressed in matrix notation

$$\begin{bmatrix} J_m(k_{\mathrm{t}\rho}a) & -H_m^{(2)}(k_\rho a) \\ \kappa_{\mathrm{t}\varepsilon} J'_m(k_{\mathrm{t}\rho}a) & -\kappa_\varepsilon H'^{(2)}_m(k_\rho a) \end{bmatrix} \cdot \begin{bmatrix} A_m \\ A'_m \end{bmatrix} = \begin{bmatrix} C_m J_m(k_\rho a) \\ \kappa_\varepsilon C_m J'_m(k_\rho a) \end{bmatrix}, \tag{3.32}$$

where the factors $\kappa_{\mathrm{t}\varepsilon}$ and κ_ε are defined by

$$\kappa_{\mathrm{t}\varepsilon} = -\frac{j\omega\varepsilon_\mathrm{t}}{k_{\mathrm{t}\rho}}\,, \tag{3.33}$$

$$\kappa_\varepsilon = -\frac{j\omega\varepsilon}{k_\rho}\,. \tag{3.34}$$

The solution of (3.32) is then given by

$$A_m = \frac{\kappa_\varepsilon C_m J'_m(k_\rho a) H_m^{(2)}(k_\rho a) - \kappa_\varepsilon C_m J_m(k_\rho a) H'^{(2)}_m(k_\rho a)}{\kappa_{\mathrm{t}\varepsilon} J'_m(k_{\mathrm{t}\rho} a) H_m^{(2)}(k_\rho a) - \kappa_\varepsilon H'^{(2)}_m(k_\rho a) J_m(k_{\mathrm{t}\rho} a)}, \tag{3.35}$$

$$A'_m = \frac{\kappa_\varepsilon C_m J'_m(k_\rho a) J_m(k_{\mathrm{t}\rho} a) - \kappa_{\mathrm{t}\varepsilon} C_m J'_m(k_{\mathrm{t}\rho} a) J_m(k_\rho a)}{\kappa_{\varepsilon\mathrm{t}} J'_m(k_{\mathrm{t}\rho} a) H_m^{(2)}(k_\rho a) - \kappa_\varepsilon H'^{(2)}_m(k_\rho a) J_m(k_{\mathrm{t}\rho} a)}. \tag{3.36}$$

3.4 Tangential Longitudinal Orientated Source

Along with the evaluation in [For10], an equal solution of a source orientated in ϕ-direction can be deduced by a simple substitution of $\mathbf{I}_z$ by $\mathbf{I}_\phi$. But—in contradiction to the proposed approach—we restrict our intended solution to the *xy*-plane. This enables the description of on-body paths by a far less extensive solution of the related boundary conditions to determine the connected coefficients. The modified approach uses, in principle, a similar procedure as deduced in terms of the *z*-orientated source. The initial geometry of a ϕ–polarized line source at $\mathbf{r}'(\rho',\phi')$ is shown in Fig. 3-4, while Fig. 3-5 depicts the corresponding tangential longitudinal point source.

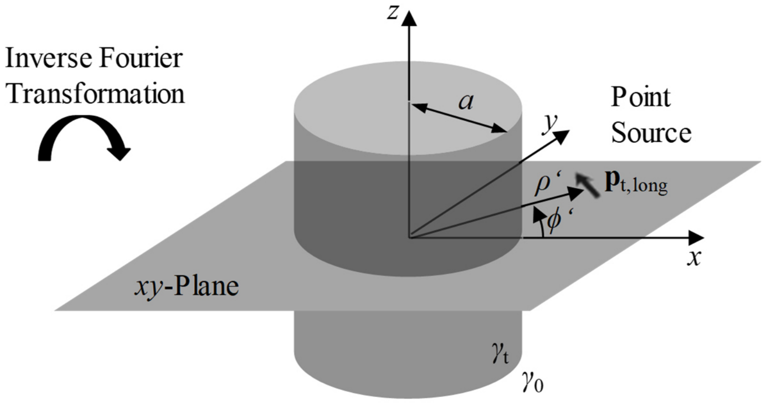

Fig. 3-5 A line source orientated in ϕ-direction is positioned parallel within the *xy*-plane in such a way that a dissipative dielectric cylinder of infinite length is encircled with contestant spacing ρ'-a.

At first, the incident and scattered field components are derived, where the total field results from a superposition of both components. The explicit coefficients are calculated at the end of the paragraph.

3.4.1 Incident Field Components

The incident magnetic field of a ϕ-orientated source can directly be given by neglecting the presence of the dielectric cylinder. This enables, in comparison with (3.20), a similar expression, considering now the z-component of the magnetic incident field. If we restrict our solution space to the xy-plane at $z = 0$, the incident magnetic field only consists of z-component. In this case, it can be described by the use of an infinite number of Bessel functions, with

$$H_z^{\text{inc}}\Big|_{\mathbf{I}_\phi} = \sum_{m=-\infty}^{\infty} D_m J_m(k_\rho \rho)\mathrm{e}^{jm(\phi-\phi')}\mathrm{e}^{-jk_z z} \qquad a \le \rho \le \rho' . \tag{3.37}$$

Here, the factor D_m is defined in relation to the excitation of the source by

$$D_m = \frac{k_\rho I_\phi}{4j} H'^{(2)}_m(k_\rho \rho') . \tag{3.38}$$

Because of the transverse nature of the field components, the electric field can be acquired using (3.16) and (3.17). Since E_z is zero, the equations can be reduced to

$$E_\rho = \frac{\omega \mu m}{k_\rho^2 \rho} H_z \tag{3.39}$$

$$E_\phi = \frac{j\omega\mu}{k_\rho^2} \frac{\partial H_z}{\partial \rho} . \tag{3.40}$$

Therefore, the outer transverse components of the electric field that arises from (3.37), is given by

$$E_\rho^{\text{inc}}\Big|_{\mathbf{I}_\phi} = \frac{\omega\mu_0}{\rho k_\rho^2} \sum_{m=-\infty}^{\infty} m D_m J_m(k_\rho \rho)\mathrm{e}^{jm(\phi-\phi')}\mathrm{e}^{-jk_z z} \qquad a \le \rho \le \rho' \tag{3.41}$$

$$E_\phi^{\text{inc}}\Big|_{\mathbf{I}_\phi} = \frac{j\omega\mu_0}{k_\rho} \sum_{m=-\infty}^{\infty} D_m J'_m(k_\rho \rho)\mathrm{e}^{jm(\phi-\phi')}\mathrm{e}^{-jk_z z} \qquad a \le \rho \le \rho' . \tag{3.42}$$

3.4.2 Scattered Field Components

Analogous to (3.25), the scattered *z*-component of the magnetic field, which results from the presence of the ϕ-directed line source near the dielectric cylinder, can be modeled by Hankel functions. Assuming the geometry-related scaling factor *B*'$_m$ the corresponding formulation yields

$$H_z^{\mathrm{sct}}\Big|_{\mathbf{I}_\phi} = \sum_{m=-\infty}^{\infty} B'_m H_m^{(2)}(k_\rho \rho)\,\mathrm{e}^{jm(\phi-\phi')}\mathrm{e}^{-jk_z z} \qquad \rho \geq a\,. \tag{3.43}$$

Following (3.39) and (3.40), the connected transverse electric field components can be calculated from (3.43), with

$$E_\rho^{\mathrm{sct}}\Big|_{\mathbf{I}_\phi} = \frac{\omega\mu}{k_\rho^2 \rho} \sum_{m=-\infty}^{\infty} m B'_m H_m^{(2)}(k_\rho \rho)\,\mathrm{e}^{jm(\phi-\phi')}\mathrm{e}^{-jk_z z} \qquad \rho \geq a\,, \tag{3.44}$$

$$E_\phi^{\mathrm{sct}}\Big|_{\mathbf{I}_\phi} = \frac{j\omega\mu}{k_\rho} \sum_{m=-\infty}^{\infty} B'_m H'^{(2)}_m(k_\rho \rho)\,\mathrm{e}^{jm(\phi-\phi')}\mathrm{e}^{-jk_z z} \qquad \rho \geq a\,. \tag{3.45}$$

The factor *B*'$_m$ depends on the size of the dielectric cylinder and the dielectric properties. A detailed solution is shown in the following paragraph.

3.4.3 Total Field Components

Corresponding to (3.1) and (3.2), the total electromagnetic field of the ϕ-orientated electric line source results from the superposition of incident and scattered field components. In terms of the magnetic field, with (3.37) and (3.43) in mind, the total field is

$$\mathbf{H}^{\mathrm{total}}\Big|_{\mathbf{I}_\phi} = \left.\begin{bmatrix} 0 \\ 0 \\ \mathbf{H}_z^{\mathrm{inc}} + \mathbf{H}_z^{\mathrm{sct}} \end{bmatrix}\right|_{\mathbf{I}_\phi}. \tag{3.46}$$

The total electric field results from the superposition of (3.42), (3.42), (3.44), and (3.45) and is, therefore,

$$\mathbf{E}^{\text{total}}\Big|_{\mathbf{I}_\phi} = \begin{bmatrix} \mathbf{E}_\rho^{\text{inc}} + \mathbf{E}_\rho^{\text{sct}} \\ \mathbf{E}_\phi^{\text{inc}} + \mathbf{E}_\phi^{\text{sct}} \\ 0 \end{bmatrix}\Bigg|_{\mathbf{I}_\phi} . \tag{3.47}$$

As seen from (3.46) and (3.47), the electromagnetic field within the xy-plane shows, in terms of a ϕ–polarized source, a TM characteristic.

3.4.4 Coefficient Calculation by Applied Boundary Conditions

To determine the scattered field outside the cylinder, the coefficients B'_m are required. Along with the z-orientated source, the coefficient is calculated by the boundary conditions, which are related to the continuous field values of the tangential components. Again, the z-components of the total magnetic field within the cylinder can be assumed as a superposition of Bessel function elements. In case of the line source $\mathbf{I}_\phi$, this results in:

$$H_z^{\text{total}}\Big|_{\mathbf{I}_\phi} = \sum_{m=-\infty}^{\infty} B_m J_m(k_{\text{t}\rho}\rho)\,\mathrm{e}^{jm(\phi-\phi')}\mathrm{e}^{-jk_z z} \qquad \rho \le a , \tag{3.48}$$

where $k_{\text{t}\rho}$ is the wave number in ρ-direction within the dielectric cylinder. The factor B_m depends on the excitation and the geometry. According to (3.40), the tangential electric field component in ϕ-direction can be calculated from (3.48), and is of the form

$$E_\phi^{\text{total}}\Big|_{\mathbf{I}_\phi} = \frac{j\omega\mu_{\text{t}}}{k_{\text{t}\rho}} \sum_{m=-\infty}^{\infty} B_m J'_m(k_{\text{t}\rho}\rho)\,\mathrm{e}^{jm(\phi-\phi')}\mathrm{e}^{-jk_z z} \qquad \rho \le a . \tag{3.49}$$

Analogous to (3.32), we suppress the sigma sign, as well as the factors $\mathrm{e}^{jm(\phi-\phi')}\mathrm{e}^{-jk_z z}$ to formulate the boundary conditions in matrix notation

$$\begin{bmatrix} J_m(k_{\text{t}\rho}a) & -H_m^{(2)}(k_\rho a) \\ \kappa_{\text{t}\mu} J'_m(k_{\text{t}\rho}a) & -\kappa_\mu H'^{(2)}_m(k_\rho a) \end{bmatrix} \cdot \begin{bmatrix} B_m \\ B'_m \end{bmatrix} = \begin{bmatrix} D_m J_m(k_\rho a) \\ \kappa_\mu D_m J'_m(k_\rho a) \end{bmatrix}, \tag{3.50}$$

where the factors $\kappa_{\text{t}\mu}$ and κ_μ are defined by

$$\kappa_{\text{t}\mu} = \frac{j\omega\mu_{\text{t}}}{k_{\text{t}\rho}} , \tag{3.51}$$

$$\kappa_{\mathrm{\mu}} = \frac{j\omega\mu}{k_\rho} . \tag{3.52}$$

The solution of (3.50) is then given by

$$B_m = \frac{\kappa_{\mathrm{\mu}} D_m J'_m(k_\rho a) H_m^{(2)}(k_\rho a) - \kappa_{\mathrm{\mu}} D_m J_m(k_\rho a) H'^{(2)}_m(k_\rho a)}{\kappa_{\mathrm{\mu t}} J'_m(k_{\mathrm{t}\rho} a) H_m^{(2)}(k_\rho a) - \kappa_{\mathrm{\mu}} H'^{(2)}_m(k_\rho a) J_m(k_{\mathrm{t}\rho} a)} , \tag{3.53}$$

$$B'_m = \frac{\kappa_{\mathrm{\mu}} D_m J'_m(k_\rho a) J_m(k_{\mathrm{t}\rho} a) - \kappa_{\mathrm{t\mu}} D_m J'_m(k_{\mathrm{t}\rho} a) J_m(k_\rho a)}{\kappa_{\mathrm{t\mu}} J'_m(k_{\mathrm{t}\rho} a) H_m^{(2)}(k_\rho a) - \kappa_{\mathrm{\mu}} H'^{(2)}_m(k_\rho a) J_m(k_{\mathrm{t}\rho} a)} . \tag{3.54}$$

Chapter 4

Basics of Model Body-Centric Communications and Related Applications

The basis of model body-centric applications comprises the general scope of this chapter. While the previous chapters define elementary theoretical models, the purpose of this chapter is to summarize general modeling aspects. In addition, the basics of a numerical method—the so-called FDTD Method—is introduced, which is used in the following chapters to model complex body-centric propagation scenarios by a combined theoretical-numerical approach as well as to calculate the current distribution on several antenna geometries. One major benefit of this approach is the reduction of the required numerical computation effort, which is typically connected to the solution of body-centric propagation scenarios. On the other hand, the conventional approach, i.e. the numerical solution of corresponding full human body models, provides a solid method of verification of the on-body antenna and propagation theory, discussed hereinafter.

At first, the chapter specifies important electromagnetic field quantities which are valuable measures to characterize underlying propagation effects of body-centric applications. In terms of the previous chapters, in particular, this enables the transfer of the summarized theory to specific applications at commonly used frequencies. In addition, derived from the well-known Debye equation, the Gabriel parameters are referred, which provide the basis to model the dissipative nature of dielectric human body tissues by the Cole-Cole equation. Based on this equation, the values of upper dermis tissue types, e.g. human skin, muscle and fat, are listed, and two numerical anatomically inspired human body phantoms are referred to. At last, general remarks toward the underlying coordinate systems are given, as well as numerical modeling aspects and related numerical effects.

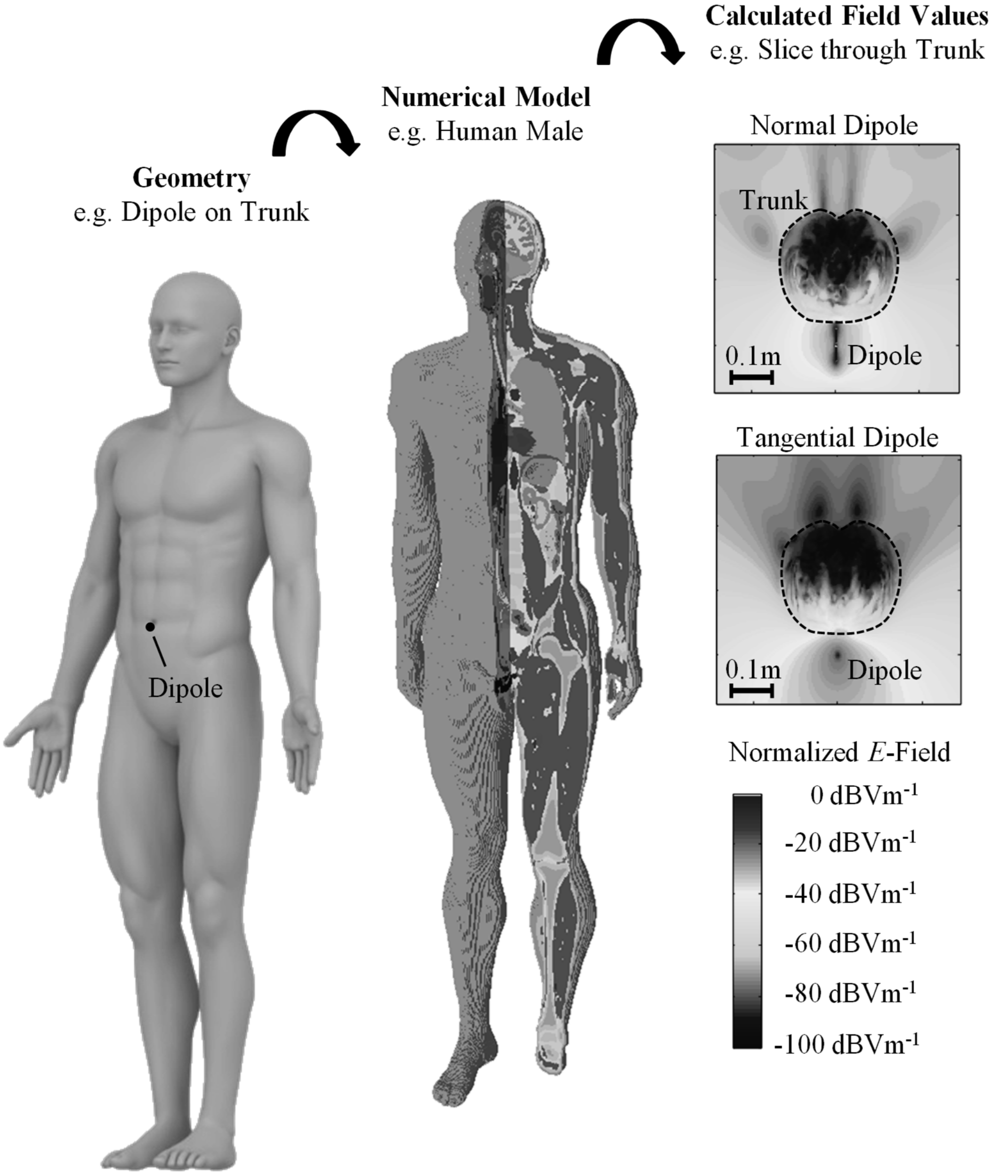
Calculated Field Values
e.g. Slice through Trunk
Numerical Model
e.g. Human Male
Geometry
e.g. Dipole on Trunk
Dipole
Normal Dipole
Trunk
0.1m
Dipole
Tangential Dipole
0.1m
Dipole
Normalized E-Field
0 dBVm-1
-20 dBVm-1
-40 dBVm-1
-60 dBVm-1
-80 dBVm-1
-100 dBVm-1

Fig. 4-1 General steps to model body-centric communication setups: Example shows the radiated electric field component on the IT'IS voxel model 'Duke' at 2.45 GHz for different orientations of a half-wave dipole.

4.1 Propagation Constant and Related Quantities

As seen in Chapter 2, the complex propagation constant is an important measure to define the propagation mechanisms along a dissipative dielectric half-space. Related to [Bal89], one can define the complex propagation constant γ of dissipative dielectric media by its real part, the attenuation constant α, and its imaginary part, the phase constant β, by

$$\gamma = \alpha + j\beta . \tag{4.1}$$

On the other hand, as seen by (2.4), the propagation constant can be defined by the media parameters, i.e. equivalent conductivity σ, permittivity ε and permeability μ, by

$$\gamma^2 = j\omega\mu\sigma - \omega^2\mu\varepsilon . \tag{4.2}$$

Because of the equivalent nature of these definitions, the real and imaginary parts can be led back to the media parameters as well. In this case, the attenuation constant α is defined by

$$\alpha = \omega\sqrt{\mu\varepsilon}\left(\frac{1}{2}\left(\sqrt{1+\left(\frac{\sigma}{\omega\varepsilon}\right)^2}-1\right)\right)^{\frac{1}{2}} \tag{4.3}$$

and the phase constant by

$$\beta = \omega\sqrt{\mu\varepsilon}\left(\frac{1}{2}\left(\sqrt{1+\left(\frac{\sigma}{\omega\varepsilon}\right)^2}+1\right)\right)^{\frac{1}{2}} . \tag{4.4}$$

While the definition of the wave number is typically used to define wave propagation mechanisms, the dissipative nature of human tissues and the related electromagnetic effects may benefit from an equivalent notation in terms of the complex propagation constant, which is related to the wave number k by

$$\gamma = jk . \tag{4.5}$$

4.1.1 Connected Quantities

As demonstrated in [Bal89], many physical propagation phenomena that may occur by the interaction of electromagnetic waves with a dielectric medium can be traced back to the corresponding electromagnetic properties. Therefore, mechanical and electromagnetic properties are linked to each other with the definition of the complex parameters. Owing to the descent of the connected values from TEM wave propagations, these quantities are limited in terms of the complex nature of body-centric propagations. But—as demonstrated later—even single transversal modes, such as the TM or TE case, can be sufficiently approximated with these quantities and so provide feasible measures.

In this case, the wave length λ is connected to the phase constant by

$$\lambda = \frac{2\pi}{\beta} \tag{4.6}$$

and the skin depth δ to the attenuation constant by

$$\delta = \frac{1}{\alpha}. \tag{4.7}$$

The phase velocity c of an electromagnetic wave within a certain medium can be calculated by

$$c = \frac{\omega}{\beta}, \tag{4.8}$$

while the intrinsic impedance is defined by its material parameters by

$$\eta_\mathrm{i} = \sqrt{\frac{j\omega\mu}{\sigma + j\omega\varepsilon}}, \tag{4.9}$$

Considering (4.9), the intrinsic impedance of free space is $\eta_0 = 376.730\ \Omega$. As stated above, the quantities (4.1)–(4.9) are listed at this point only. Their detailed relationship with specific physical properties is extensively discussed in [Bal89].

4.2 Modeling Aspects of Biological Tissues

The dielectric properties of biological tissues have been well investigated during the progress made in the last century. Leading results were introduced by Schwan and Foster in 1957, in which originate the frequency-dependent dielectric properties of biological tissues to physical causes at the cellular level. A valuable reference to their work is given in [Gab94a–c], where the key aspects of their results are listed, summarized and used for further investigations. Related to [Bal89], the general definition of the complex permittivity is given by

$$\varepsilon(\omega) = \mathrm{Re}\{\varepsilon(\omega)\} - j\,\mathrm{Im}\{\varepsilon(\omega)\}. \tag{4.10}$$

While $\varepsilon(\omega) = \varepsilon_0 \cdot \varepsilon_\mathrm{r}(\omega)$, the relative permittivity ε_r can be defined with help of (4.10) by

$$\varepsilon_r(\omega) = \frac{\varepsilon(\omega)}{\varepsilon_0} = \mathrm{Re}\{\varepsilon_\mathrm{r}(\omega)\} - j\,\mathrm{Im}\{\varepsilon_\mathrm{r}(\omega)\}, \tag{4.11}$$

with $\varepsilon_0 = 8.854 \cdot 10^{-12}$ AsV^{-1}m^{-1}. In terms of general mathematical aspects, the sign of the imaginary part of the permittivity, compare (4.10) and (4.11), is in principle free to be chosen. But in general convention, a negative sign is used to express the losses of dissipative dielectrics, and therefore, in terms of a lossless dielectric, the imaginary part vanishes. Related to [Bal89], the complex permeability μ is defined by

$$\mu(\omega) = \mathrm{Re}\{\mu(\omega)\} - j\,\mathrm{Im}\{\mu(\omega)\}. \tag{4.12}$$

With magnetic fields in mind, biological tissues are nearly transparent and lossless and in general agreement [Bal89], it is assumed that the real part of the relative permeability is one and the imaginary part vanishes. Using (4.12), the permeability of biological systems can, therefore, be set to

$$\mu(\omega) \approx \mu_0 = 4\pi \cdot 10^{-7}\,\mathrm{VsA^{-1}m^{-1}}. \tag{4.13}$$

Along with [Bal89], the equivalent conductivity is defined by

$$\sigma = \sigma_s + \sigma_a = \sigma_s + \omega\,\mathrm{Im}\{\varepsilon\}, \tag{4.14}$$

where σ denotes the total or equivalent conductivity. As seen from (4.14), it can be broken down into a static component σ_s and a frequency-dependent component σ_a, the so-called alternating component.

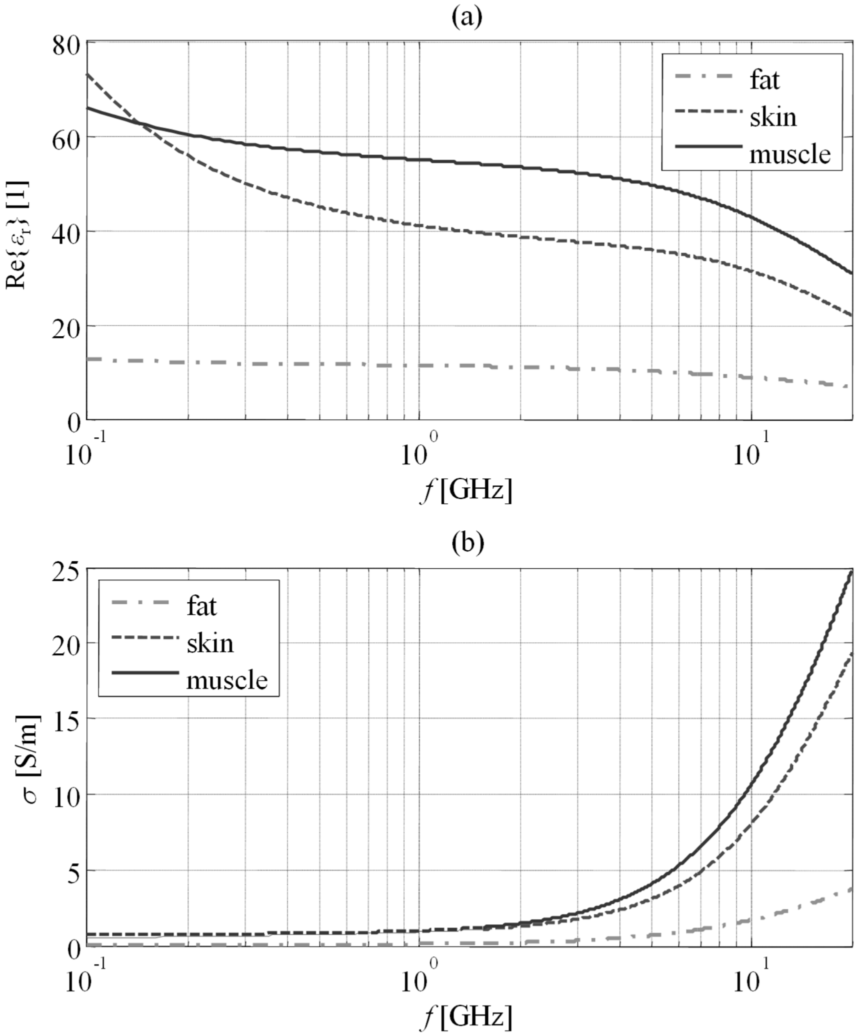

Fig. 4-2 Dielectric properties of human skin, fat, and muscle tissues as functions of the frequency: (a) Real part of the relative permittivity; (b) Equivalent conductivity.

The frequency dependency can be led back to the rotation of dipole momentums, which aspires an alignment corresponding to the alternating field. This effect is also called dielectric hysteresis. The static conductivity of body tissues is in comparison to conductor's low and can primarily lead back to the minor flow of ions. But if the tissues are exposed to an alternating electromagnetic field, the alternating conductivity rises drastically with frequency. In this case, the tissue tends to absorb the energy of an electromagnetic wave, converts it into thermal heat, and, as a result, the penetration depth decreases with increased frequency. As examples, the permittivity and conductivity of muscle, fat and skin tissue are shown in Fig. 4-2.

4.2.1 Cole-Cole Dispersion Approximation and Gabriel Parameters

Along with [Gab94a–c], the relative permittivity below 100 Hz reaches values around 10^6 to 10^7. Above this frequency threshold, the relative permittivity decreases in three significant steps: the so-called α-, β-, γ-dispersion regions. Relatively seen, these relaxation regions occur at low, middle and high frequencies. Within the corresponding frequency regions, the underlying dispersion effect is dominant and other physical effects or the neighboring dispersion regions have a minor impact on the behavior of dielectric properties. An example is the δ-dispersion, which is—in the following considerations—neglected. The γ-dispersion occurs primarily within the gigahertz region and can be traced back to the polarization of water molecules. The β-dispersion dominates the frequency range from a few hundred hertz to the kilohertz range. The major driving physical effect is the polarization of cell membranes, where the membrane limits the ion flow from outer cell regions to the interior. In addition, polarization effects of whole protein- and other macromolecules contribute to this dispersion region. The low frequency α-dispersion region is associated with the diffusion of ions, which is located on the outer cell membrane. And last of all, biological tissues have a low number of mobile ions, which result in a low ionic conductivity. A connected time constant τ can be assigned to each of these relaxation regions. Along to [Gab94c], this leads to the well-known Debye equation, a first order approximation of the complex permittivity ε as function of the angular frequency ω

$$\varepsilon(\omega) = \varepsilon_\infty + \frac{\varepsilon_s - \varepsilon_\infty}{1 + j\omega\tau}, \tag{4.15}$$

where ε_∞ denotes the permittivity at $\omega\tau << 1$ and ε_s the permittivity at $\omega\tau >> 1$. The intensity of the dispersion is hereby given by $\Delta\varepsilon = \varepsilon_\mathrm{s} - \varepsilon_\infty$. To cover more dispersion regions, (4.15) is extended by the distribution parameter α. This factor describes the bandwidth of the related relaxation region and extends the Debye equation to the Cole-Cole equation in the manner of

$$\varepsilon(\omega) = \varepsilon_\infty + \frac{\Delta\varepsilon}{1+(j\omega\tau)^{(1-\alpha)}} . \tag{4.16}$$

To finalize the combination of all three dispersion regions, (4.16) is extended to four summation terms. In addition, the sum is extended by the ionic conductivity term σ_i to cover the static conductivity of body tissues. This leads to the multiple Cole-Cole equation of the form

$$\varepsilon(\omega) = \varepsilon_\infty + \sum_{n=1}^{4} \frac{\Delta\varepsilon_n}{1+(j\omega\tau_n)^{(1-\alpha_n)}} + \frac{\sigma_i}{j\omega\varepsilon_0} . \tag{4.17}$$

The constants $\Delta\varepsilon_\mathrm{n}$, τ_n, α_n with $n = \{1, 2, 3, 4\}$, ε_∞, and σ_i are the so-called Gabriel parameters. Related to [Gab94b–c], measures of various tissues samples enabled the calculation and definition of the parameters of more than 40 different human tissue types. A table of these values is found in Appendix B, while explicit values are also available at [IAP] and [ITI]. In terms of the proceeding content of this thesis, all corresponding dielectric parameters are based on (4.17) and Appendix B.

4.2.2 Properties of Human Dermis Tissues

In terms of modeling aspects of waves that propagate along the human body surface, dermis tissues are of major interest. With this aspect in mind, especially skin, fat, and muscle tissue are focused on, and the frequencies considered correspond to the MICS (Medical Implant Communication Service) standard at 400 MHz, and the ISM (Industrial Medical Scientific) frequencies around 1 GHz, 2.45 GHz and 5.4 GHz. Because of the increasing interest in 60 GHz WBAN applications, this frequency range is considered as well. Using (4.6), (4.7), and (4.17), the connected quantities are derived and listed in Table 4-1.

TABLE 4-1
BASIC QUANTITIES OF HUMAN DERMIS TISSUES

Symbol	Unit	Value to corresponding frequency				
f	GHz	0.4	1	2.45	5.4	60
λ_0	mm	750	300	122	56	5
$\varepsilon_{\mathrm{r,muscle}}$	1	57.1	54.8	52.7	49.0	12.9
$\varepsilon_{\mathrm{r,fat}}$	1	5.58	5.45	5.28	4.99	3.13
$\varepsilon_{\mathrm{r,skin}}$	1	46.8	40.9	38.0	35.4	7.98
σ_{muscle}	$\mathrm{S\,m^{-1}}$	0.80	0.98	1.74	4.49	52.8
σ_{fat}	$\mathrm{S\,m^{-1}}$	0.04	0.05	0.10	0.27	2.82
σ_{skin}	$\mathrm{S\,m^{-1}}$	0.69	0.90	1.46	3.38	36.4
δ_{muscle}	mm	52.6	40.7	22.3	8.36	0.41
δ_{fat}	mm	309	232	117	44.5	3.37
δ_{skin}	mm	55.3	38.5	22.6	9.46	0.47
$\lambda_{\mathrm{muscle}}$	mm	95	40	17	8	1.2
λ_{fat}	mm	313	128	53	25	2.8
λ_{skin}	mm	102	44	19	9	1.4

It can be observed that the properties of muscle and skin tissue correspond to the so-called *high water content* tissues due to their high conductivity and permittivity. At 60 GHz especially, the low penetration depth of the skin tissue indicates that the wave propagation is primarily affected by the skin.

4.3 Coordinate System

As a comparison of Chapters Two and Three reveals, the applied coordinate systems are not congruent with each other: see Fig. 4-1. This can be traced back to the underlying geometries, which can be solved efficiently for the suggested alignment of the coordinate systems. If we restrict our considerations only to the line-of-sight or non-line-of-sight case, this mismatch may be neglected. But if a combined propagation path—which consists of both cases—is required, the coordinate systems have to be adapted to each other.

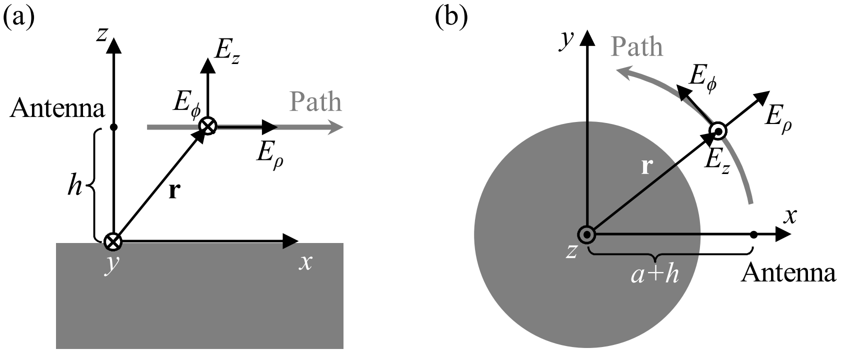
(a)
z
Antenna
h
y
x
r
E_z
E_ϕ
Path
E_ρ
(b)
y
Path
E_ϕ
E_ρ
r
E_z
x
z
a+h
Antenna

Fig. 4-3 Underlying geometries to model on-body propagation paths proceeding parallel above the surface at height *h*; (a) Coordinate system of the planar model, (b) Coordinate system of the cylinder model.

Having on-body propagations in mind, i.e. the propagation path proceeds at a fixed high *h* parallel to the body, an alignment of the coordinate systems orientated to the body surface seems evident. In this case, we can define two tangential and one identical normal orientations in relation to the body surface. Here, the two tangential orientations are differentiated into a longitudinal direction and a transversal one. The suggested definition is shown in Fig. 4-2 with reference to the example of the electric field, where the sub-index "n" denotes a normal orientation and "t" a transversal orientation, which is divided into transversal (trans) and longitudinal (long).

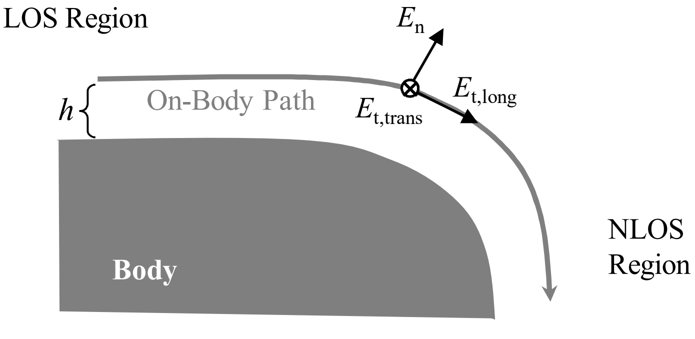
LOS Region
E_n
h
On-Body Path
$E_\mathrm{t,trans}$
$E_\mathrm{t,long}$
NLOS
Region
Body

Fig. 4-4 Coordinate system defined in relation to the body surface to match the line-of-sight (LOS) and non-line-of-sight (NLOS) propagation model in terms of on-body propagation scenarios.

With this definition, we can define identical transformation pairs that transfer the independent systems of Fig. 4-3 into the coincident system, as defined in Fig. 4-4. In the case of the electric field strength, the transformation pairs of Table 4-2 are found.

TABLE 4-2
COORDINATE SYSTEM TRANSFORMATION TABLE

Surface related Coordinates	Planar Model Coordinates	Cylinder Model Coordinates
E_{n}	E_z	E_ρ
$E_{\mathrm{t,trans}}$	E_ϕ	E_z
$E_{\mathrm{t,long}}$	E_ρ	E_ϕ

Equivalent transformation pairs can also be found in case of the magnetic field strength and the power flux density.

4.4 The FDTD Method

Till now, a large variety of numerical methods was used to solve the Maxwell equations for all kinds of high-frequency applications. One of these approaches, a volume-based solution technique approximates the partial differential terms of the Maxwell equations by finite differences in the time domain. The so-called FDTD method (finite differences in time domain) is a well-established numerical approach that can be optimized for a wide range of different geometries and electromagnetic problems. One realization of this method is given by the commercial software EMPIRE XCcell [EMP], which provides the solution to spatial well-known geometries of finite size and defined medium parameters. Within the solution space, precisely defined fields can be determined to excite the structure. During the progress of the thesis, all numerically calculated values and quantities are based on this method.

4.4.1 The Basic FDTD Algorithm

The realization of the FDTD approach shows a wide range of different implementations, while the core algorithm stays the same. The following elementary descriptions are based on [Gus06]. It follows closely the theoretical description, starting with the differential Maxwell equations—which are given by

$$\frac{\partial \mathbf{B}}{\partial t} = -\nabla \times \mathbf{E}, \tag{4.18}$$

$$\frac{\partial \mathbf{D}}{\partial t} = \nabla \times \mathbf{H} - \mathbf{J}. \tag{4.19}$$

If we can assume linear, isotropic, and non-dispersive media, the equations

$$\mathbf{B} = \mu_0 \mu_r \mathbf{H}, \tag{4.20}$$

$$\mathbf{D} = \varepsilon_0 \varepsilon_r \mathbf{E}, \tag{4.21}$$

$$\mathbf{J} = \sigma \mathbf{E} \tag{4.22}$$

Are applicable. Considering (4.18) to (4.22), all field quantities, i.e. electric field **E** and magnetic field **H**, are connected to the medium parameters. In Cartesian coordinates, we can generally define the electric field by

$$\mathbf{E} = E_x \mathbf{e}_x + E_y \mathbf{e}_y + E_z \mathbf{e}_z \tag{4.23}$$

and the magnetic field by

$$\mathbf{H} = H_x \mathbf{e}_x + H_y \mathbf{e}_y + H_z \mathbf{e}_z . \tag{4.24}$$

Related to (4.20), (4.21), and (4.22), the Maxwell differential equations of the electric (4.18) and magnetic field (4.19) can be reformulated into six connected partial differential equations. Under consideration of (4.23) and (4.24), this results in

$$\varepsilon_x \frac{\partial E_x}{\partial t} = \frac{\partial H_z}{\partial y} - \frac{\partial H_y}{\partial z} - J_x , \tag{4.25}$$

$$\varepsilon_y \frac{\partial E_y}{\partial t} = \frac{\partial H_x}{\partial z} - \frac{\partial H_z}{\partial x} - J_y , \tag{4.26}$$

$$\varepsilon_z \frac{\partial E_z}{\partial t} = \frac{\partial H_y}{\partial x} - \frac{\partial H_x}{\partial y} - J_z , \tag{4.27}$$

$$\mu_x \frac{\partial H_x}{\partial t} = \frac{\partial E_y}{\partial z} - \frac{\partial E_z}{\partial y} , \tag{4.28}$$

$$\mu_y \frac{\partial H_y}{\partial t} = \frac{\partial E_z}{\partial x} - \frac{\partial E_x}{\partial z} , \tag{4.29}$$

$$\mu_z \frac{\partial H_z}{\partial t} = \frac{\partial E_x}{\partial y} - \frac{\partial E_y}{\partial x} . \tag{4.30}$$

4.4.2 Discretization in Space

Equations (4.25) to (4.30) are continuous functions of the space coordinates x, y, z and time t. If we now define a spatial sampling size in each coordinate direction, i.e. Δx, Δy, Δz, we can formulate a discrete formulation of the field equations, where the electric and magnetic field components are still orthogonally aligned to each other. Using these subdivisions, the whole solution space can be divided—or *discretized*—into cubic cells, the so-called *voxels*. Within these cells, the electric field components can be found on the edges and the magnetic field components in the face of each cell. With reference to Fig. 4-5, such a cell is illustrated in dark gray. Otherwise, if we chose the light-gray illustrated cell definition, both electric and magnetic field components would switch their relative positions within the cell.

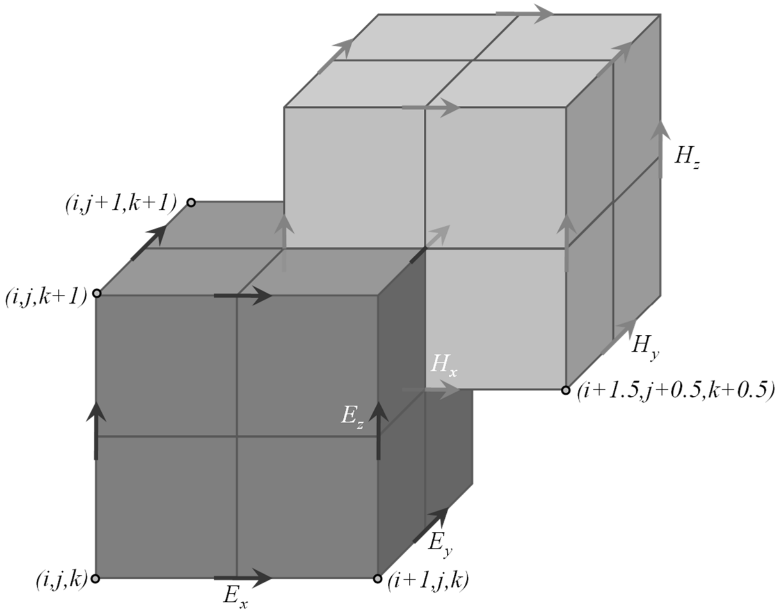

Fig. 4-5 [Gus06]: Electric and magnetic field components within the FDTD mesh. Each cell edge corresponds to spatial coordinate, beginning in this example with (*i*,*j*,*k*) in the left bottom corner.

If we limit our observations to one face of a cell, we can see that each field component of the electric field is encircled by the two transverse field components of the magnetic field and vice versa. This behavior is closer depicted in Fig. 4-6 and is a direct consequence of Faraday's law of induction as well as Ampère's law. Related to [Gus06], this concept was introduced by K. Yee in 1966. Therefore, these spatial cells are called Yee cells.

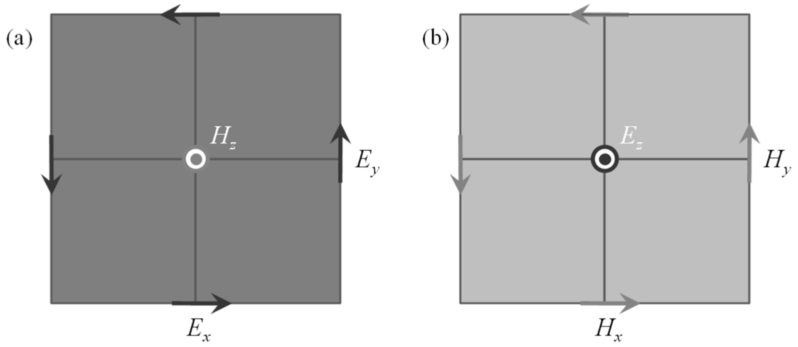

Fig. 4-6 [Gus06]: Two-dimensional slice through a spatial cell to illustrate the circular orientation of the field components to each other: (a) Magnetic field component H_z encircled by transverse electric field components E_x and E_y; (b) Electric field component E_z encircled by transverse electric field components H_x and H_y.

Using this kind of spatial discretization, the electric and magnetic field components are delocalized to each other by a half-cell width. If we now choose the indices (*i*,*j*,*k*) from the natural numbers to allocate the corresponding cells, see Fig.4-5, and assume discrete functions of **E** and **H**, the partial spatial derivations can be replaced by central differences. In this case, the partial differentiation in *x*-direction is

$$\frac{\partial E_{y,i+\frac{1}{2},j+\frac{1}{2},k}}{\partial x} \approx \frac{E_{y,i+\frac{1}{2},j+\frac{1}{2},k} - E_{y,i,j+\frac{1}{2},k}}{\Delta x}, \tag{4.31}$$

$$\frac{\partial E_{z,i+\frac{1}{2},j,k+\frac{1}{2}}}{\partial x} \approx \frac{E_{z,i+1,j,k+\frac{1}{2}} - E_{z,i,j,k+\frac{1}{2}}}{\Delta x}, \tag{4.32}$$

$$\frac{\partial H_{y,i,j,k+\frac{1}{2}}}{\partial x} \approx \frac{H_{y,i+\frac{1}{2},j,k+\frac{1}{2}} - H_{y,i-\frac{1}{2},j,k+\frac{1}{2}}}{\Delta x}, \tag{4.33}$$

$$\frac{\partial H_{z,i,j+\frac{1}{2},k}}{\partial x} \approx \frac{H_{z,i+\frac{1}{2},j+\frac{1}{2},k} - H_{z,i-\frac{1}{2},j+\frac{1}{2},k}}{\Delta x}. \tag{4.34}$$

An approximation of the spatial derivation $\partial Ey/\partial$x by the difference $\Delta E_y/\Delta x$ is shown in Fig. 4-7. Therefore, the discrete function ΔE_y is known for each sampled step of size Δx in *x*-direction. The spatial differences in the middle of each interval can be estimated by a linear interpolation between the direct left- and right-sided neighbors. Corresponding expressions can be found in *y*- and *z*-directions.

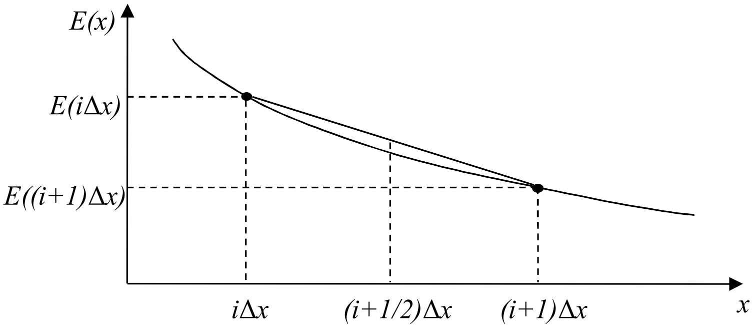

Fig. 4-7 [Gus06]: Approximation of the partial derivative by differences and linear interpolation of values at half-cell width.

4.4.3 Discretization in Time

Related to the Maxwell equations [Gus06], the time derivative of the electric field is linked to the spatial derivative of the magnetic field. In reverse, the time derivative of the magnetic field is connected to the curl of the electric field. To find a time-dependent expression of the field functions, the time width Δt is defined. In the next step, the time derivative is exchanged by differences, while the electric field is calculated at each time step $n \cdot \Delta t$, and the magnetic field vales are calculated at step sizes that are relatively shifted by a half step, i.e. at $(n + 0.5) \cdot \Delta t$. In this case, the time derivative of the electric field can be approximated by

$$\left. \frac{\partial E_{x,i+\frac{1}{2},j,k}}{\partial t} \right|_{t=(n+\frac{1}{2})\Delta t} \approx \frac{1}{\Delta t} \left(E^{n+1}_{x,i+\frac{1}{2},j,k} - E^{n}_{x,i+\frac{1}{2},j,k} \right), \tag{4.35}$$

$$\left. \frac{\partial E_{y,i,j+\frac{1}{2},k}}{\partial t} \right|_{t=(n+\frac{1}{2})\Delta t} \approx \frac{1}{\Delta t} \left(E^{n+1}_{y,i,j+\frac{1}{2},k} - E^{n}_{y,i,j+\frac{1}{2},k} \right), \tag{4.36}$$

$$\left.\frac{\partial E_{z,i,j,k+\frac{1}{2}}}{\partial t}\right|_{t=(n+\frac{1}{2})\Delta t} \approx \frac{1}{\Delta t}\left(E^{n+1}_{z,i,j,k+\frac{1}{2}} - E^{n}_{z,i,j,k+\frac{1}{2}}\right). \tag{4.37}$$

In (4.35) to (4.37), the upper indices of the electric field values define the corresponding time step, while the lower index describes the spatial position within the FDTD mesh. In the same way, the magnetic field can be found with

$$\left.\frac{\partial H_{x,i,j+\frac{1}{2},k+\frac{1}{2}}}{\partial t}\right|_{t=n\Delta t} \approx \frac{1}{\Delta t}\left(H^{n+\frac{1}{2}}_{x,i,j+\frac{1}{2},k+\frac{1}{2}} - H^{n-\frac{1}{2}}_{x,i,j+\frac{1}{2},k+\frac{1}{2}}\right), \tag{4.38}$$

$$\left.\frac{\partial H_{y,i+\frac{1}{2},j,k+\frac{1}{2}}}{\partial t}\right|_{t=n\Delta t} \approx \frac{1}{\Delta t}\left(H^{n+\frac{1}{2}}_{y,i+\frac{1}{2},j,k+\frac{1}{2}} - H^{n-\frac{1}{2}}_{y,i+\frac{1}{2},j,k+\frac{1}{2}}\right), \tag{4.39}$$

$$\left.\frac{\partial H_{z,i+\frac{1}{2},j+\frac{1}{2},k}}{\partial t}\right|_{t=n\Delta t} \approx \frac{1}{\Delta t}\left(H^{n+\frac{1}{2}}_{z,i+\frac{1}{2},j+\frac{1}{2},k} - H^{n-\frac{1}{2}}_{z,i+\frac{1}{2},j+\frac{1}{2},k}\right). \tag{4.40}$$

Considering (4.35) to (4.40), it is obvious that the current flow density has to be calculated at the same time step indices as the magnetic field values. Therefore, the current flow density is calculated at (n + 0.5)·Δt by averaging the electric field values at neighboring indices. By this, the current flow density **J** is given by

$$J^{n+\frac{1}{2}}_{x,i+\frac{1}{2},j,k} \approx \frac{1}{2}\sigma_x\left(E^{n+1}_{x,i+\frac{1}{2},j,k} + E^{n}_{x,i+\frac{1}{2},j,k}\right), \tag{4.41}$$

$$J^{n+\frac{1}{2}}_{y,i,j+\frac{1}{2},k} \approx \frac{1}{2}\sigma_y\left(E^{n+1}_{y,i,j+\frac{1}{2},k} + E^{n}_{y,i,j+\frac{1}{2},k}\right), \tag{4.42}$$

$$J^{n+\frac{1}{2}}_{z,i,j,k+\frac{1}{2}} \approx \frac{1}{2}\sigma_z\left(E^{n+1}_{z,i,j,k+\frac{1}{2}} + E^{n}_{z,i,j,k+\frac{1}{2}}\right). \tag{4.43}$$

The expressions of (4.35) to (4.43) that have been developed can now be used to reformulate (4.25) into

$$\frac{\varepsilon_x}{\Delta t}\left(E^{n+1}_{x,i+\frac{1}{2},j,k}-E^{n}_{x,i+\frac{1}{2},j,k}\right)=\frac{H^{n+\frac{1}{2}}_{z,i+\frac{1}{2},j+\frac{1}{2},k}-H^{n+\frac{1}{2}}_{z,i+\frac{1}{2},j-\frac{1}{2},k}}{\Delta y}+$$

$$-\frac{H^{n+\frac{1}{2}}_{y,i+\frac{1}{2},j,k+\frac{1}{2}}-H^{n+\frac{1}{2}}_{y,i+\frac{1}{2},j,k-\frac{1}{2}}}{\Delta z}-\frac{1}{2}\sigma_x\left(E^{n+1}_{x,i+\frac{1}{2},j,k}+E^{n}_{x,i+\frac{1}{2},j,k}\right). \tag{4.44}$$

A rearrangement delivers then the x-component of the electric field as a function of previous electric and magnetic field values with

$$E^{n+1}_{x,i+\frac{1}{2},j,k}=\left(\frac{1-\frac{\sigma_x\Delta t}{2\varepsilon_x}}{1+\frac{\sigma_x\Delta t}{2\varepsilon_x}}\right)E^{n}_{x,i+\frac{1}{2},j,k}+$$

$$+\left(\frac{\frac{\Delta t}{\varepsilon_x}}{1+\frac{\sigma_x\Delta t}{2\varepsilon_x}}\right)\left(\frac{H^{n+\frac{1}{2}}_{z,i+\frac{1}{2},j+\frac{1}{2},k}-H^{n+\frac{1}{2}}_{z,i+\frac{1}{2},j-\frac{1}{2},k}}{\Delta y}-\frac{H^{n+\frac{1}{2}}_{y,i+\frac{1}{2},j,k+\frac{1}{2}}-H^{n+\frac{1}{2}}_{y,i+\frac{1}{2},j,k-\frac{1}{2}}}{\Delta z}\right). \tag{4.45}$$

This recursive expression can be also found for the remaining electric and magnetic field values and are listed in Appendix D. The algorithm described by these equations is the so-called Leap Frog algorithm. Following this algorithm, the electric and magnetic field values of the spatial mesh grid can be calculated for discrete time values. If now, we assume the time step $t = 0$, a finite excitation is initiated, the resulting reaction of further time steps of the defined geometry can be calculated within the defined space volume. A schematic illustration of the algorithm is shown in Fig. 4-8.

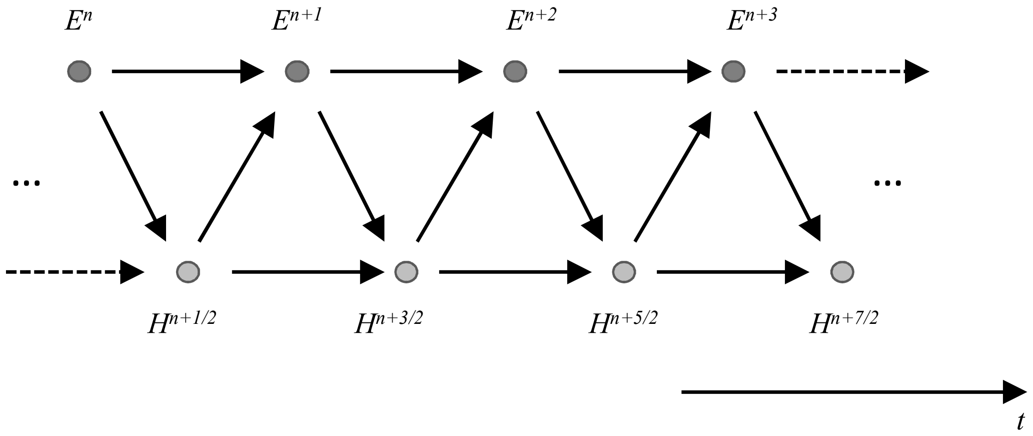

Fig. 4-8 [Gus06]: Leap Frog Method; Electric field values are calculated at time steps $t = n \cdot \Delta t$ and magnetic field values at $t = (n + 0.5) \cdot \Delta t$.

4.4.4 Numeric Stability and Dispersion

The equations given above represent the core algorithm of the FDTD method. To ensure sufficient reliability of the technique, certain criteria relating the discretization in time and space have to be fulfilled. Along with [Gus06], one major criterion to ensure numerical stability is the limitation of the time step size Δt. In terms of an equally discretized solution space, the Courant criterion limits the step size by

$$\Delta t \leq \frac{1}{c\sqrt{\left(\frac{1}{\Delta x}\right)^2 + \left(\frac{1}{\Delta y}\right)^2 + \left(\frac{1}{\Delta z}\right)^2}}, \tag{4.46}$$

where Δx, Δy, Δz defines the spatial increment in x-, y-, and z-direction and c the velocity of the electromagnetic wave in the corresponding medium as defined by (4.8). Equation (4.46) ensures that the distance $c \cdot \Delta t$ does not exceed the diagonal of a discretization cell. In other words, the fact that the passed distance of an electromagnetic wave within the time Δt is smaller than a cell width is ensured. As a consequence thereof, a smaller resolution of the discretization size implies a smaller time step size and so more iterations of the algorithm to complete. If, for instance, the transit of an electromagnetic wave through the solution space has to be solved, the time required to travel through the space is subdivided into more time steps if the spatial resolution is reduced. As seen from Table 4-1, the dielectric parameters of human tissues are a function of the frequency and, considering (4.8), the related change in the propagation velocity has to be considered if a simulating geometry has to be solved that includes dissipative human body tissues.

Another detailed analysis of the FDTD method shows that the spatial discretization can lead to anisotropic propagation velocities of a propagating wave [Gus06], the so-called numeric dispersion. While this effect does not necessarily cause numeric stability problems, the different propagation velocities in different directions can cause—especially within large solution spaces—significant errors of the calculated electromagnetic field values. To limit this error, the condition

$$\max(\Delta x, \Delta y, \Delta z) \leq \frac{\lambda_{\min}}{10}, \tag{4.47}$$

should be fulfilled. This means that the largest discretization width should not exceed a tenth of the smallest occurring wave-length $\lambda_{\min}$ of the media within the solution space.

4.4.5 Anatomical Human Body Models

Based on [Chr10] and [Gos14], the following numerical calculations use anatomically inspired human phantoms to model the electromagnetic behavior of the human body. Based on magnetic resonance imaging data of various probands, the underlying human bodies are reconstructed by voxel models, where each corresponding spatial cell is assigned to the connected dielectric tissue type. The resolution cell width of the used voxel models is limited to 0.5 mm, while the used voxel size in this thesis is 2 mm. The dielectric properties of each tissue type are calculated by the Cole-Cole Equation (4.17) for the solution frequency of interest using the Gabriel parameters of Appendix B.

As seen in Fig. 4-9, two models are used—a male model called *Duke* and a female model called *Ella*. Both phantoms are integrated into the commercial software Empire [EMP], as well as the dielectric property estimation by the Gabriel parameters. Another feature, which is implemented into this simulation environment, is the so-called “body poser.” This algorithm enables the adaption of different body postures of the voxel phantom, i.e. a wide range of other postures can be emulated [EMP]. With this, even complex position variations—e.g. walking, running and sitting—can be modeled.

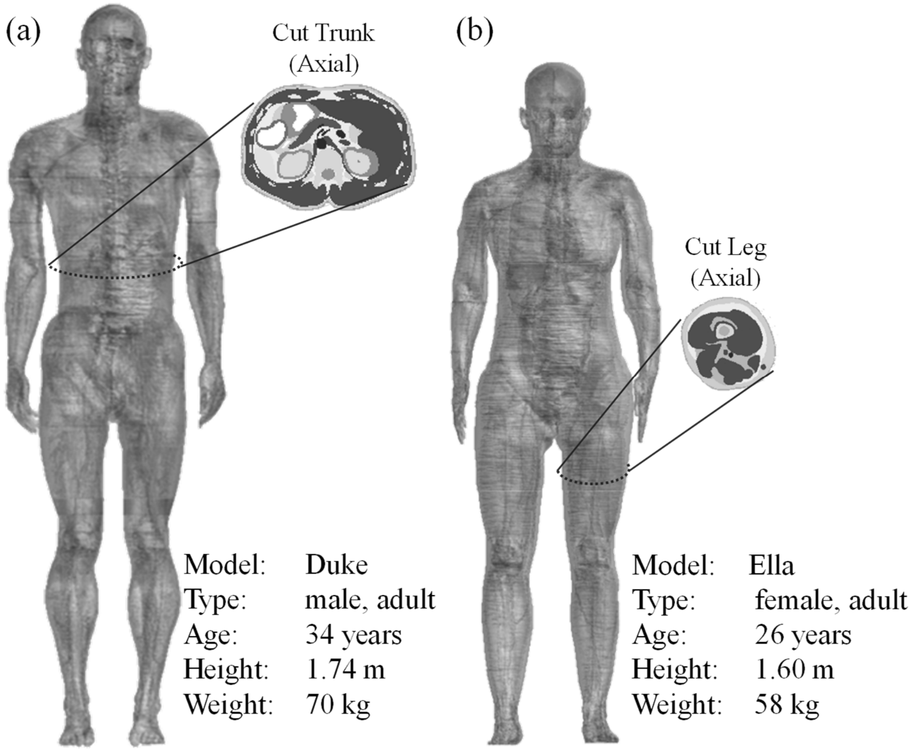
(a)
Cut Trunk
(Axial)
(b)
Cut Leg
(Axial)
Model: Duke
Type: male, adult
Age: 34 years
Height: 1.74 m
Weight: 70 kg
Model: Ella
Type: female, adult
Age: 26 years
Height: 1.60 m
Weight: 58 kg

Fig. 4-9 Numerical human body phantoms: (a) Male model 'Duke'; (b) Female model 'Ella'.

4.4.6 Vast Solution Spaces and Appropriate Boundary Conditions

Related to the principles of the FDTD method, several boundary conditions are available to enclose the numerical simulation space [Gus06]. Typical conditions are, for instance, a perfect electric conductor (PEC), a specific impedance matched (in general, the intrinsic free space impedance η_0), or a so-called absorbing boundary. While the first and second conditions are valuable for specific geometries, the last condition is very important to emulate general free space conditions. Taking the third boundary condition into consideration, a finite number of layers accomplishes an impedance matching from the related medium impedance to PEC conditions, thereby enabling the termination of an electromagnetic wave of arbitrary incidence angle. The numbers of additional cell layers, which are necessary to realize the matching, depend on the incident angle. Within Empire, the number can be chosen between 4 and 16 [EMP]. In general, an acute angle requires more layers than a perpendicular incident angle. Such acute angles occur in the first place if the simulation space is extremely expanded in one direction, i.e. the ratio between the edge lengths is very high and may result in non-negligible numerical errors. To compensate this effect, the sizes in the two remaining space directions have to be increased as well. Having the modeling of wireless applications under the consideration of whole human bodies in mind, this can result in vast numerical models. To investigate the influence of these parameters in relation to the numerical error, a specific numerical setup is used.

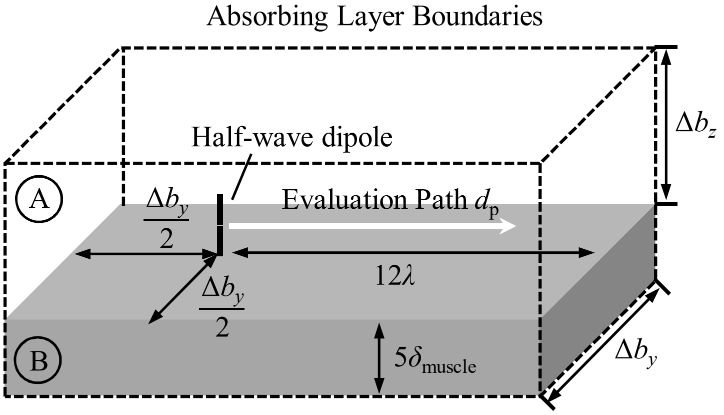

Fig. 4-10 Evaluation setup to determine the numerical error arising from solution space size.

As shown in Fig. 4-10, a normally orientated half-wave dipole is positioned above a dissipative dielectric half space, Medium A, with an effective antenna height of a quarter free space wave length at $f = 2.45$ GHz. The dielectric parameters of the ground layer, Medium B, are set to muscle tissue. The evaluation path proceeds parallel above the surface at the effective antenna height, where the numerically calculated electric field is compared with the analytically calculated field values based on the Bannister equations of Appendix C. The dimension of the solution space is dependent on Δb_y and Δb_z, as defined in Fig. 4.10, while the length is fixed to 12 wave lengths and the thickness of the muscle tissues is set to five penetration depths. The boundary conditions are set to absorbing layers, and the absolute difference between the numerically and theoretically calculated electric fields is calculated at $r = 4\lambda$, $r = 6\lambda$, and $r = 12\lambda$. The results are shown in

Table 4-3 for eight layers and in Table 4-4 for 16 layers.

TABLE 4-3
ABSOLUTE DIFFERENCE, 8 LAYERS

Δb_y [λ^{-1}]	Δb_z [λ^{-1}]	Absolute Difference [dBV]		
		$r(4\lambda)$	$r(6\lambda)$	$r(12\lambda)$
1	0.5	0.078	0.98	5.74
1	1	0.086	1.05	6.51
1	3	0.077	1.04	6.21
4	0.5	0.014	0.03	0.72
4	1	0.023	0.01	0
4	3	0.019	0.05	0.25
10	0.5	0.014	0.02	0.34
10	1	0.023	0.01	0
10	3	0.015	0.02	0.13

TABLE 4-4
ABSOLUTE DIFFERENCE, 16 LAYERS

Δb_y [λ^{-1}]	Δb_z [λ^{-1}]	Absolute Difference [dBV]		
		$r(4\lambda)$	$r(6\lambda)$	$r(12\lambda)$
1	0.5	0.069	0.11	1.96
1	1	0.063	0.08	1.92
1	3	0.071	0.09	1.91
4	0.5	0.03	0	0
4	1	0.023	0.01	0
4	3	0.036	0.01	0.02
10	0.5	0.03	0	0.16
10	1	0.023	0.01	0.11
10	3	0.031	0	0.1

As can be seen from Table 4-3 and Table 4-4, the number of layers has a major effect on the results if the width and height of the evaluation path are small in comparison with the length, especially at far path distances. Related to the dipole orientation, the simulation space width has a stronger influence on the error as the height. The following numerical derivations within the thesis use a tradeoff between these values, and therefore, 16 absorbing layer are used in accordance with a setup space, which is set to $\Delta b_y = 4\lambda$ and $\Delta b_z = 1\lambda$. Notice that if a dissipative dielectric is in contact with an absorbing boundary condition, this may lead to addition numerical effects. These effects can be neglected if a setup is chosen analogous to Fig. 4-10. But in terms of in-body scenarios, i.e. the antenna as well as the path under test is located within the dissipative body tissue, these setups may lead to severe resonance effects. These harmonics can lead back to an electrical short circuit of the boundary by the conductive dielectric medium. To avoid these harmonics, an FDTD excitation pulse with a small DC component should be used.

4.4.7 End Criterion Estimation

The recursive nature of the FDTD method implies the need for an end criterion to finish the calculation of the electromagnetic field values by the equations of Appendix D. Therefore, it is necessary to find the minimum number of time steps when the results converge to the geometry-related solution. One method to identify whether the algorithm has achieved that goal is to test the remaining energy [Gus06]. Here, it has to be ensured that the remaining energy of the defined excitation at $t = 0$ vanishes within the solution space. Otherwise, the calculated field values suffer from non-negligible numerical errors. In general, the underlying FDTD software [EMP] estimates the remaining energy, which is stored within the electromagnetic field of the solution space, by reference measurements. These reference measurements are realized by the calculated difference between the initialized excitation pulse and the currently approaching energy at the excitation position. If this difference falls below a certain threshold, the algorithm is terminated at the corresponding time step. This end criterion is convenient for solutions of geometries sizes around a few wave lengths, i.e. the energy distribution within the solution space can be assumed to be equal. But having a solution space in the scale of the human body in mind, this definition may cause large numerical errors. If we, for instance, assume a propagation path along the front side of the human body, e.g. from upper chest to leg of the 'Duke' model of Fig. 4-9, the related distance is approximately 1.5 m. In terms of the

ISM frequency band at 2.45 GHz, this corresponds to about 12 free space wave lengths. To compensate this influence, the related end criterion has to be adjusted, i.e. the termination threshold has to be lowered, or the number of time steps has to be increased. In practice, the related adaption of the threshold in terms of simulation space and frequency is difficult to be realized by this method. Therefore, the minimum number of required time steps is approximated by the geometry itself. The spatial extension of the numerical simulation grid, seen in terms of electrical wave lengths, increases with frequency. As seen in Table 4-1, the dielectric losses within the human body increase with frequency as well and so cause a rapid decay of the stored field energy within the phantom model. This fact implies that the phantom can be treated as non-resonant dielectric structure. Therefore, the accuracy of the numerical algorithm within the free space medium around the phantom suffers more from an electrical large simulation space as the interior of the body would. Assuming a dielectric medium, a traveling electromagnetic wave takes the time increment ∂t to pass the distance increment ∂r. As seen in [Bal89], this is related to the propagation velocity c by

$$\partial t = \frac{\partial r}{c}\,. \tag{4.48}$$

If we define the maximum possible propagation distance $L_{\max}$ within the solution space, the related time t can be calculated for free space conditions using (4.48) by

$$t = \frac{L_{\max}}{c_0}\,, \tag{4.49}$$

where $c_0 \approx 3 \cdot 10^8$ m/s is the propagation velocity of free space. Assuming the cubic FDTD mesh structure, $L_{\max}$ can be approximated by the diagonal width of the cubic simulation space. as defined in Fig. 4-11. In this thesis, it is assumed that the FDTD algorithm can be terminated if a related electromagnetic wave has passed $4 \cdot L\text{max}$. If we assume the example of Fig. 4-11 and follow (4.49), the algorithm ends after 26 ns. This value can be seen as the upper bound. If the space can be reduced, e.g. to a specific body part, (4.49) yields a shorter end criterion time value, which can lead back to the reduced values of $L_{\max}$.

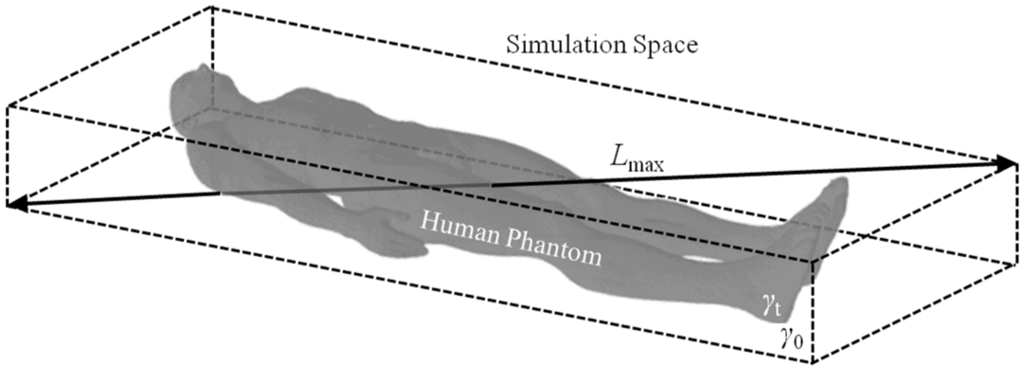

Fig. 4-11 End criterion definition of the FDTD method in terms of body-centric wireless applications: Approximation of the maximum spatial size $L_{\max} \approx 2$ m of the Duke phantom.

4.4.8 Estimation of Memory Allocation

As seen from the core algorithm equations of Appendix D, the FDTD method requires three electric and three magnetic field values for each spatial mesh point to process the recursive calculation for each time step. As seen above, the spatial dimension of the mesh depends on the connected medium parameters as well as on the frequency. At high frequencies, in particular, the demand for allocated memory increases drastically, and so the numerical modeling of full human body models becomes resource- and time-consuming. Related to [EMP], Empire requires 4 Bytes to store an electromagnetic field value as float value, i.e. each mesh node requires 24 Bytes of allocated memory. In principle, the same memory has to be allocated to store the tissue parameters of each cell, where the used method holds these values on the fly with a caching rate of about 90 %. Eventually, the PML boundary require 48 byte to store the complex values of each layer mesh cell. Table 4-5 shows the memory demand as a function of the frequency. The underlying calculation assumes a simulation space size of 0.568 m x 0.34 m x 1.878 m (Duke voxel model), which is equally divided into underlying mesh cells. Corresponding to (4.47), 10 cells per wave length are assumed, while the wave length of muscle tissue is presumed. Furthermore, at each boundary, there are 10 addition cells envisaged to represent the boundary and related spacing issues.

TABLE 4-5
ESTIMATED MEMORY DEMAND OF THE DUKE PHANTOM

f [GHz]	Number of field values [1]	Estimated Memory [GB]
0.10	104,629	0.0047
1.00	8,329,422	0.2774
5.00	660,113,558	18.610
10.0	4,228,023,277	115.76
60.0	199,595,578,933	5324.1

Chapter 5

Modeling Line-of-Sight On-Body Propagations

With wireless body-centric communications in mind, the close proximity of the human body may have a significant impact on the antenna as well as on the channel properties. This fact links both characteristics to each other and increases the effort in terms of a purposeful antenna design. A straightforward solution is the consideration of the whole propagation scenario, which includes the antennas as well as the propagation medium, i.e. the human body in general. Therefore, a scenario-specific description might be provided by measurements or numerical calculations of the entire transfer function, including transmitting antenna, channel and receiving antenna [Abb12]. More general information on how different configurations of antennas and channel behave can be obtained by investigating various setups using statistical analysis [Gal11]. In this case, specific parameters are varied, such as body shape, frequency, body position, antenna position or polarization. As a consequence thereof, the combination variety of all parameters may lead to resource-consuming measurement campaigns. Moreover, the achieved results are restricted to the underlying setup parameters and are, in principle, limited if a transfer to other applications is intended, as the impact of the different variation parameters is a function of the other parameters as well. Therefore, all suitable setup configurations have to be systematically modeled to estimate the general performance of a featured application. Unfortunately, these methods yield only implicit information in respect of the entire system design and it is difficult to draw conclusions e.g. about an optimized antenna design. Therefore, more analytical insights would be desirable.

To deal with this problem, a modeling technique would be feasible that is defined corresponding to the free space antenna theory, i.e. to separate the wireless propagation link into independent antenna and channel parameters to achieve an equivalent model with replaceable and scalable parameters. As seen in Fig. 5-1, the following chapter aims for separated antenna and channel characterization theory for line-of-sight on-body applications.

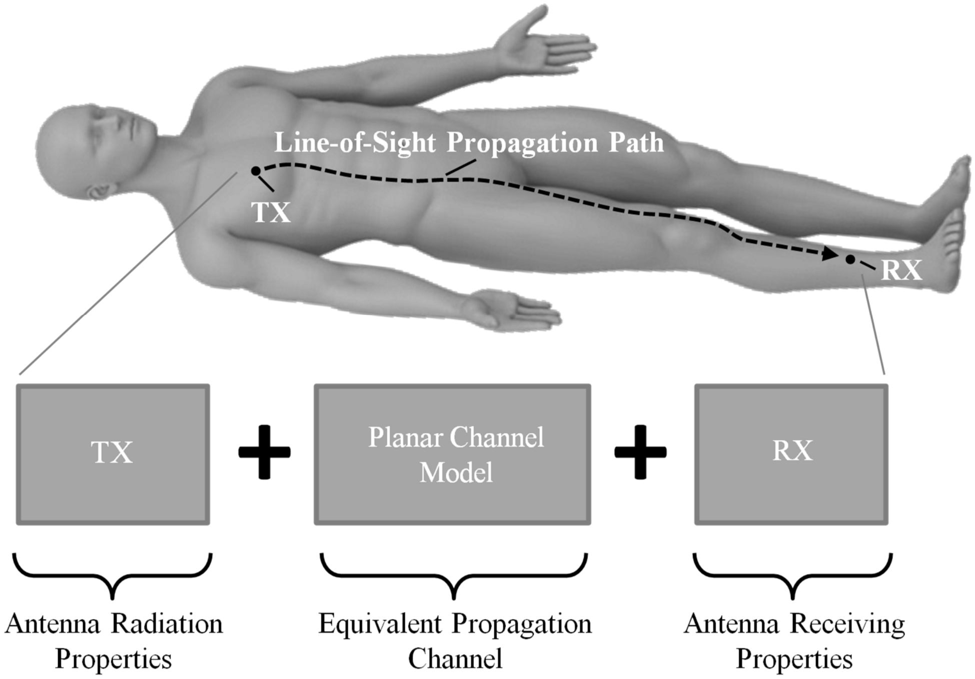
Line-of-Sight Propagation Path
TX
RX
TX
Planar Channel Model
RX
Antenna Radiation Properties
Equivalent Propagation Channel
Antenna Receiving Properties

Fig. 5-1 Systematic modeling of a wireless on-body propagation link: Separated equivalent antenna and channel models are combined to describe the propagation path.

The first part discusses the general feasibility of transferring the Sommerfeld problem to body-centric communications. The second part utilizes common quantities that are associated with this theory, such as the numerical distance of Sommerfeld, to discuss the line-of-sight on-body propagation channel for different BAN frequencies and tissue types. In this context, the radiated electromagnetic field is discussed with reference to the example of three basic dipole orientations that are later used to describe the radiated field of arbitrarily shaped on-body antennas. The next step combines the knowledge of the radiated field species with its related basic dipole configurations to define two equivalent dipole sources. Related to these equivalent sources, the on-body directivity is defined as well as the effective antenna area. Then, the defined on-body antenna parameters enable the calculation of the path gain, which is discussed for various dipole configurations, as well as for a planar inverted-F antenna. A final evaluation of the suggested theory in terms of the full human body is done numerically as well as by a measurement setup in an anechoic chamber.

The general derivations of this chapter strictly follow [Gri14b].

5.1 The Planar Model in Relation to Full Human Body Models

As seen in Chapter 2, a well-established approach to model terrestrial wireless communication links is given by the solution to the Sommerfeld problem. Nevertheless, the general assumption to model the complex topology of the earth by a homogeneous planar model seems far-fetched at first. But, as demonstrated by several contributors, e.g. K. Norton [Nor41], in case of terrestrial propagations, the model is capable of describing the average behavior of the assumed model quite well. Local contortions—for instance, resulting from mountains and valleys, and regional fluctuations of the ground parameters, e.g. related to wood and lake areas—may disturb the local accuracy of the suggested model, but in relation to the whole propagation distance, these effects are minor fluctuations of the average behavior. Therefore, the transfer of this theory to the topology of the human body and the general field of body-centric wireless applications as well seems promising.

Within the scope of WBAN applications, the corresponding Norton theory has again gained attention. Here, the tissue of the body acts as a dissipative ground and due to the aim for low profile antennas, such as textile antennas [Cha12], the Sommerfeld approach seems inevitable. In this context, the radiation mechanism of a body-worn antenna is discussed at an operation frequency of 2.45 GHz for electrical small dipoles [Akh10]. The corresponding results are also applied to the design of a 60 GHz on-body antenna, which aims for a strong Norton surface wave excitation in [Wu10]. An analytical propagation model for the frequency range of 1 GHz to 10 GHz of a stratified skin, fat, and muscle tissue ground is presented in [Lea09]. This model is based on the solution of the Sommerfeld approach by J. R. Wait [Wai96] for electrically small dipole antennas that are positioned vertically on the ground. Other approaches aim at an on-body far field description by the Norton theory to deduce body-centric antenna parameters and propagation models [Gri12a].

5.1.1 Comparison between Theoretical and Numerical Models

In addition to the references given above, the feasibility of the planar model of Chapter 2 is shown by a numerical on-body example setup. The considered propagation paths lead along the human voxel phantoms “Duke” and “Ella,” and are numerically calculated by the FDTD method. In addition, the theoretically modeled electromagnetic field of an equivalent scenario is calculated by the Poynting vector, using (2.70) and (2.71). In general, the large variety of wireless body-centric application leads to a wide spectrum of possible scenarios. In terms of this thesis, the investigated scenarios are related to the ISM band at 2.45 GH and, therefore, cover one of the most utilized frequency bands. Moreover, the curvature and radii of the human body is within the scale of free space wave length and, therefore, a challenging test of the suggested planar model in relation to the anatomy of the human body. The underlying numerical voxel phantoms and defined propagation paths are shown in Fig. 5-2. The effective antenna height is set to a quarter free space wavelength.

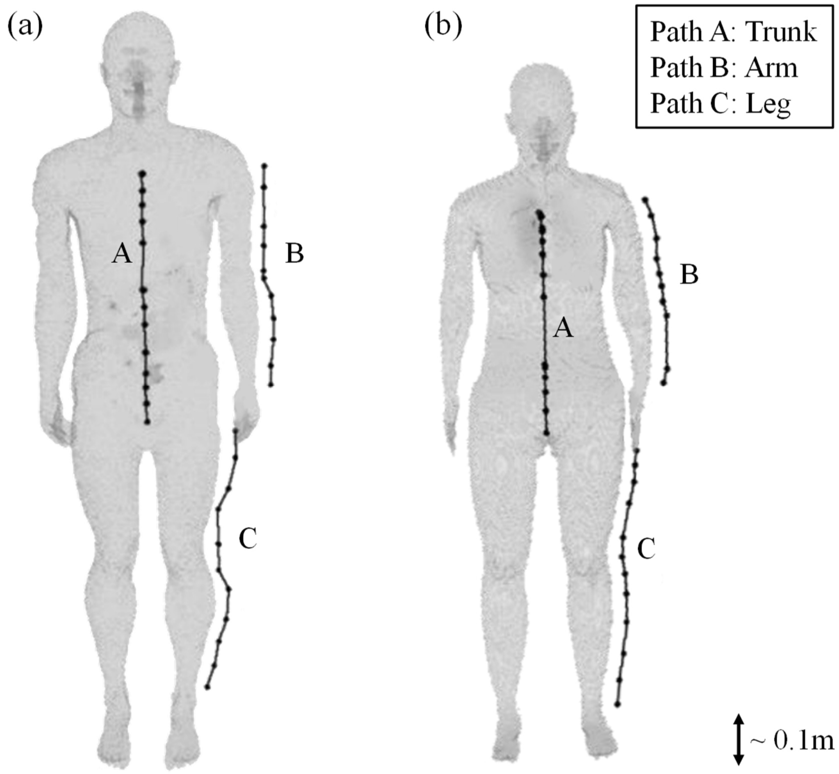

Fig. 5-2 Defined evaluation paths on numerical voxel model (a) Duke, and (b) Ella on trunk, arm, and leg body parts.

This value is chosen as an upper bound, while, in reality, most applications can be assumed to be tightly bound to the body. To enable a direct comparison of the results with the Bannister solution, normal orientated half-wave dipoles are used. The power flux density of the defined paths is shown in Fig. 5-3, where the planar model values are based on the field quantity terms of Table 2-1 for $\mathbf{p}_1$ and the ground medium is set to muscle tissue properties. To achieve a good comparability, the model is normalized to 1 dBWm^{-2} at a distance of $d_p = 0.1$ m.

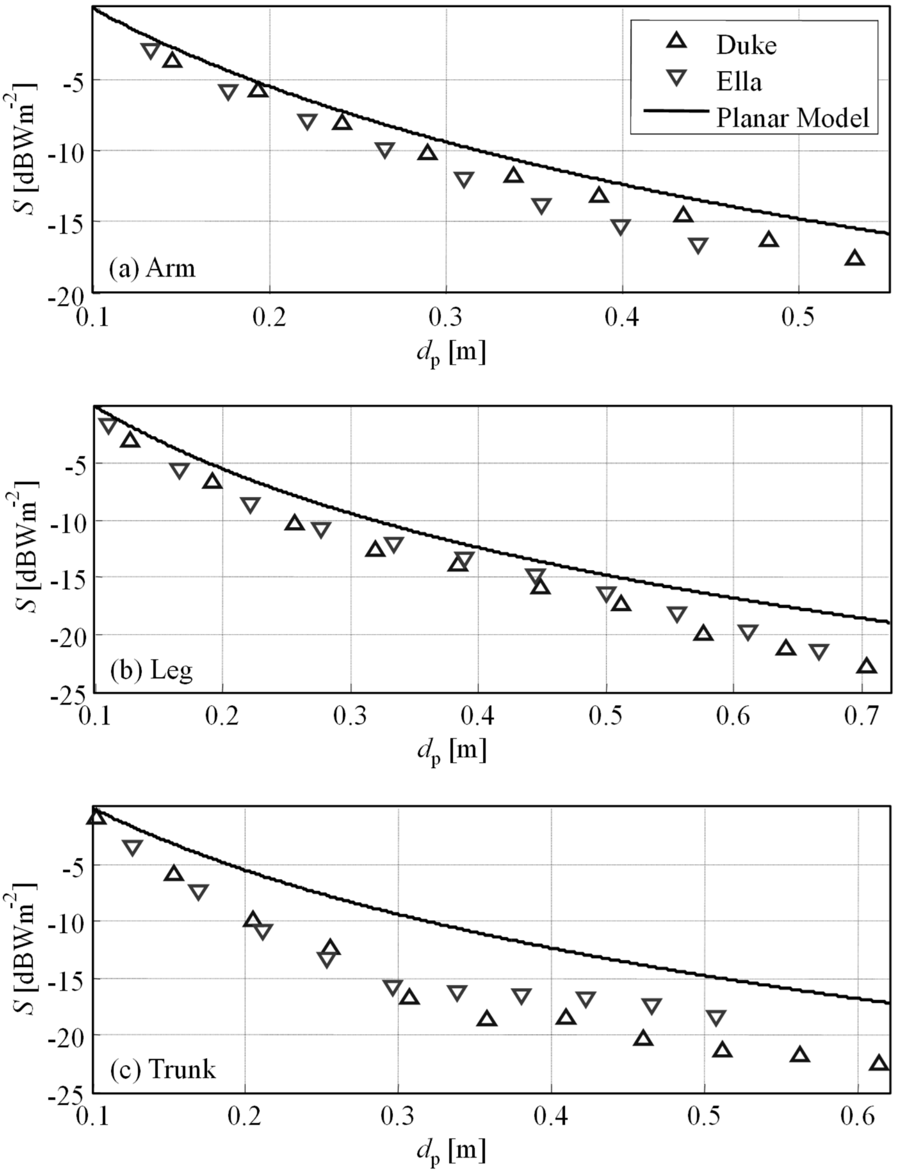

Fig. 5-3 Numerically calculated magnitude of the power flux density versus distance for different evaluation paths and voxel models in comparison to a planar muscle tissue model. Parameters: Normally orientated half-wave dipole, $f = 2.45$ GHz, $h = \lambda/4$.

As seen from Fig. 5-3, the model is capable of representing the average mean value of the paths under test, and hence implies the applicability of the suggested model. The major problem, which arises from this modeling technique, is the unknown normalization factor of the planar model. The definition of an appropriate factor in terms of a unified antenna theory is shown in the context of the next chapter.

5.2 Norton Surface Waves in Context of Body-Centric Applications

While each individual antenna concept is connected to a specific response of the line-of-sight channel, which is discussed in the following paragraph, the intention of this paragraph is to discuss general channel aspects. Descending from the basic field equations of the planar on-body model, comparing (2.70) and (2.71), the propagation of the radiated ground wave is, in general, a function of the frequency, the constitutive parameters of the ground, the effective antenna height, and the antenna polarization. The variations in these quantities are discussed to identify the general on-body far field behavior and to link general antenna configurations to desired radiation mechanisms.

5.2.1 Applicability in Terms of Human Dermis Tissues

To ensure the applicability of the planar on-body model, the Bannister theory has to be verified in terms of surface near tissue types, muscle, skin and fat. Muscle especially is a commonly used tissue type to model the average losses in body-centric propagation scenarios [Hal06]. When it comes to higher frequencies, the skin and fat layers might be more relevant. As seen in Chapter 2, descending from the connected derivation procedure, the main requirement to ensure the applicability of the field factors of Table 2-1 is to guarantee a sufficient high material difference $n = \gamma_1/\gamma_0$. As shown in [Ban84b], in practical applications, this demand is satisfied for $n^2 \geq 10$. Table 5-1 shows the corresponding tissue ratios, which are based on the multiple Cole-Cole equation (4.17) and the connected Gabriel parameters of Appendix B for the selected frequencies.

In coincidence with Table 4-1, the defined frequency range of interest reaches from 0.4 GHz to 60 GHz, and common WBAN frequencies are selected from this range. The values related to the condition $n^2 \geq 10$ imply a good applicability of the Bannister equations to muscle and skin tissues, while the fat tissue results show borderline values, especially for *f* = 60 GHz.

TABLE 5-1
APPLICABILITY OF THE BANNISTER THEORY IN TERMS OF HUMAN DERMIS TISSUES

Symbol	Unit	Value to corresponding frequency				
f	GHz	0.4	1	2.45	5.4	60
$\lvert n^2_{\text{muscle}}\rvert$	1	67	58	54	51	20
$\lvert n^2_{\text{fat}}\rvert$	1	6	5	5	5	3
$\lvert n^2_{\text{skin}}\rvert$	1	56	44	39	37	14

5.2.2 Numerical Distance of Fat, Muscle and Skin Tissue

According to [Som26] and [Nor37], the Norton surface wave is closely connected to the air-ground boundary due to the fact that a small component of the Poynting vector points toward the ground to preserve the wave. Nevertheless, this component is relatively small, and the main component of the energy flux is directed along the surface. In conjunction with the fact that for far distances the major part of the space wave is reflected away from the ground, the Norton surface wave adds a substantial contribution, especially for long-range on-body communications.

TABLE 5-2
NUMERICAL DISTANCE OF HUMAN DERMIS TISSUES

Symbol	Unit	Value to corresponding frequency				
f	GHz	0.4	1	2.45	5.4	60
$\lvert w_{\text{muscle}}\rvert$	1	0.12	0.36	0.95	2.21	61.7
$\lvert w_{\text{fat}}\rvert$	1	1.43	3.79	9.62	22.3	388
$\lvert w_{\text{skin}}\rvert$	1	0.15	0.48	1.30	3.04	93.1
φ_{muscle}	[°]	-58	-72	-76	-73	-39
φ_{fat}	[°]	-72	-80	-82	-80	-75
φ_{skin}	[°]	-57	-68	-74	-72	-36

A very important factor to estimate the capability of a strong surface wave excitation is given by the numerical distance defined by A. Sommerfeld [Som26]. As shown in (2.73) and (2.74), the Sommerfeld attenuation function F is part of the Norton surface wave component and, therefore, a large numerical distance results in a weak surface wave. As defined by (2.75), the numerical distance is a function of the constitutive parameters of the ground, the frequency and the effective antenna height. Table 5-2 shows the corresponding values of the numerical distance w at certain WBAN frequencies between 0.4 GHz and 60 GHz at an effective antenna height of $h = 0$ for typical body surface tissues. The depicted values are separated in magnitude $|w|$ und phase component φ. It can be observed from Table 5-2 that the magnitude of the numerical distance varies extremely, depending on the tissue parameters. For instance, at $f = 0.4$ GHz, the numerical distance of muscle and fat differs approximately by a factor of 12. This fact implies that tissues having low conductivity, such as low water content tissues, are less capable of supporting a dominant Norton surface wave. In order to illustrate the relationship between the tissue parameters and the frequency dependency, Fig. 5-4 shows the Sommerfeld attenuation function versus the numerical distance for muscle and fat tissue at selected frequencies.

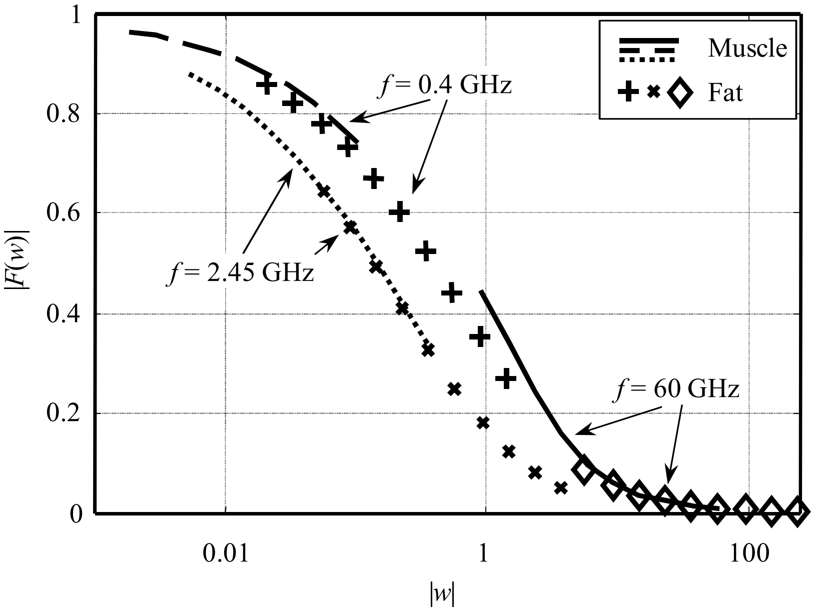

Fig. 5-4 [Gri14b]: Sommerfeld attenuation function for a ground consisting of muscle and fat tissue;

$h = 0$; $R_1 \in [0.03, 2]$ m; $f = 0.4$ GHz, 2.45 GHz and 60 GHz.

5.2.3 Ratio of the Norton Surface Wave to the Space Wave in Relation to Tissue Type and Frequency

In order to identify the dominant wave type of common on-body scenarios, the ratio of the space wave component and the Norton surface wave component is calculated. The variation of the body tissue is modeled by a ground consisting of the high water content tissue muscle and the low water content tissue fat. Because of the fact that the Bannister equations are not suitable to analyze the ratio for low water content tissues, the ratio is calculated using Norton's solution (2.73). Therefore, the results are limited to distances greater than one free space wave length. To cover even WBAN scenarios with far communication links the maximum observation distance is set to 2 m, which is more than the total body height of the "Duke" voxel model. The frequencies of interest are set to 0.4 GHz, 2.45 GHz, and 60 GHz, while the corresponding effective antenna heights are set to $\lambda_0/4$.

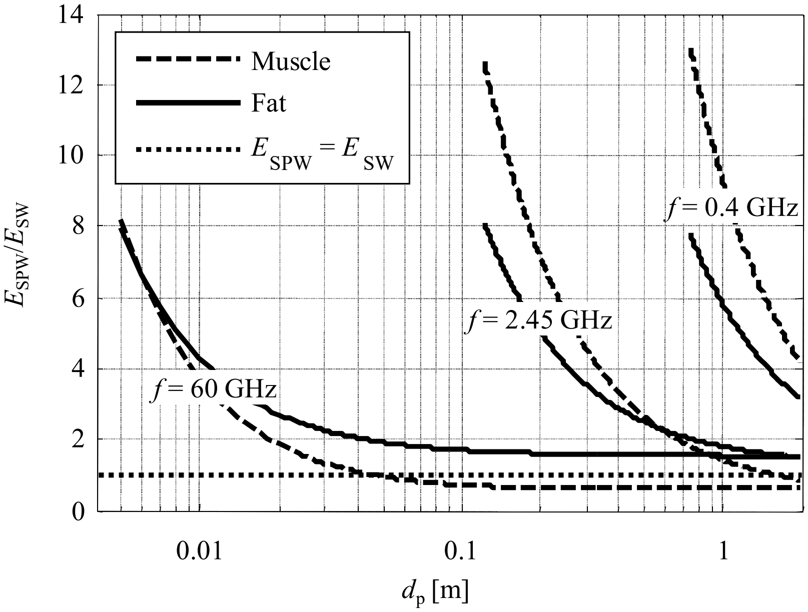

Fig. 5-5 [Gri14b]: Ratio of space wave and Norton surface wave above muscle and fat tissue for different frequencies; $h = \lambda_0/4$; $f = 0.4$ GHz, 2.45 GHz and 60 GHz

Figure 5-5 shows the ratios derived for the normally orientated dipole $\mathbf{p}_1$ and suggests some interesting practical implications: In order to cover small on-body distances, an antenna design which yields a strong space wave excitation may be desired while a communication link over large distances may benefit from a strong Norton surface wave. Especially for fat tissue, this observation takes on a greater significance due to the large numerical distances. Related to the results at $f = 0.4$ GHz, the space wave is much more dominant than the Norton surface wave for both tissue types. At frequencies around $f = 2.45$ GHz, a balanced wave combination of the total field is shown at medium ranges for muscle tissue. At $f = 60$ GHz, a strong Norton surface wave can be identified for propagation distances above 0.05 m. This implies a significant contribution of the Norton wave component for WBAN applications within this frequency range.

5.2.4 Ratio of the Norton Surface Wave to the Space Wave in Relation to the Effective Antenna Height

At the lower frequencies considered above, slight variations of the effective antenna height have a negligibly small influence on the Norton surface wave excitation. In this case, the variations are comparatively small in relation to the free space wavelength. On the contrary: at 60 GHz, even a movement by one millimeter is within the range of a quarter of a wave length—see Table 4-1—and results therefore in altered radiation properties.

As defined by (2.75), the numerical distance is connected to the effective antenna height by the angle ψ_1. In order to evaluate the influence of the effective antenna height, the Norton surface wave to space wave ratio is calculated for normal dipole orientation $\mathbf{p}_1$ at different effective antenna heights by (2.73). The corresponding frequency is set to $f = 60$ GHz and the constitutive parameters are set to a skin tissue equivalent due to the small penetration depth at this frequency (see Table 4-1). For effective heights above a quarter of one free space wavelength, the calculated values in Fig. 5-6 indicate a dominant space wave over the whole observation range. Moreover, the results imply a dominant Norton surface wave excitation only for antennas, which are closely bound to the body surface. For instance, in the scope of 60 GHz textile antennas, the results imply a sensitive relationship between the height and the related wave form.

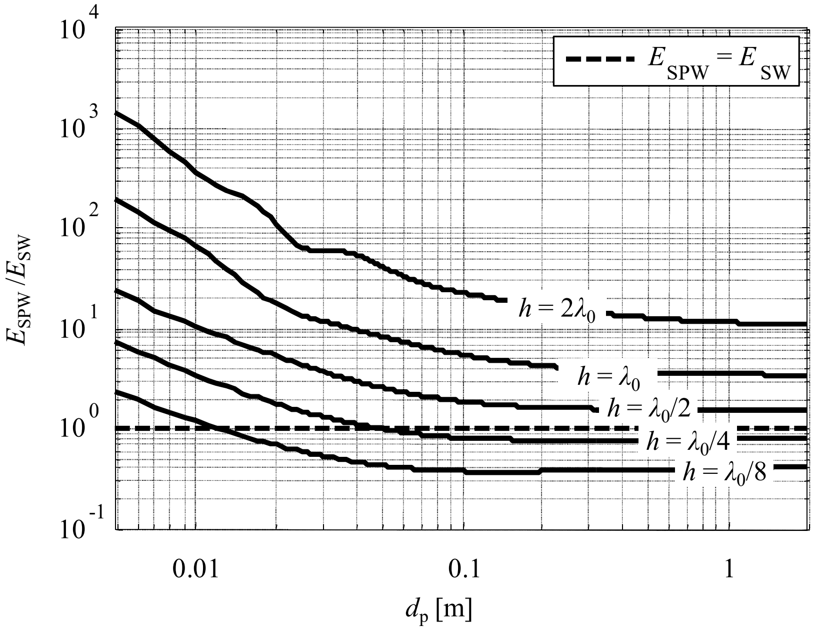

Fig. 5-6 [Gri14b]: Ratio of space wave and surface wave above skin tissue ground for different effective antenna heights h; $f = 60$ GHz.

5.3 Radiated Antenna Field of Body-Worn Antennas

In conjunction with the approach of Bannister in [Ban84a] and [Ban84b], the basic antenna setup assumes a small electric dipole with constant current distribution, which is positioned on or above the surface at the effective antenna height h. Related to the validity discussion above, this solution is applicable for a wide range of high water content tissues, where we primarily use in the following an equivalent human muscle tissue medium. In conjunction with Chapter 2, the propagation constant of free space is denoted by γ_0, the propagation constant of the body tissue is γ_1, and the free space impedance is defined by η_0. In general, we assume RMS values where a time-harmonic dependency is assumed and the corresponding factor $\exp(j\omega t)$ is omitted. The general schematic of on-body antenna setup is shown in Fig. 5-7.

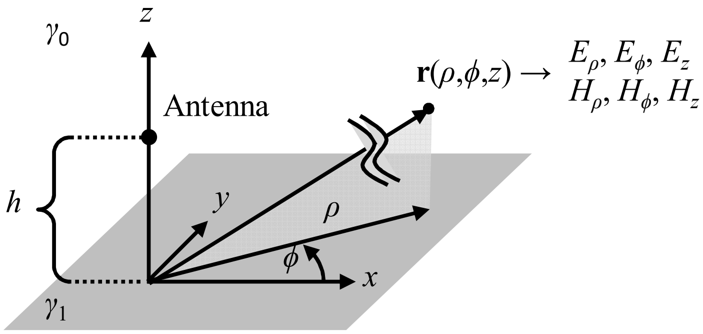

Fig. 5-7 [Gri15b]: General on-body setup consisting of an antenna at effective height h above a dissipative dielectric body.

The key results presented in the remaining chapter are a combination of [Gri14b] and [Gri15b]. Therefore, the content is revised and rearranged at some points to feature an adequate recapitulation of the whole theory in closed form.

5.3.1 Electric Dipole Antennas

Related to the discussed solution of Sommerfeld geometry by the Hertz potential, the resulting equations deliver a straightforward description of small electric dipole antennas. Based on the defined basic dipole orientations of Fig. 2-3, the radiated electric field components of all three configurations are discussed. Figure 5-8 shows the electric field components of the normally $\mathbf{p}_1$-orientated half-wave dipole ($f = 2.45$ GHz) located above a muscle tissue ground along an observation path parallel to the surface at the effective antenna height $h = \lambda_0/4$. The corresponding observation path proceeds in x-direction and is unchanged for all three basic examples. The values obtained by the Bannister model using (2.70) are compared to a numerical simulation based on the FDTD method [EMP]. In order to evaluate the accuracy of the model with reference to the numerical data, the Bannister description of the electric field has been normalized to the FDTD field values at maximum distance.

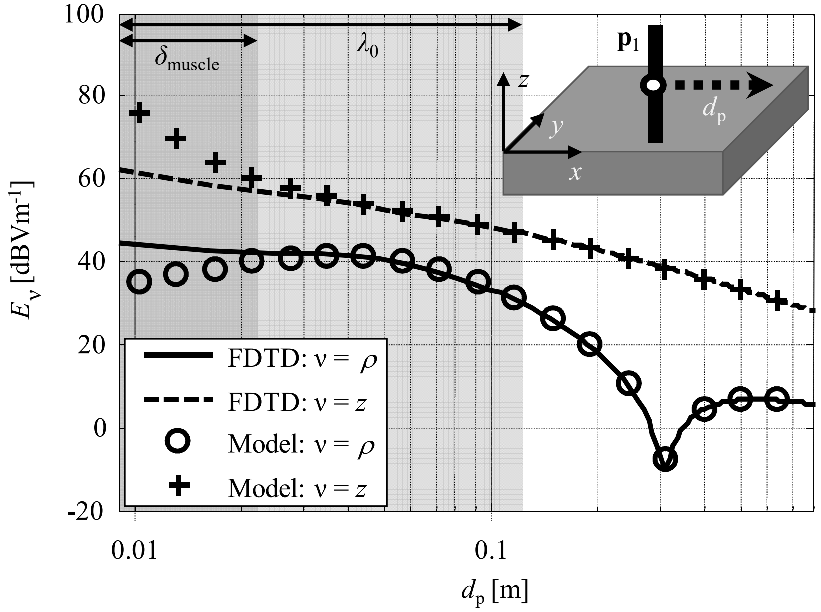

Fig. 5-8 [Gri14b]: Electric field components of a normal half-wave dipole above muscle tissue ground; $f = 2.45$ GHz; $h = \lambda_0/4$; Dipole axis: $\mathbf{p}_1$

It can be observed from Fig. 5-8 that the Bannister model approximates the field very well, even quite close to the dipole. In contrast to the normally orientated dipole, the electric field generated by a tangential dipole above the tissue does not exhibit a radial symmetry. In this case, according to [Akh10], the related radiation mechanism suggests a discussion of two orthogonal horizontal dipole orientations. In our case, we use the remaining two defined dipole orientations $\mathbf{p}_2$ and $\mathbf{p}_3$.

As shown in Fig. 5-9, the first case corresponds to the horizontal dipole, as discussed by Norton in [Nor37]. The axis of the dipole is orientated tangential transversal to the path direction in y-direction and is also positioned above a muscle tissue ground at the effective height $h = \lambda_0/4$. The results of the second tangential case are shown in Fig. 5-9. Here, the axis of the half-wave dipole is orientated in x-direction at $h = \lambda_0/4$ and is, therefore, aligned transversal longitudinal to the observation path. The electric field values of both scenarios are calculated by the normalized Bannister solution (2.70) and verified numerically using the FDTD method [EMP].

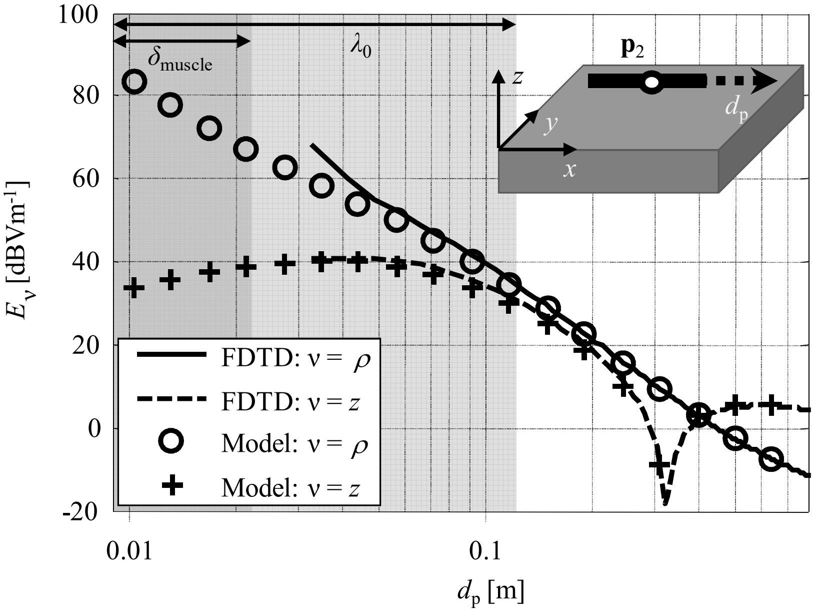

Fig. 5-9 [Gri14b]: Electric field components of a tangential longitudinal orientated half-wave dipole above muscle tissue ground; $f = 2.45$ GHz; $h = \lambda_0/4$; Dipole axis: $\mathbf{p}_2$

If, in addition, the magnetic field values are obtained by (2.71), the tangential transversal dipole $\mathbf{p}_3$ shows a TE characteristic, while the tangential longitudinal dipole $\mathbf{p}_2$ shows a TM characteristic. According to [Akh10], this behavior implies that the excited field specie can be changed either by a rotation of the tangential dipole axis or by a definition of another path direction. In comparison, the normal dipole $\mathbf{p}_1$ shows an omnidirectional TM characteristic. If both TM characteristics are compared, i.e. $\mathbf{p}_1$ and $\mathbf{p}_2$, the TM wave resulting from the tangential dipole is quite weak due to the diminishing direct wave component, since in this orientation the field is primarily excited by the images of the dipole within the ground.

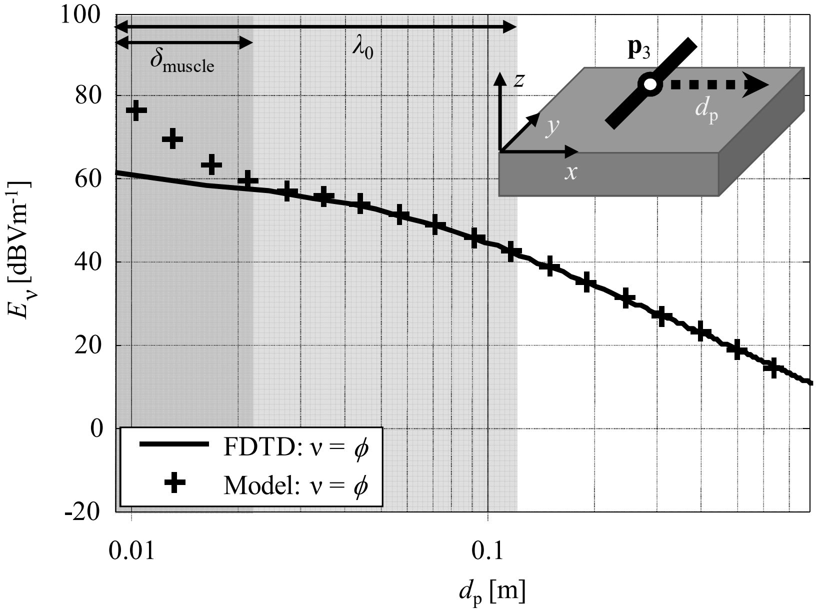

Fig. 5-10 [Gri14b]: Electric field components of a tangential transversal orientated half-wave dipole above muscle tissue ground; $f = 2.45$ GHz; $h = \lambda_0/4$; Dipole axis: $\mathbf{p}_3$

The results indicate that the Bannister solution is capable of modeling the quasi-static range with good accuracy, even for realistic antenna configurations. In terms of the Norton theory, this means that even critical distances below one wavelength can be treated by this model. Despite the fact that Bannister restricts his solution of (2.70) and (2.71) to distances larger than 10 penetration depths of the ground [Ban78], the derived values indicate a sufficient applicability even for smaller distances that are above one penetration depth.

5.3.2 Arbitrarily Shaped Antennas

Strictly speaking, the Norton surface wave theory is defined only for small dipole antennas. To model larger and more complex antennas, our approach is to discretize the large antenna structure down into a finite number of small electric dipoles. Owing to the cubic mesh grid of the FDTD method, it seems evident to break down the electric current flow density on a numerically calculated antenna structure into a cluster of small electric dipoles.

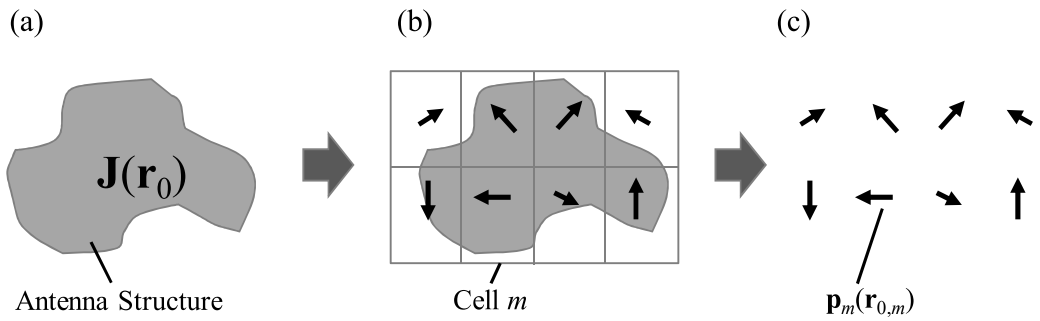

Fig. 5-11 [Gri15b]: (a) General antenna structure with corresponding current density; (b) Segmentation of the antenna structure into M cells; (c) Group of M equivalent electric dipole sources.

Hereto, as shown in Fig. 5-11, the antenna structure is divided into M space cells. Assuming a perfectly conducting antenna, the total radiated field can then be expressed by the superposition of the field formulation of M small electric dipoles at position $\mathbf{r}_{0,m}$ with $m \in \{1,2,...,M\}$. Related to the arbitrary antenna shape each dipole element can be arbitrarily orientated itself: see Fig. 5-12. The dipole momentum $\mathbf{p}_m$ of cell m can be separated into three orthogonal dipoles $\mathbf{p}_{1,m}$, $\mathbf{p}_{2,m}$, and $\mathbf{p}_{3,m}$ which correspond to the chosen coordinate system. By the assumption of Cartesian coordinates, the decomposition yields

$$\mathbf{p}_m = p_{2,m}\mathbf{e}_x + p_{3,m}\mathbf{e}_y + p_{1,m}\mathbf{e}_z\,, \tag{5.1}$$

where Fig. 5-12 depicts the orthogonal dipole components in relation to the origin.

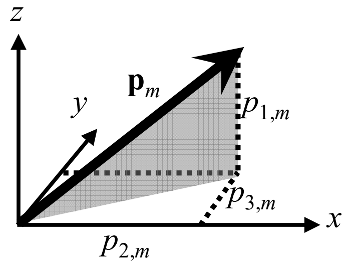

Fig. 5-12 [Gri15b]: Separation of the dipole momentum p_m into three Cartesian components p_1, p_2, and p_3.

In the following context, the FDTD method [EMP] is used to calculate the current density distribution $\mathbf{J}(r_0)$ on the antenna structure. The related dipole moment $\mathbf{p}_m$ of (5.1) then results from a multiplication of this value with the spatial cell dimensions.

The radiated field of each dipole results from the superposition of the three canonical dipoles within the underlying cell—namely, $\mathbf{p}_{1,m}$, $\mathbf{p}_{2,m}$, and $\mathbf{p}_{3,m}$. These definitions are coincident with our basic dipoles, as defined in Fig. 2-3. Based on direct transformation from cylindrical to Cartesian coordinates, the superimposed electric antenna field can be expressed by (2.70) with

$$\mathbf{E}_1 = \frac{p_1 \eta_0 \gamma_0}{4\pi\rho} \left(N_{1,x}^{\mathrm{E}} \mathbf{e}_x + N_{1,\mathrm{y}}^{\mathrm{E}} \mathbf{e}_y + N_{1,\mathrm{z}}^{\mathrm{E}} \mathbf{e}_z \right), \tag{5.2}$$

$$\mathbf{E}_2 = \frac{p_2 \eta_0 \gamma_0}{4\pi\rho} \left(\cos(\phi) N_{2,\mathrm{x}}^{\mathrm{E}} \mathbf{e}_x + \sin(\phi) N_{2,\mathrm{y}}^{\mathrm{E}} \mathbf{e}_y + \cos(\phi) N_{2,\mathrm{z}}^{\mathrm{E}} \mathbf{e}_z \right), \tag{5.3}$$

$$\mathbf{E}_3 = \frac{p_3 \eta_0 \gamma_0}{4\pi\rho} \left(\sin(\phi) N_{2,\mathrm{x}}^{\mathrm{E}} \mathbf{e}_x - \cos(\phi) N_{2,\mathrm{y}}^{\mathrm{E}} \mathbf{e}_y + \sin(\phi) N_{2,\mathrm{z}}^{\mathrm{E}} \mathbf{e}_z \right), \tag{5.4}$$

where N_1^{E}, resp. N_2^{E}, corresponds to the electric field factor functions of Table 2-1 with unit [1]. In an equivalent manner, we can find the magnetic field comments using (2.71) with

$$\mathbf{H}_1 = \frac{p_1 \gamma_0}{4\pi} \left(N_{1,x}^{\mathrm{H}} \mathbf{e}_x + N_{1,y}^{\mathrm{H}} \mathbf{e}_y + N_{1,z}^{\mathrm{H}} \mathbf{e}_z \right), \tag{5.5}$$

$$\mathbf{H}_2 = \frac{p_2 \gamma_0}{4\pi} \left(\sin(\phi) N_{2,x}^{\mathrm{H}} \mathbf{e}_x + \cos(\phi) N_{2,y}^{\mathrm{H}} \mathbf{e}_y + \sin(\phi) N_{2,z}^{\mathrm{H}} \mathbf{e}_z \right), \tag{5.6}$$

$$\mathbf{H}_3 = \frac{p_3 \gamma_0}{4\pi} \left(-\cos(\phi) N_{2,x}^{\mathrm{H}} \mathbf{e}_x + \sin(\phi) N_{2,y}^{\mathrm{H}} \mathbf{e}_y - \cos(\phi) N_{2,z}^{\mathrm{H}} \mathbf{e}_z \right), \tag{5.7}$$

where N_1^{H}, resp. N_2^{H}, corresponds to the electric field factor functions of Table 2-1 with unit [1].

In the final step, the radiated electromagnetic field of the complete antenna structure follows from the superposition of the corresponding M cells. Therefore, the summation of the related field components of the basic dipoles defined by (5.2), (5.3), and (5.4) at position $\mathbf{r}_{0,m}$ is

$$\mathbf{E}^{\mathrm{total}}(\mathbf{r}) = \sum_{m=1}^{M} \sum_{\nu=1}^{3} \mathbf{E}_\nu (\mathbf{r} - \mathbf{r}_{0,m}). \tag{5.8}$$

In an equivalent manner, the total magnetic field can be calculated using (5.5), (5.6), and

(5.7) by

$$\mathbf{H}^{\text{total}}(\mathbf{r}) = \sum_{m=1}^{M} \sum_{\nu=1}^{3} \mathbf{H}_{\nu}(\mathbf{r} - \mathbf{r}_{0,m}) . \tag{5.9}$$

With respect to the desired properties of the field formulation, the corresponding terms (5.2)–(5.7) may also be chosen from Norton's solution. Here, we have chosen Bannister's air-to-air formulation that is applicable from quasi-static ranges to far field distances. Owing to the fact that for far field distances, the underlying formulations of Bannister converge into the formulation of Norton, the method used may also be based on Norton's electric dipole model [Nor37] if far field distances are only of interest. In this case, the tangential dipole, as defined by Norton, is rotated through 90° compared to the Bannister definition, i.e. in this case, the field description of $\mathbf{p}_2$ and $\mathbf{p}_3$ have to be exchanged by each other.

Considering (5.1)–(5.9), the knowledge of the excited currents on the antenna body enables a description of the radiated electromagnetic on-body field. Throughout the paper, we are using the full wave simulation software [EMP], which is based on the FDTD method, to calculate the current distribution on the antenna structure. The simulations are done for antennas in the presence of a body phantom, i.e. the antennas are positioned near an anatomically correct human body voxel model or near a tissue equivalent surface, to include the coupling between body and antenna. The numerical model includes the antenna structure and the ground where the computational domain is terminated by open boundary conditions at a distance of two wave lengths from the antenna center. The general setup is shown in Fig. 5-13.

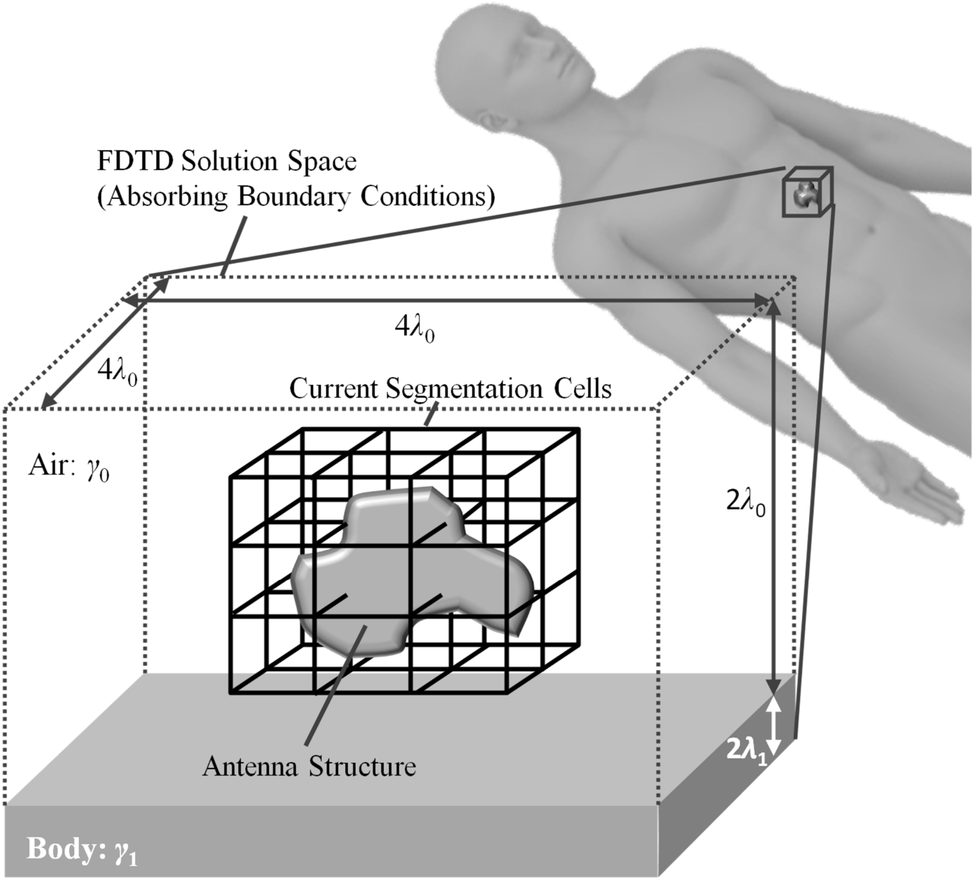
FDTD Solution Space
(Absorbing Boundary Conditions)
$4\lambda_0$
$4\lambda_0$
Current Segmentation Cells
Air: γ_0
$2\lambda_0$
Antenna Structure
$2\lambda_1$
Body: γ_1

Fig. 5-13 [Gri15b]: General setup to model the radiated on-body field by the FDTD method. As depicted, the current distribution on the antenna structure is segmented into a finite number of space cells. Each segment represents a small dipole element for the application of the Bannister model.

To ensure a clear differentiation between the current distribution that is wanted on the antenna structure and the induced currents within the phantom, our method benefits from a spacing between antenna and phantom. Consequently, this approach loses sharpness if the antenna structure is positioned in direct contact with the phantom. Apart from this, the generality of our approach enables the modeling of various antenna types as long as these can be approximated by a finite number of small electric dipoles and is not restricted to the validation examples below.

5.4 On-Body Antenna Parameters

The approach presented above enables insight into the underlying radiated electromagnetic field of body-worn antennas. Nevertheless, a comparison of the related radiation characteristic with the electromagnetic field distribution is difficult to realize. The following section will discuss an approach to define concentrated on-body antenna parameters. The primary focus aims at a possible definition of the equivalent on-body directivity and the on-body effective antenna area.

5.4.1 Far Field Distance

Depending on the selected far field model, the applicability of the underlying formulation is restricted to distances which are above a certain limit. As seen in Chapter 2, this distance is related to the chosen approach to calculate the Hertz vector and is a function of the frequency and the dielectric material parameters of the body. In case of the Norton formulation, as described in [Ban84a], a distance can be identified as part of the far field if the following equation is satisfied:

$$\left| \gamma_0 \left(\rho^2 + (z+h)^2 \right)^{\frac{1}{2}} \right| >> 1 . \tag{5.10}$$

Norton's formulation is, therefore, valid for distances above a few free space wave lengths and defines the far field in general terms of on-body communications. However, this distance may be not practical for many of the short on-body paths present in some on-body communication links. Here, the quasi-static range of Bannister's solution enables a quite accurate modeling starting from distances of a few penetration depths of the ground [Gri14b].

5.4.2 Far Field Components

As seen above, for on-body propagation paths, e.g. the observation path **r** proceeds parallel to the body surface in x direction, the basic dipoles $\mathbf{p}_1$ and $\mathbf{p}_2$ have a TM far field characteristic, and the dipole $\mathbf{p}_3$ has a TE characteristic. Related to (5.2)–(5.7), an antenna of arbitrary shape has a characteristic that is a superposition of the corresponding sources and their associated field values. For valid distances, it follows from (5.8) and

(5.9) that the power flux density **S** can be calculated by the Poynting vector from the superimposed field values by

$$\mathbf{S}=\mathbf{E}\times\mathbf{H}^{*}=\left(\mathbf{E}_1+\mathbf{E}_2+\mathbf{E}_3\right)\times\left(\mathbf{H}_1+\mathbf{H}_2+\mathbf{H}_3\right)^{*}. \tag{5.11}$$

In general, the field values (5.11) can then be separated into their TM and TE components as follows:

$$\mathbf{S}=\left(\underbrace{\begin{bmatrix}E_{1,\rho}+E_{2,\rho}\\0\\E_{1,z}+E_{2,z}\end{bmatrix}}_{\mathbf{E}_{\mathrm{TM}}}+\underbrace{\begin{bmatrix}0\\E_{3,\phi}\\0\end{bmatrix}}_{\mathbf{E}_{\mathrm{TE}}}\right)\times\left(\underbrace{\begin{bmatrix}0\\H_{1,\phi}+H_{2,\phi}\\0\end{bmatrix}}_{\mathbf{H}_{\mathrm{TM}}}+\underbrace{\begin{bmatrix}H_{3,\rho}\\0\\H_{3,z}\end{bmatrix}}_{\mathbf{H}_{\mathrm{TE}}}\right)^{*}. \tag{5.12}$$

Equation (5.12) can also be written as

$$\mathbf{S}=\begin{bmatrix}E_{1,\rho}+E_{2,\rho}\\0\\E_{1,z}+E_{2,z}\end{bmatrix}\times\begin{bmatrix}0\\H_{1,\phi}^{*}+H_{2,\phi}^{*}\\0\end{bmatrix}+\begin{bmatrix}0\\E_{3,\phi}\\0\end{bmatrix}\times\begin{bmatrix}H_{3,\rho}^{*}\\0\\H_{3,z}^{*}\end{bmatrix}. \tag{5.13}$$

or expressed in matrix notation

$$\mathbf{S}=\underbrace{\left(\mathbf{E}_1+\mathbf{E}_2\right)\times\left(\mathbf{H}_1+\mathbf{H}_2\right)^{*}}_{\mathbf{S}_{\mathrm{TM}}}+\underbrace{\left(\mathbf{E}_3\times\mathbf{H}_3^{*}\right)}_{\mathbf{S}_{\mathrm{TE}}}. \tag{5.14}$$

Equation (5.14) shows that the total far field power flux density can be expressed by the summation of the TE and TM power flux densities.

5.4.3 Equivalent Electric Sources Approach

Equation (5.12) implies that the far field of an arbitrary on-body antenna can be decomposed into its corresponding TM and TE wave components. Furthermore, we take (5.14) into account that we can model the total power flux density of the original source by two equivalent sources, a TM source and TE one. The TE source can be modeled by a small dipole $\mathbf{p}_{\mathrm{TE}}$ that is aligned tangentially to the body surface and perpendicular to the observation direction. The TM source $\mathbf{p}_{\mathrm{TM}}$ can either be represented by a tangential dipole, the axis of which is aligned in observation direction, or by a normally oriented dipole. In this manner, we have chosen the normally oriented dipole as the equivalent source, and the corresponding setup is shown in Fig. 5-14. This source is selected because the related far field of a tangential dipole source, which is aligned in the direction of propagation, is negligibly small in comparison to the source components of the other two directions. As a comparison of Fig. 5.8 and Fig. 5.9 reveals, this can lead back to the significantly weaker radiated power in direction of the dipole axis.

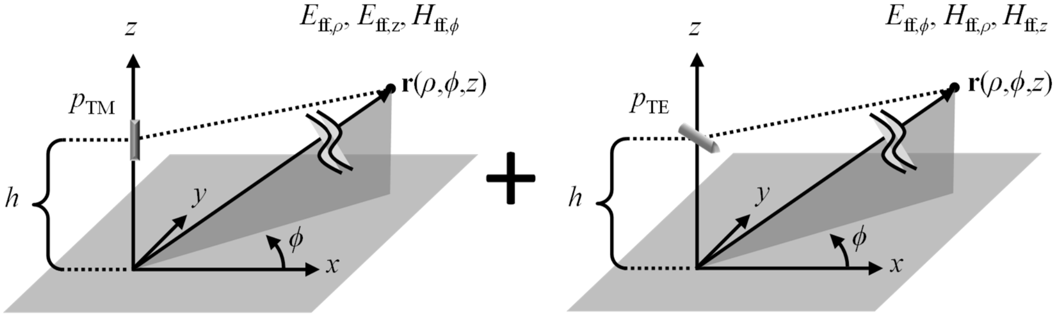
z
$E_{\mathrm{ff},\rho}, E_{\mathrm{ff},z}, H_{\mathrm{ff},\phi}$
p_{TM}
$\mathbf{r}(\rho,\phi,z)$
h
y
ϕ
x
+
z
$E_{\mathrm{ff},\phi}, H_{\mathrm{ff},\rho}, H_{\mathrm{ff},z}$
p_{TE}
$\mathbf{r}(\rho,\phi,z)$
h
y
ϕ
x

Fig. 5-14 [Gri15b]: Normally oriented p_{TM} and tangentially oriented p_{TE} equivalent electric dipoles to model the TM and TE far field.

In order to verify this assumption in terms of body-worn antennas, $\mathbf{S}_{\mathrm{TM}}$ is independently calculated for both TM sources. If we assume the far field of a low-profile antenna, i.e. the effective antenna height is almost zero, or alternatively let the distance converge to infinity, the space wave will vanish. The resulting field then consists only of the Norton surface wave component. If we now calculate the general solution of (5.14)

$$\mathbf{S}_{\mathrm{TM}} = -E_z H_\phi^* \mathbf{e}_\rho + E_\rho H_\phi^* \mathbf{e}_z \tag{5.15}$$

and follow the air-to-air far field formulation in [Ban84a], keeping the assumptions given above in mind, the direct and reflected path distances converge into the distance ρ and the reflection coefficient of the ground (2.46) becomes minus one. With these assumptions, the power flux density $\mathbf{S}_{\mathrm{TM},1}$ of the normal electric dipole $\mathbf{p}_{\mathrm{norm}}$ is

$$\mathbf{S}_{\mathrm{TM},1} = \frac{\gamma_0^2 \eta_0 \left| p_{\mathrm{norm}} \right|^2}{4\pi^2 \rho^2} \left| F(w) \right|^2 e^{-2\gamma_0 \rho} \left[\mathbf{e}_\rho - \Delta \mathbf{e}_z \right] \tag{5.16}$$

and $\mathbf{S}_{\mathrm{TM},2}$ of the tangential electric dipole $\mathbf{p}_{\mathrm{tang,long}}$, which is aligned along the observation direction, is

$$\mathbf{S}_{\mathrm{TM},2} = \frac{\gamma_0^2 \eta_0 \left|p_{\mathrm{tang,long}}\right|^2}{4\pi^2 \rho^2} \left|\Delta\right|^2 \left|F(w)\right|^2 e^{-2\gamma_0 \rho} \left[\mathbf{e}_\rho - \Delta \mathbf{e}_z\right]. \tag{5.17}$$

In (5.16) and (5.17), $F(w)$ denotes the Sommerfeld surface wave attenuation factor which is defined by

$$F(w) = \left[1 - j\sqrt{\pi w} e^{-w} \operatorname{erfc}\left(-j\sqrt{w}\right)\right], \tag{5.18}$$

where w denotes the numerical distance, which is in this case

$$w \approx -\frac{\gamma_0 \rho}{2} \sin \Delta^2. \tag{5.19}$$

In (5.16), (5.17), and (5.19), Δ defines the ratio of the two propagation constants of the media, i.e. free space and body tissue, which is defined by

$$\Delta = \frac{\gamma_0}{\gamma_1}. \tag{5.20}$$

A comparison of (5.16) and (5.17) reveals that the radiated power flux density of the tangential dipole differs from the corresponding normally oriented dipole by the factor $|\Delta|^2$ if we assume the same magnitude of dipole momentums, i.e. $p_{\mathrm{norm}} = p_{\mathrm{tang,long}}$. This implies that we can model the general TM far field, which may result from both sources, by a single equivalent TM source.

To evaluate how sufficient this assumption is, we calculate the deviation between the power flux density of $\mathbf{p}_{\mathrm{norm}}$ and $\mathbf{p}_{\mathrm{tang,lomg}}$ by the use of the complete Bannister equations (2.70) and (2.71). To achieve a matching of both values for infinite distance, $S_{\mathrm{norm},\rho}$ is corrected by the factor $|\Delta|^2$. By a normalization to $|S_{\mathrm{tang,long},\rho}|$ the deviation is

$$d_{\mathrm{f}} = \frac{\left|S_{\mathrm{norm},\rho} \,|\, \Delta \,|^2 - S_{\mathrm{tang,long},\rho}\right|}{\left|S_{\mathrm{tang,long},\rho}\right|}. \tag{5.21}$$

In this respect, Fig. 5-15 shows the deviation at 2.45 GHz for muscle tissue as a function of the effective antenna height and the distance. Both values are normalized to the free space wave length. As seen from the results, the error is negligible for low effective heights at moderate distances and, therefore, proves a good applicability in terms of low profile on-body antennas. Moreover, the calculated error, which may arise by a description of $\mathbf{p}_{\text{tang,long}}$ through $\mathbf{p}_{\text{norm}}$, becomes significant if the antenna shows a dominant tangential current distribution pointing in the direction of the observation. In all other cases, i.e. considering antennas with mixed distributions, the contribution of $\mathbf{p}_{\text{tang,long}}$ is dominated by the normal current $\mathbf{p}_{\text{norm}}$ due to the factor $|\Delta|^2$ in (5.17).

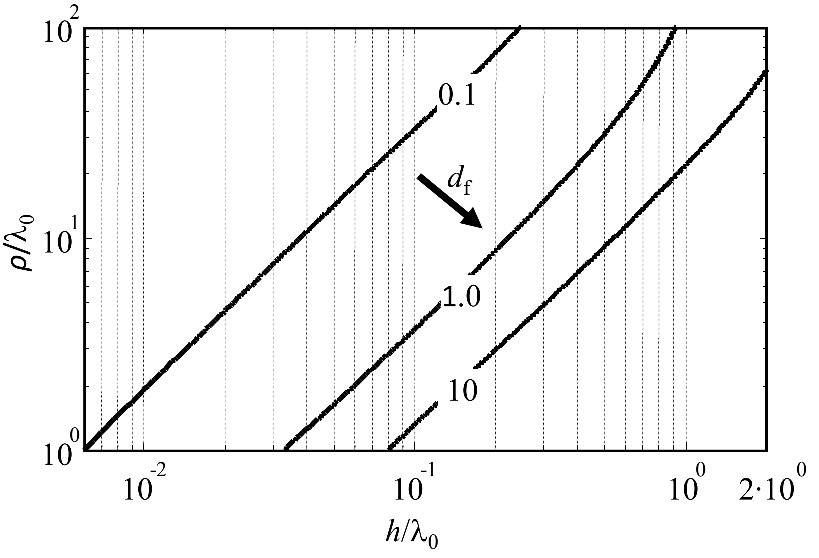

Fig. 5-15 [Gri15b]: Approximation of the error that can occur by using a normally oriented dipole source to express a tangential dipole which is aligned along the observation direction to describe the TM on-body field; the underlying muscle tissue parameters are based on Table 4-1.

5.4.4 On-Body Directivity

Based on the results of the previous paragraph, which state that two equivalent electric sources may sufficiently describe the on-body antenna far field, a definition of related directivity parameters seems evident. In general, the total radiated field of an antenna can be separated in the same way as described by (5.13) in the underlying TM and TE field components by

$$\mathbf{S}=\left(\underbrace{\begin{bmatrix}E_\rho\\0\\E_\mathrm{z}\end{bmatrix}}_{\mathbf{E}_\mathrm{TM}}+\underbrace{\begin{bmatrix}0\\E_\phi\\0\end{bmatrix}}_{\mathbf{E}_\mathrm{TE}}\right)\times\left(\underbrace{\begin{bmatrix}0\\H_\phi\\0\end{bmatrix}}_{\mathbf{H}_\mathrm{TM}}+\underbrace{\begin{bmatrix}H_\rho\\0\\H_\mathrm{z}\end{bmatrix}}_{\mathbf{H}_\mathrm{TE}}\right)^{*} \tag{5.22}$$

The solution of (5.22) is then given by

$$\mathbf{S}=\underbrace{\begin{bmatrix}-E_\mathrm{z}H_\phi^{*}\\0\\E_\rho H_\phi^{*}\end{bmatrix}}_{\mathbf{S}_\mathrm{TM}}+\underbrace{\begin{bmatrix}E_\phi H_\mathrm{z}^{*}\\0\\-E_\phi H_\rho^{*}\end{bmatrix}}_{\mathbf{S}_\mathrm{TE}} \tag{5.23}$$

which implies that we need two quantities to describe the total power flux density **S**, i.e. $\mathbf{S}_\mathrm{TM}$ and $\mathbf{S}_\mathrm{TE}$.

In contrast to the free space case, the power flow is directed into two directions. Consequently, two quantities are required to describe each power flux density component. However, a comparison of (5.16) and (5.17) reveals that the ratio between the ρ- and z-components is constant for far distances. Therefore, one value per equivalent source is sufficient to describe the radiation properties of the antenna in terms of the TM and TE wave species. Our definition links the excited TM field to an equivalent dipole with normal orientation, where the TE component is associated with a tangential dipole whose axis is perpendicularly orientated to the observation direction. Because the power flow in ρ direction is significantly larger—by the factor Δ—we use this component to define the directivity. According to (5.23), we can define the TM directivity D_TM as the ratio of the TM power flux densities at far field distances by

$$D_\mathrm{TM}=\frac{\mathrm{Re}\left\{S_{\mathrm{TM},\rho}\right\}}{\mathrm{Re}\left\{S_{\mathrm{TM},\rho}^{\mathrm{ff}}\right\}}=\frac{\mathrm{Re}\left\{-E_\mathrm{z}H_\phi^{*}\right\}}{\mathrm{Re}\left\{S_{\mathrm{TM},\rho}^{\mathrm{ff}}\right\}} \tag{5.24}$$

where $\mathbf{S}^\mathrm{ff}_\mathrm{TM}$ denotes the power flux density of the normal equivalent electric dipole source $\mathbf{p}_\mathrm{TM}$ with same effective height and radiated power P_rad.

In the same way, the TE directivity D_TE is defined using the ratio of the TE power flux densities by

$$D_{\mathrm{TE}} = \frac{\mathrm{Re}\left\{S_{\mathrm{TE},\rho}\right\}}{\mathrm{Re}\left\{S^{\mathrm{ff}}_{\mathrm{TE},\rho}\right\}} = \frac{\mathrm{Re}\left\{E_{\phi}H^{*}_{\mathrm{z}}\right\}}{\mathrm{Re}\left\{S^{\mathrm{ff}}_{\mathrm{TE},\rho}\right\}} \tag{5.25}$$

where $\mathbf{S}^{\mathrm{ff}}_{\mathrm{TE}}$ denotes the power flux density of the equivalent tangential perpendicular electric dipole $\mathbf{p}_{\mathrm{TE}}$. In this context, the equivalent power flux density is calculated by the Poynting vector of the equivalent electromagnetic field values. Analogous to (5.2) and (5.4), the equivalent electric far field can be expressed in terms of the defined dipole orientations by

$$\mathbf{E}^{\mathrm{ff}}_{\mathrm{TM}} = \sqrt{\frac{\eta_0\,\mathrm{P}_{\mathrm{rad}}}{4\pi}}\left(N^{\mathrm{E}}_{1,\rho}\mathbf{e}_{\rho} + N^{\mathrm{E}}_{1,\phi}\mathbf{e}_{\phi} + N^{\mathrm{E}}_{1,\mathrm{z}}\mathbf{e}_{z}\right) \tag{5.26}$$

and

$$\mathbf{E}^{\mathrm{ff}}_{\mathrm{TE}} = \sqrt{\frac{\eta_0\,\mathrm{P}_{\mathrm{rad}}}{4\pi}}\left(\sin(\phi)N^{\mathrm{E}}_{2,\rho}\mathbf{e}_{\rho} - \cos(\phi)N^{\mathrm{E}}_{2,\phi}\mathbf{e}_{\phi} + \sin(\phi)N^{\mathrm{E}}_{2,z}\mathbf{e}_{z}\right) \tag{5.27}$$

where the magnitude of the equivalent dipole momentum is represented by

$$\left|p_{\mathrm{iso}}\right|^2 = \frac{4\pi P_{\mathrm{rad}}}{\eta_0\gamma_0^2}. \tag{5.28}$$

Using (5.5) and (5.7), the equivalent magnetic far field follows from the same assumption.

Considering the results given above, the following steps are required to derive the on-body directivity: At first, the currents on the antenna body are calculated in the presence of the human body by a full-wave approach. Then, the related far field is modeled for all on-body directions as a function of the observation angle ϕ. To calculate the directivity $D_{\mathrm{TM}}(\phi)$ and $D_{\mathrm{TE}}(\phi)$, the corresponding field is separated into TM and TE components. Finally, each value is normalized to the far field model of the equivalent dipoles $\mathbf{p}_{\mathrm{TM}}$ and $\mathbf{p}_{\mathrm{TE}}$ of Fig. 5-14 for each observation angle. Equation (5.28) is used to calculate the magnitude of the equivalent dipole momentums, where the radiated power P_{rad} of the antenna is known from the initially used full-wave method.

At this point, the defined directivity values enable a direct evaluation of the antenna performance in terms of on-body propagations. Here, D_{TM} and D_{TE} define a direct measure to compare the antenna under test in terms of the wave species of a normal, resp. tangential perpendicular, Hertzian dipole. If we e.g. find an antenna with high D_{TM} value, the antenna excites a far field containing a strong Norton surface wave component which tends to follow the curvature of the human body. In reverse, if the antenna exhibits a high D_{TE} value, the corresponding space wave component tends to be reflected away from the body, which may be advantageous in terms of off-body communications.

5.4.5 On-Body Effective Antenna Area

As seen from (5.16) and (5.17), the z component primarily maintains the Norton surface wave, while the major power flow in the far field is directed parallel to the body surface in ρ direction. Therefore, the received power P_{RX}, which is available at a receiving antenna, is proportional to the power flux density S_ρ. Neglecting the power flux density in z-direction, a definition of the effective TM and TE on-body antenna area seems evident by the canonical definition in [Bal05] for plane waves. The on-body effective antenna area can then be defined by the ratio of the received power to the power flux density as well as by the directivity, as defined above for the TM component by

$$A_{\mathrm{eff,TM}} = \frac{P_{\mathrm{RX,TM}}}{\mathrm{Re}\left\{S_{\mathrm{TM},\rho}\right\}} = -\frac{\pi}{\gamma_0^2} D_{\mathrm{TM}} \tag{5.29}$$

and for the TE component by

$$A_{\mathrm{eff,TE}} = \frac{P_{\mathrm{RX,TE}}}{\mathrm{Re}\left\{S_{\mathrm{TE},\rho}\right\}} = -\frac{\pi}{\gamma_0^2} D_{\mathrm{TE}}\,. \tag{5.30}$$

The total available power P_{RX} at a receiving antenna is then given by the summation of the power delivered by the TM and TE field components, namely

$$P_{\mathrm{RX}} = P_{\mathrm{RX,TM}} + P_{\mathrm{RX,TE}}\,. \tag{5.31}$$

5.4.6 On-Body Path Gain

The path gain of an on-body propagation scenario, consisting of a transmitting antenna TX and a receiving antenna RX, can be calculated directly using (5.24)–(5.31). If we, for instance, set the radiated power of the transmitter to unity, the path gain *PG* is

$$PG = -\frac{\pi}{\gamma_0^2}\Big(D_{\mathrm{TM,TX}} D_{\mathrm{TM,RX}} \operatorname{Re}\left\{S^{\mathrm{ff}}_{\mathrm{TM,\rho,TX}}\right\} + \\ + D_{\mathrm{TE,TX}} D_{\mathrm{TE,RX}} \operatorname{Re}\left\{S^{\mathrm{ff}}_{\mathrm{TE,\rho,TX}}\right\}\Big). \tag{5.32}$$

In this case, the equivalent dipole momentum of our far field description becomes

$$\left|p^{\mathrm{ff}}_{\mathrm{iso}}\right|^2 = \frac{4\pi}{\eta_0 \gamma_0^2}. \tag{5.33}$$

to result in a conformal expression in terms of units.

It is inevitable to use the same Bannister parameters, i.e. frequency, ground parameters, effective antenna height, to calculate the antenna directivity values and the equivalent antenna far field. However, despite this restriction, (5.32) enables an evaluation of wireless on-body links by concentrated antenna parameters. Considering all results of the current chapter, this means that the current distributions on the antennas can be used to model the whole on-body propagation power budget. Thereby, different antenna combinations can be analyzed on the same on-body channel efficiently. Even if a modified channel is required, e.g. if the tissue parameters of the ground have to be adjusted, the corresponding adaption can be done with small effort by a recalculation of the antenna current distribution and the related antenna parameters. In this respect, a variation of the target frequency can be done, which enables the discussion of wide band antenna structures in terms of on-body communications for discrete frequency points. By this, even the dispersive nature of human tissues is included in the deduced antenna parameters.

5.4.7 Estimation of the Effective Antenna Height

As seen above, the derived antenna parameters are calculated assuming the normal and tangential equivalent on-body sources of Fig. 5-14. Therefore, strictly seen, the corresponding values are restricted to the chosen equivalent sources setup, i.e. frequency, coordinate origin, tissue type, and effective height. While we have in principle the free choice of defining these values, a careful selection of parameters that are linked to the underlying setup is preferable. Thereby, insight into related propagation mechanisms, e.g. the dominate wave form, is enabled. With dipole antennas in mind, we estimate the effective antenna height by the geometrical center of the dipole. In the context of arbitrarily shaped antenna structures, such a direct relationship is not feasible in general.

In our case, we use a method to estimate the effective antenna height by the current distribution on the segmented antenna structure. For this purpose, we calculate a weighting factor s_i of each spatial cell, which sets the current density in z direction in relation to the total current density of the cell. If we multiply the height of each cell with the corresponding weight factor, the effective height of the antenna arises from normalization to the total sum of all weight factors to

$$h = \frac{\sum_{i=1}^{M} s_i r_{0,z,i}}{\sum_{i=1}^{M} s_i} . \tag{5.34}$$

5.4.8 Example: Antenna: Half-Wave Dipole

In the following section, the on-body radiation characteristic is discussed using the examples of differently orientated electric half-wave dipoles. In this context, the on-body 2D radiation patterns are calculated by the directivity formulations of (5.24) and (5.25) using the numerically calculated current distribution on the antenna structure in the presence of a body phantom by the FDTD software [EMP]. The human body is represented by muscle tissue parameters that are taken from Table 4-1, and the effective antenna height of the equivalent sources is set to the center of the dipole. The axes of the dipole antennas are described by two angles in conjunction with spherical coordinates with θ_a and ϕ_a, as defined in Fig. 5.16, where the initial axis is aligned in z direction with $\theta_a = 0°$ and $\phi_a = 0°$.

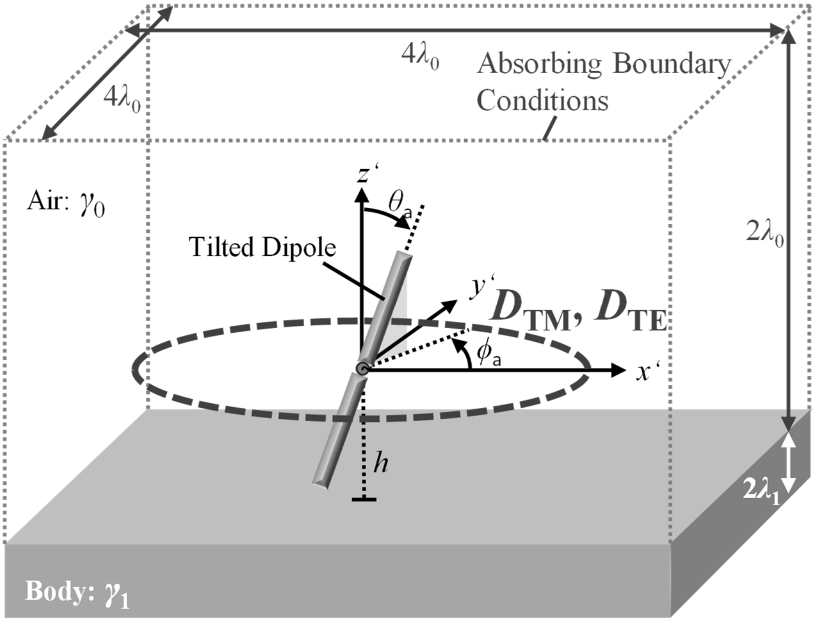

Fig. 5-16 [Gri15b]: Definition of the inclination angles θ_a and ϕ_a of a tilted dipole above a human body phantom at effective antenna height *h*. In addition, the schematic shows the on-body radiation pattern of the antenna, which is based on the equivalent sources at the antenna center.

The canonical dipole orientations of Bannister's formulation are discussed by half-wave dipoles at 2.45 GHz. The effective antenna height is set to a quarter of a free space wave length. Because of the thickness of the rod, the antenna is slightly shorter than a half wave length, and, therefore, an intersection with the phantom is avoided. As depicted by Fig. 5-17, the calculated directivity parameters indicate a TM field which equally radiates in all directions by the normally orientated dipole. The tangential dipole exhibits a mixed excitation, where the maximum of the radiated TM field and TE field is directed parallel, resp. perpendicular, to the dipole axis. In comparison, the difference of the maximum TM values of both orientations is around 20 dB, while the corresponding theoretical value $|\Delta|^2$ of (5.17) suggests a difference of 17.5 dB. This difference results from the numerically calculated field values and is related to the finite spatial segmentation of the antenna structure. In terms of the high dynamic range between the maximum TM and TE field values especially, the calculated value of the TE directivity includes a larger numerical error than the related TM values. Despite this aspect, the 2D on-body radiation pattern reveals the relationship between the antenna orientation and the resulting electromagnetic wave form.

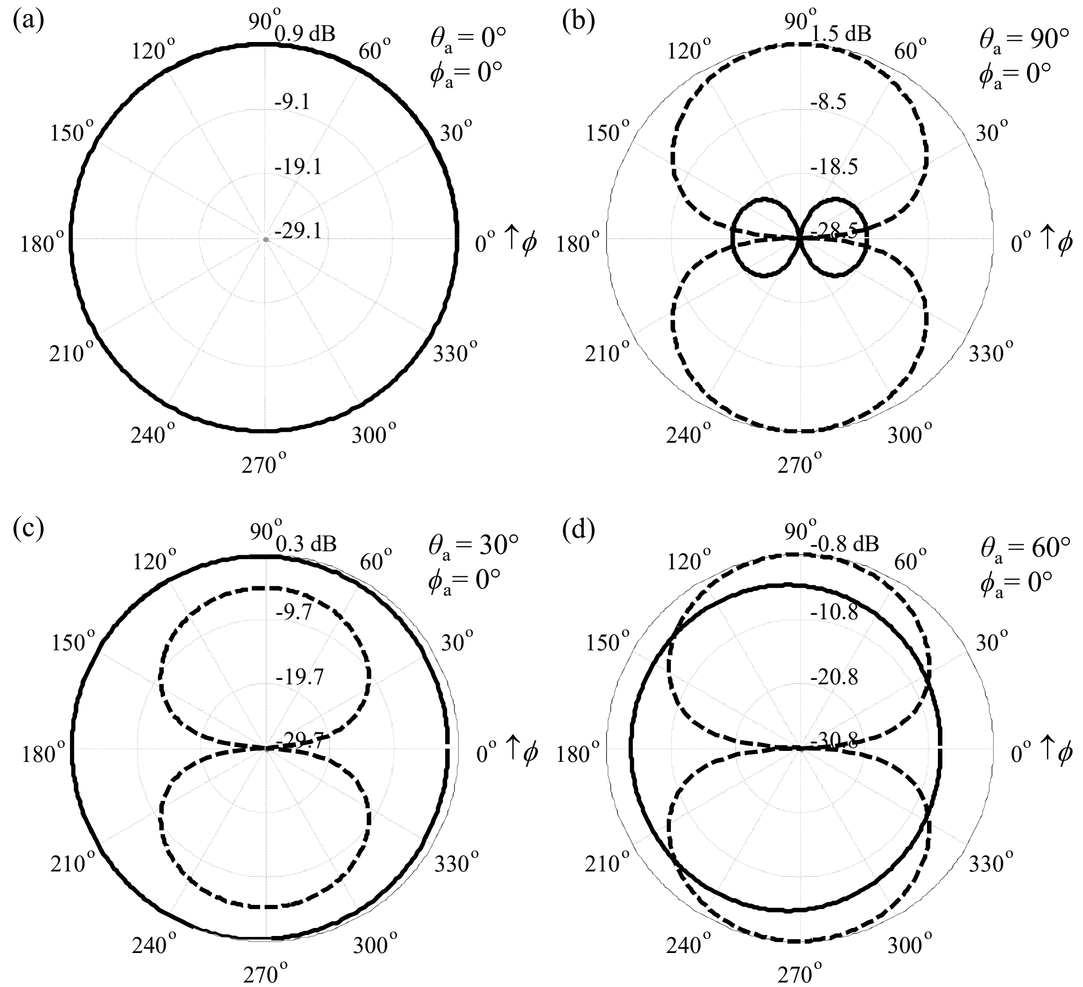

Fig. 5-17 [Gri15b]: Radiation pattern based on the on-body directivity of differently oriented electric half-wave dipoles ($h = \lambda_0/4$, $f = 2.45$ GHz, $\gamma_{\mathrm{muscle}} = (44.8 + j\,376)\ \mathrm{m}^{-1}$); Solid line: D_{TM}; Dashed line: D_{TE}; (a) Normal; (b) Tangential; (c) tilted by 30°; (d) tilted by 60°.

As can be seen from the radiation patterns, the antenna polarization is directly linked to the excited wave form. If, for instance, the normally orientated dipole is tilted toward the body surface, we can increase the magnitude of the TE wave component. As seen in Fig. 5-17, this is accompanied by a reduction in the TM component. In addition, we can observe a deformation of the initial omnidirectional TM pattern, where the difference between maximum and minimum values for $\theta_a = 30°$, resp. 60°, is 1.6 dB, resp. 4.3 dB. In order to obtain a better insight into the relationship between the dipole orientation and the resulting radiation characteristic, various configurations are calculated. The results are listed in Table 5-3, where the directivity is calculated for on-body paths in x direction.

TABLE 5-3
ON-BODY DIRECTIVITY OF TILTED HALF-WAVE DIPOLES IN X DIRECTION

		Label					
Value	Unit	A	B	C	D	E	F
θ_a	°	0	90	90	45	45	45
ϕ_a	°	0	0	90	0	45	90
D_{TM}	dB	0.90	-18.1	Inf.	-3.99	-2.19	-1.69
D_{TE}	dB	Inf.	Inf.	1.50	Inf.	-4.33	-1.69
		Label					
Value	Unit	G	H	I	J	K	L
θ_a	°	45	30	30	60	60	90
ϕ_a	°	180	0	180	0	180	30
D_{TM}	dB	-1.29	-1.32	0.29	-7.78	-3.37	-18.9
D_{TE}	dB	Inf.	Inf.	Inf.	Inf.	Inf.	-5.9

Using the directivity values of Table 5-3, the on-body path gain is calculated by (5.32). This enables a direct calculation of the on-body path gain of various dipole combinations. In this context, we are using different setups, and calculate the path gain for a propagation distance of three free space wave lengths at 2.45 GHz in x direction. To verify the validity of the approach, the path gain is calculated using the FDTD software [EMP]. The validation setups are computed for the same distance and equal antenna orientations. The path gain is calculated by the ratio of available power at the receiving antenna to the transmitted power.

TABLE 5-4
ON-BODY DIRECTIVITY OF TILTED HALF-WAVE DIPOLES IN X-DIRECTION

		Link					
Difference	Unit	AA	CC	AB	AF	AJ	CL
ΔPG	dB	0.17	0.08	7.52	0.05	1.67	0.06

The difference in the calculated path gain values of both methods is shown in Table 5-4. The results indicate that the theory is applicable to most of the combinations investigated. Only the scenario AB, where the link consists of a normally orientated transmitting dipole and a tangentially orientated receiving dipole, the axis of which points in x direction, shows a non-negligible error. As mentioned in the previous chapter, the inaccuracy is related to the two-source model we have selected that lacks the capability to describe the TM field of the tangential dipole by a normally orientated equivalent source for small antenna distances. However, if we increase the link distance e.g. to 10 free space wave lengths, the corresponding error is reduced to 3 dB and converges for an infinite distance to zero.

To obtain a better insight into the general applicability of our approach, the path gain is modeled by the concentrated on-body antenna parameters for the link combinations FA, FC, and FL as a function of the distance. In this context, the dipole orientation F is chosen due to the fact that equally weighted TM and TE waves are radiated in x direction. The FDTD validation setup is computed for the discrete antenna distances 0.3 m, 0.6 m, 0.9 m, and 1.2 m—see upper schematic of Fig. 5-18. Again, the numerical path gain is calculated by the ratio of available power at the receiving antenna to the transmitted power.

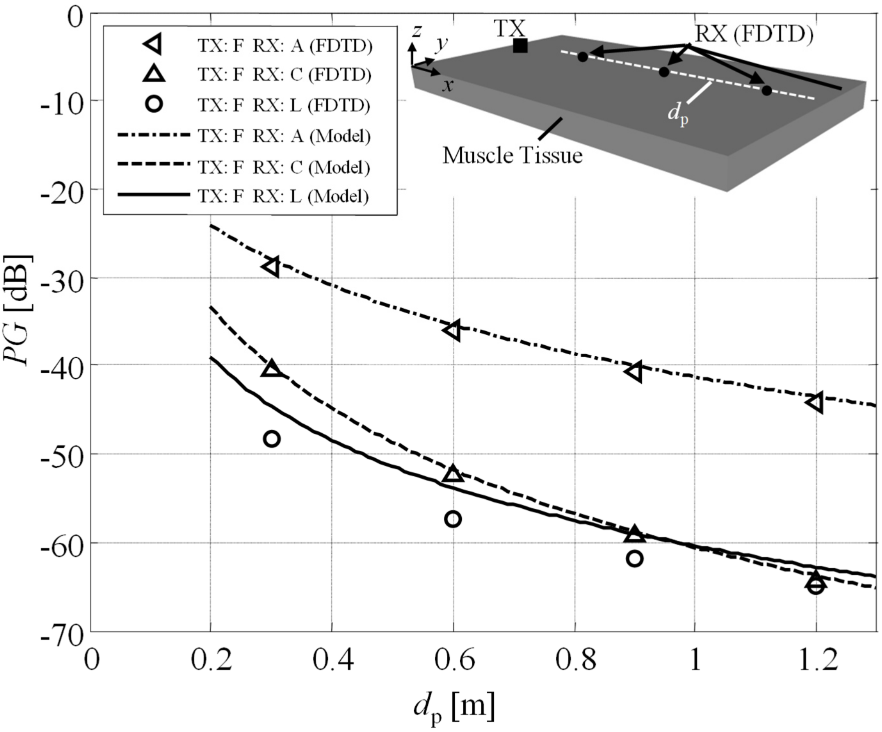

Fig. 5-18 [Gri15b]: Calculated on-body path gain of different half-wave dipole configurations by the deduced antenna parameters in relation to numerically calculated values; $f = 2.45$ GHz; $h = \lambda_0/4$; $\gamma_1 = (44.8 + j\,376)\ \text{m}^{-1}$.

The results shown in Fig. 5-18 indicate a good applicability of our approach. Even the link FL can be modeled accurately, although the receiving antenna is primarily aligned in the direction of the propagation.

5.4.9 Example: Planar Inverted-F Antenna

To verify the suggested approach in terms of more complex antenna structures, the on-body antenna parameters of a specific planar inverted-F antenna are calculated. As in the previous example, we have calculated the currents on the antenna body by the FDTD method under the influence of the immediate vicinity of the human body and modeled the antenna parameters by (5.24)–(5.28). Details on the antenna concept itself are in [Gri14c] and the primary design parameters are shown in Fig. 5-19 and Fig. 5-20.

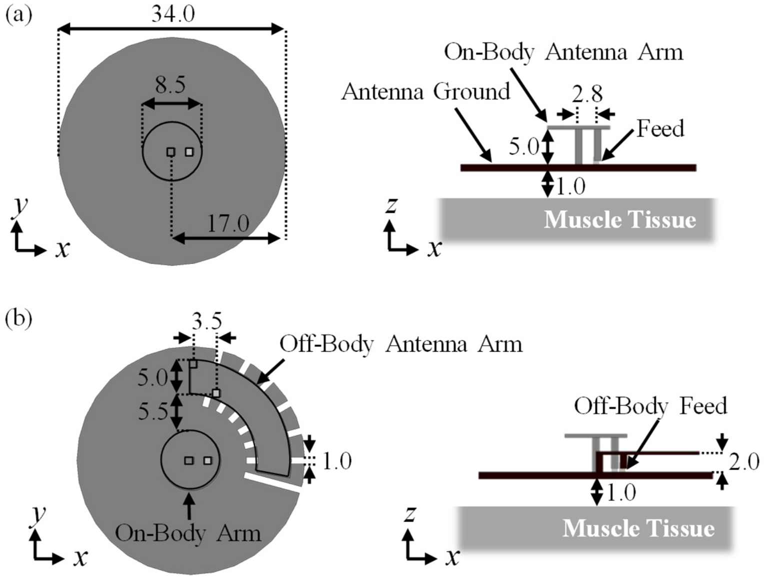
(a)
34.0
8.5
17.0
y
x
On-Body Antenna Arm
Antenna Ground
2.8
Feed
5.0
1.0
Muscle Tissue
z
x
(b)
3.5
Off-Body Antenna Arm
5.0
5.5
1.0
On-Body Arm
y
x
Off-Body Feed
2.0
1.0
Muscle Tissue
z
x

Fig. 5-19 [Gri15b]: Design parameters of an on-/off-body antenna concept, which was first presentenced in [Gri14c]; All measures are given in mm: (a) Planar inverted-F antenna feed for on-body communications at 5.4 GHz. (b) Extension of the on-body antenna concept by an off-body feed at 2.45 GHz.

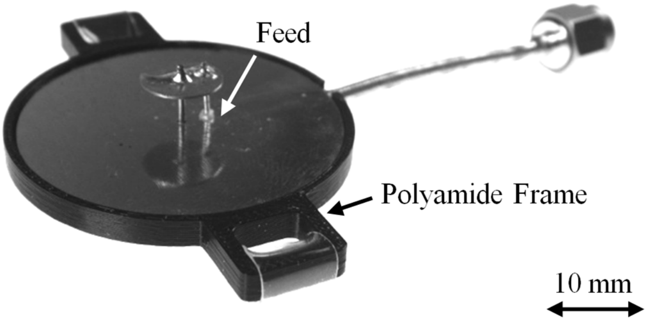
Feed
Polyamide Frame
10 mm

Fig. 5-20 Planar inverted-F antenna feed for on-body communications at 5.4 GHz. The polyamide frame is used to fix the antenna position by an elastic band on the human body.

The intention of the antenna concept is to enable a good on-body link performance. In addition, the antenna module has been extended by a secondary antenna structure that aims at off-body radiation at 2.45 GHz. As depicted by Fig. 5-21, the 2D radiation pattern shows in the case of an active on-body feed a dominant and nearly omnidirectional TM radiation characteristic, indicating, therefore, a strong excitation of Norton surface waves. This fact is related to the antenna feed, which excites a strong normal current distribution on the antenna body and so is preferable for on-body communications. On the other hand, the off-body feed shows a dominant TE component, which is preferable for off-body communication links.

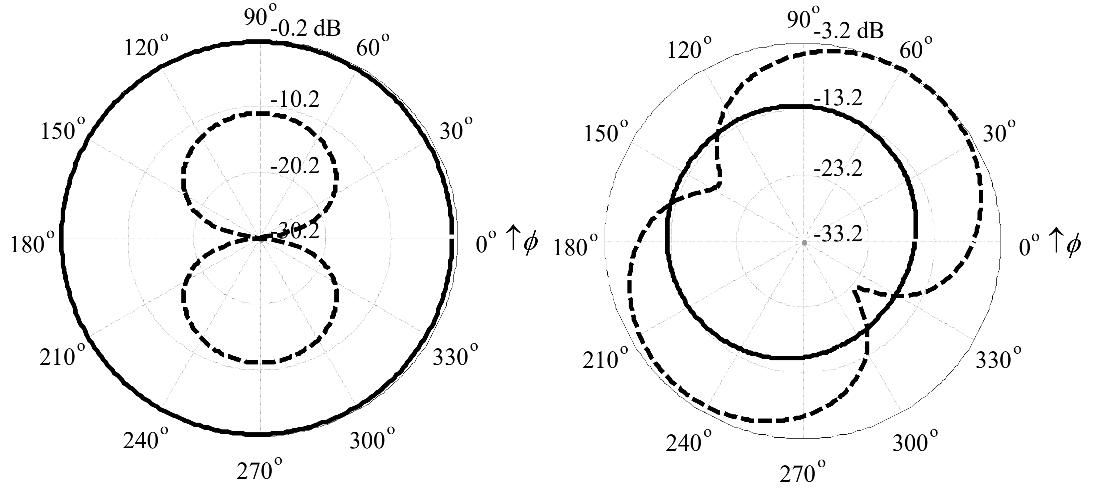
(a) On-body at 5.4 GHz

(b) Off-body at 2.45 GHz

Fig. 5-21 [Gri15b]: On-body radiation pattern of a planar inverted-F antenna with active (a) on-body antenna feed at 5.4 GHz and (b) off-body antenna feed at 2.45 GHz; Solid line: D_{TM}; Dashed line: D_{TE}.

To verify the accuracy of the derived values, we calculate the path gain of an on-body link, which consists of two planar inverted-F antennas of Fig. 5-19a, by the derived antenna parameters and (5.32). The verification of these results is done by the FDTD method [EMP] for eight discrete distance values. The related propagation path of the numerical model leads from the hip of the anatomical model "Duke" to the right foot. In addition, we have measured a corresponding propagation scenario in an anechoic chamber with two male volunteers of comparable body shape. The measurement is carried out using a vector network analyzer to trace the change of the transmission parameter between both antennas as a function of the distance to obtain the path gain. To ensure a minimal passive coupling between connecting cables and antennas, the cables have been directed as much as possible away from the propagation path. In addition, before performing each measurement, the cable positions have been varied in order to estimate the influence of the cables on our measurement results. Thereby, the cables are routed in such a way that each measurement is not significantly affected by changes of the cable positions. The corresponding results are shown in Fig. 5-22 and indicate a good applicability of the developed approach, even in terms of realistic propagation scenarios. In relation to the method presented in [Gri14c], the results show a better accuracy, which is related to the clear differentiation of the radiation characteristic in TM and TE component, where the preceding method only uses the total field.

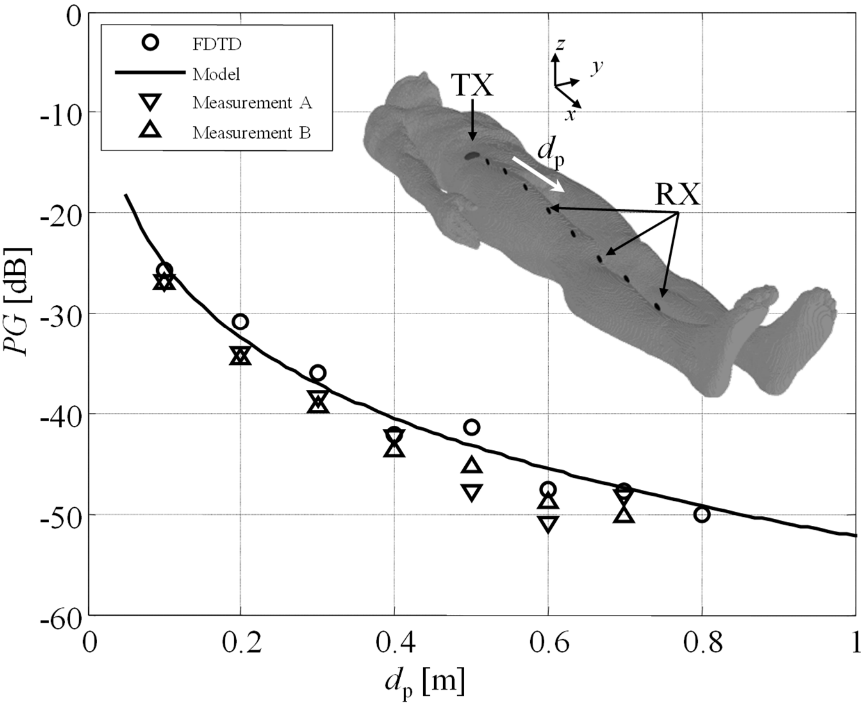

Fig. 5-22 [Gri15b]: On-body path gain of a planar inverted-F antenna concept along the leg of the numerical voxel model "Duke" at $f = 5.4$ GHz. The path gain has been modeled by the antenna parameters and is verified by numerical calculations and measurements.

5.5 Limitations of the Theory

Up to here, and in terms of the proceeding results, the underlying equations of Bannister assume a homogeneous flat ground. Having body-centric propagation scenarios in mind, this assumption is capable of describing the average mean value of the excited field if local irregularities of the surface occur, and even local variations of the ground properties may be compensated. Norton has discussed both facts in terms of terrestrial applications in [Nor37], and we have verified this in terms of on-body propagations in [Gri14b]. Nevertheless, this approach is primarily restricted to line-of-sight links along the human body. In conjunction with [Hal06], the dielectric properties of the body are set to homogeneous muscle tissue, which is a common approach to model the human body at ISM bands below 10 GHz. If required, this model may even be adapted to a layered ground structure by the use of modified ground properties. In this context [Lea09] discusses a layered skin-fat-muscle tissue where the ground properties are modified by the surface impedance.

Because our approach is based on a finite segmentation of the antenna within the FDTD solution space, antenna concepts of infinite size, e.g. ideal traveling wave antennas or slot antennas in infinite screens, cannot be modeled, and have to be approximated by their finite-size practical representatives.

In terms of broad band antennas this method is applicable as long as the desired frequency band can be broken down into discrete frequency values, where the corresponding dielectric parameters are adapted to each frequency step. Therefore, our approach is limited if time-domain quantities, e.g. pulse distortion, are of interest.

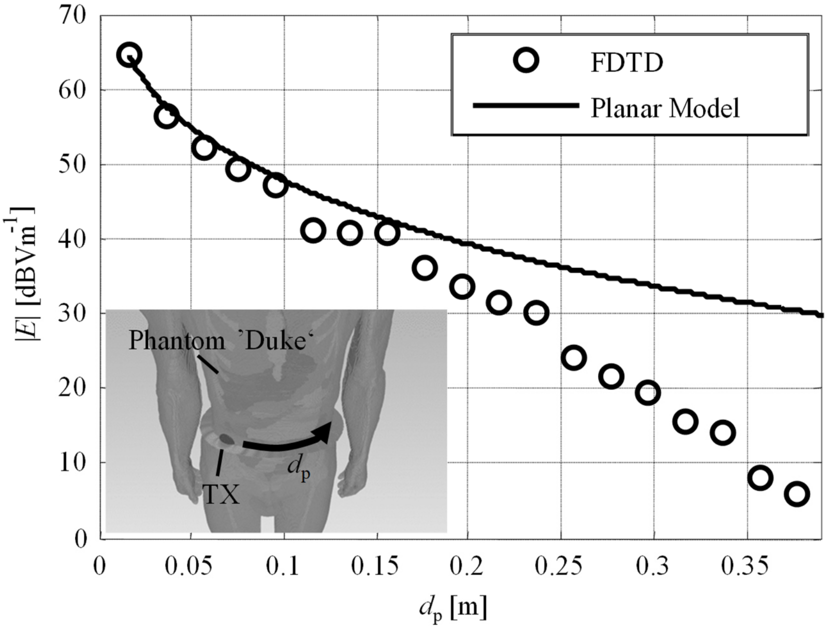

Fig. 5-23 Magnitude of the electric field along an on-body path around the trunk of the voxel model "Duke" in relation to the planar LOS channel model based on the Bannister solution; Antenna: on-body at $f = 5.4$ GHz.

The major drawback of the suggested theory is the lack of description of propagation paths that lead into permanently shadowed body regions. One possible scenario may arise if a link proceeds around the human trunk. As shown in Fig. 5-23, where such a setup is numerically evaluated on the basis of the example of the “Duke” voxel model, the electric field decreases so rapidly that for further distances, the planar on-body channel model is not capable of following the channel behavior. While in terms of near distances, a good match is achieved, the far field seems to be to be founded on other physical principles. Therefore, an adapted on-body channel model for non-line-of-sight propagation paths seems evident and is discussed in the next chapter.

Chapter 6

Non-Line-of-Sight On-Body Propagations

As seen in the previous chapters, the established on-body antenna theory is limited to line-of-sight propagation conditions. Therefore, in the context of the remainder of the thesis, a model for body-centric non-line-of-sight propagation conditions is developed. In this manner, that theory would be ideal that is compatible with the defined line-of-sight case, as well as with the derived on-body far field parameters. With this, scalable channel models would be acquired that are capable of dealing with nearly all available wireless propagation links along the human body. This implies, especially if we recall Fig. 5-1, an adapted NLOS far field model, which is compatible with the LOS planar model. A corresponding example in the case of a NLOS propagation link around the human trunk is shown in Fig. 6-1.

The following chapter is structured into two main sections. The first part discusses cylindrical models to describe the basic electromagnetic propagation effects of equivalent body-centric scenarios. Here, some general research attempts are introduced in brief, while in the course of the following work, the cylinder model of Chapter 3 is used. The second part adapts this cylindrical model to the planar model of Chapter 5, to describe propagation paths leading into body-shadowed non-line-of-sight regions. The main objective is, hereby, a good compatibility with the previously defined on-body antenna parameters. The defined theory is then evaluated by a propagation test scenario around the human trunk and verified by the FDTD method as well as by measurements in an anechoic chamber on the example of the planar inverted-F antenna, which is already discussed in terms of the planar LOS model of the previous chapter.

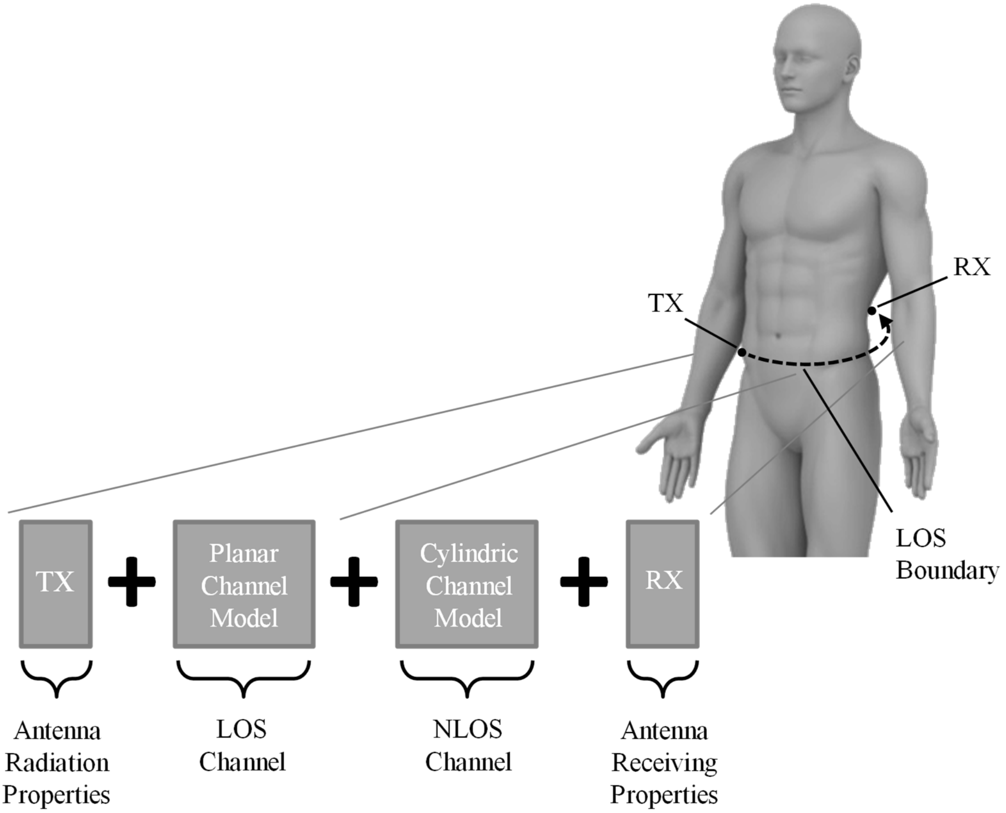
RX
TX
LOS
Boundary
TX
Planar
Channel
Model
Cylindric
Channel
Model
RX
Antenna
Radiation
Properties
LOS
Channel
NLOS
Channel
Antenna
Receiving
Properties

Fig. 6-1 Systematic modeling of a wireless on-body propagation link: Separated equivalent antenna and channel models are combined to describe the total propagation margin.

6.1 The Cylindrical Model in Relation with Full Human Body Models

In terms of body-centric communications, [For10] suggests the concept of a dissipative dielectric cylinder to model the path gain of propagation links around the human trunk and verifies the assumption by measurements on human test persons. The main benefit of this model is the availability of all field components for the whole solution space. The main drawback results from the solution concept itself, which is limited to tangential (in relation to the cylinder surface) antenna polarizations. This fact is especially restrictive if we have Norton's derivations in mind, which state that a normal antenna polarization contributes significantly to the on-body propagation.

Another NLOS approach is presented in [Alv11], which derives a corresponding cylindrical model from the creeping wave theory of wireless terrestrial communications. In this context, [Wai60] indicates that bended dielectric surfaces are capable of preserving electromagnetic wave modes which travel in such non-line-of-sight regions, where the key points of the theory are summarized in [Wai98]. This model is adapted in [Alv11] to describe the path gain around the human trunk and is verified by measurements of specific antenna setups on human test persons, where the results indicate a good applicability of the suggested model. The advantage of this model is a straightforward path gain model with relative less effort. In contrast, the model gives no direct insight into the separated field quantities for a specific antenna configuration and achieves the results only by approximation of free space antenna parameters and reference measurements. In addition, this fact makes it difficult to adapt the desired NLOS model to our derived on-body antenna parameters of Chapter 5. Keeping this aspect in mind, and especially the geometric versatility of the first model, the following NLOS model is based on an adaption of the theory of [For10], and is discussed in the following.

6.1.1 Comparison between Theoretical and Numerical Models

As seen in Chapter 3, the suggested cylindrical model is capable of describing the radiated field of the tangential dipoles $\mathbf{p}_2$ and $\mathbf{p}_3$ along the on-body path d_p. The corresponding setup is summarized in Fig. 6-2, where the related dipole is positioned in free space γ_0 at effective antenna height h above the dissipative dielectric cylinder γ_1 with radius a.

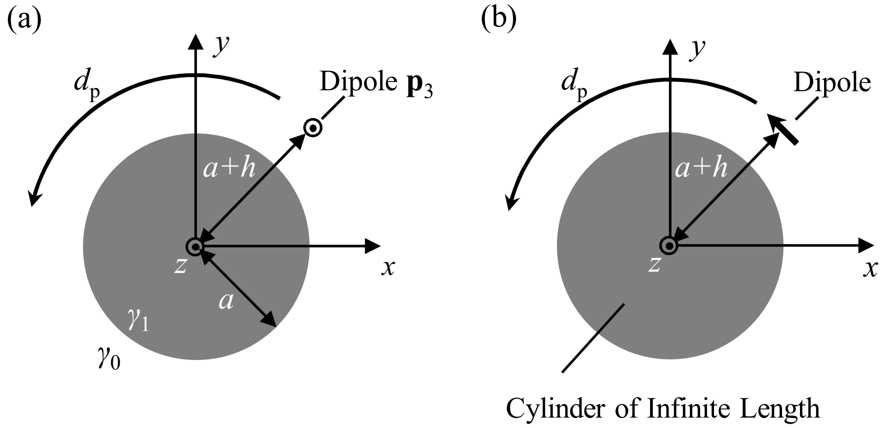

Fig. 6-2 Evaluation setup to compare the tangential dipole orientations $\mathbf{p}_2$ and $\mathbf{p}_3$ of the cylindrical model in relation to equivalent FDTD models.

To verify the cylinder model presented in Chapter 3, the magnitude of the power flux density along the on-body path d_p is calculated by the model and the FDTD method. In terms of the cylindrical model, the radiated field of dipole $\mathbf{p}_3$ is calculated by (3.20)–(3.27) using the related coefficients of (3.32), and the field of $\mathbf{p}_2$ by (3.37)–(3.47), considering (3.50). The cylinder radius is set to $a = 0.15$m to model a bending radius equal to the human trunk of the "Duke" voxel model and set to the properties of homogeneous muscle tissue at a solution frequency of $f = 2.45$ GHz. The effective antenna height is set to $h = \lambda_0/4$. Further, the FDTD method assumes a half-wave dipole. To compensate losses related to detuning effects and the directivity of the half-wave dipole, the far field model calculated by the cylindrical model is normalized to the results of the FDTD model at $d_p = 0.1$ m. The results of both methods are shown in Fig. 6-3 for both antenna orientations.

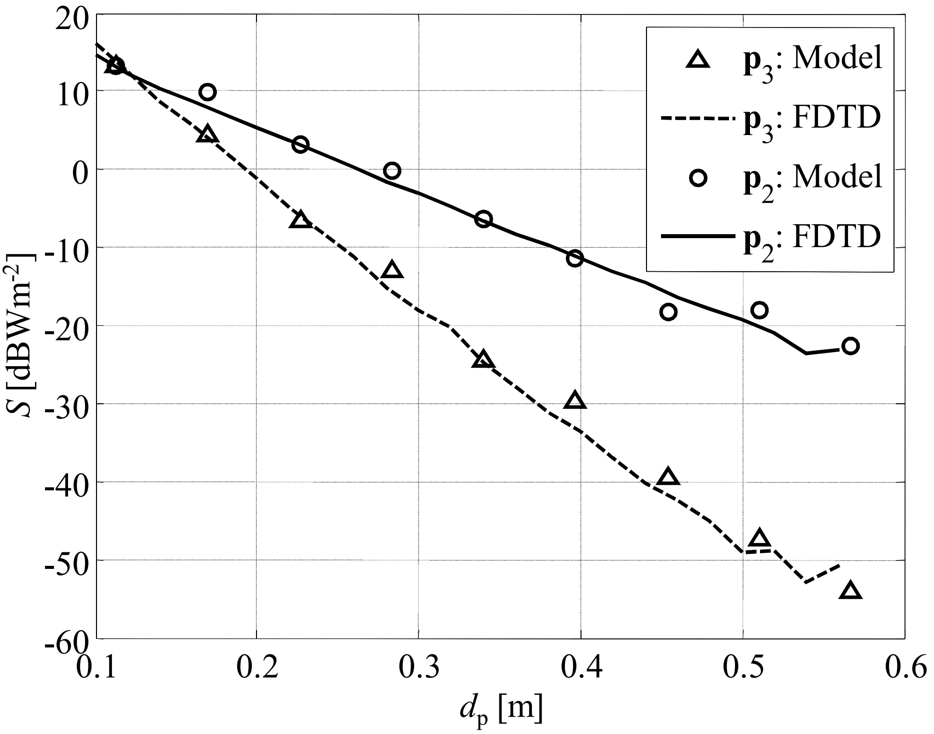

Fig. 6-3 Magnitude of the power flux density along the path around the cylinder ($a = 0.15$ m, $f = 2.45$ GHz, $\gamma_1 = (44.8 + j\,376)$ m^{-1}). Lines: Calculated by the FDTD method; Doted values: Calculation based on the cylindrical model.

Considering the results, both methods show good agreement with each other, and, therefore, imply a good applicability of the cylindrical setup as an on-body far field model. The small fluctuations are related to numerical errors. In terms of the cylindrical model, these fluctuations can be led back to the discretization of the contour integral of Fig. 3-3 as well as the representation of the Bessel and Hankel functions by an infinite number of elements. This error vanishes at the main field component and arises primarily from the weaker field components. As seen in [For10], the chosen contour has an effect on the solution time as well as the numerical error. In our case, we have chosen a contour with $C = 20$, which results in a fast derivation time as well as the numerical error that occurs.

6.2 Modeling of the Radiated NLOS Antenna Field

To develop a consistent NLOS channel model, the total characteristic of the channel has to be broken down into a TM- and a TE-related NLOS far field. As defined in Fig. 5-14, to satisfy this demand, we need the equivalent dipole configurations $\mathbf{p}_{\mathrm{TM}}$ and $\mathbf{p}_{\mathrm{TE}}$. As $\mathbf{p}_{\mathrm{TE}}$ corresponds to the tangential dipole orientation $\mathbf{p}_3$, unfortunately, $\mathbf{p}_{\mathrm{TM}}$ is defined using the dipole orientation $\mathbf{p}_1$. And here, as mentioned above, related to the solution of tangential boundary conditions of (3.32) and (3.50), the cylindrical model is not capable of delivering a solution of the normal dipole orientation $\mathbf{p}_1$. In the following, a workaround for this problem is delivered, and a method to model the general radiated antenna far field for non-line-of-sight scenarios is defined.

6.2.1 Analogy Considerations in Terms of the Planar Model

In case of the planar model, as demonstrated in the previous chapter, we are capable of describing the radiated TM component of the antenna far field by one single dipole. This approach uses the fact that the far field of the dipole $\mathbf{p}_1$ and $\mathbf{p}_2$ converges into each other for sufficient far distances. If we consider the planar case as a cylinder with infinite radius a, the effects of the primary propagations should nearly be the same if we slowly decrease the radius. Moreover, if we significantly decrease the bending radius, the weighting of the contribution wave modes may change in relation to the planar case, but the general wave form remains. This implies that in case of the cylindrical model, the tangential dipole orientation $\mathbf{p}_2$ can still describe the TM antenna far field and, therefore, may deliver a TM NLOS far field model. To evaluate this assumption, the previous geometry of Fig. 6-2 is revisited, extended by the normal dipole orientation $\mathbf{p}_1$ and solved by the FDTD method. As the illustrated results in Fig. 6-4 reveal, the radiated power flux density of the dipoles $\mathbf{p}_1$ and $\mathbf{p}_2$ show at quasi-static distances significant differences in their field behavior, but for farther distances, e.g. at distances above 0.1 m, the field components decay parallel to each other while the magnitude of the orientation $\mathbf{p}_3$ drops in a significantly stronger manner.

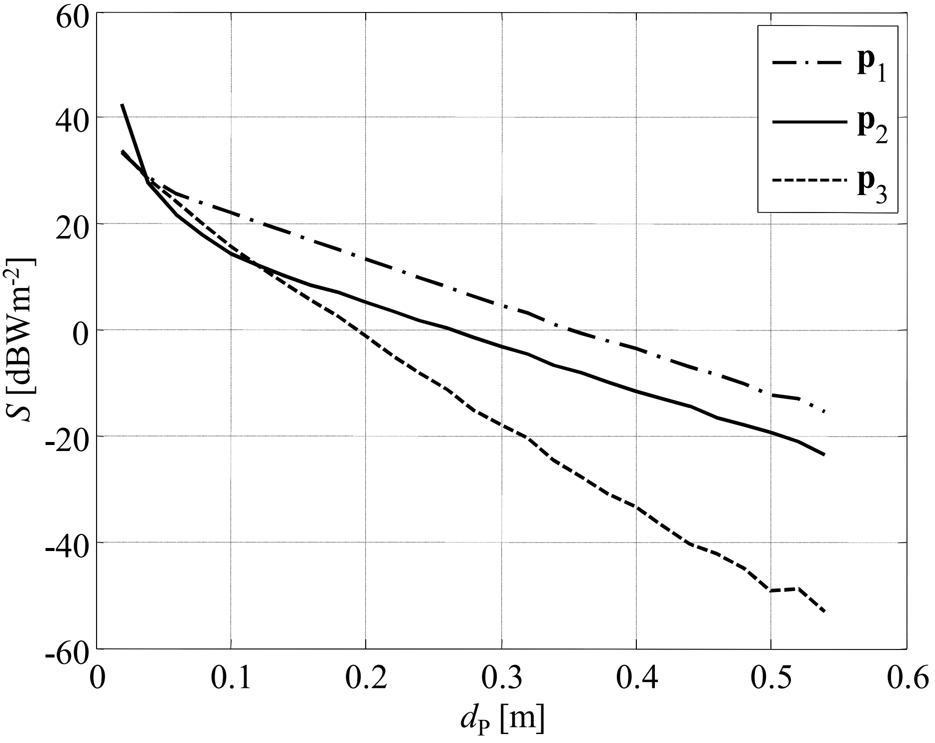

Fig. 6-4 Magnitude of the power flux density along the path around the cylinder ($a = 0.15$ m, $f = 2.45$ GHz, $\gamma_l = (44.8 + j\,376)$ m^{-1}) calculated by the FDTD method of the three basic dipole orientations.

The assumption is consolidated if we compare (3.28) and (3.29) with (3.46) and (3.47), where $\mathbf{p}_2$ shows a TM and $\mathbf{p}_3$ a TE radiation characteristic. This implies that the NLOS channel can be modeled as well as the planar model by a separated TM and TE antenna far field, where the dipole orientation $\mathbf{p}_2$, resp. $\mathbf{p}_3$, can be used to calculate the TM, resp. TE, far field behavior. Related to the theory, as described in Chapter 3, we are now capable of calculating the average electromagnetic field behavior around the human trunk as a function of various parameters, e.g. frequency, effective antenna height and bending radius.

6.2.2 Non-Line-of-Sight Far Field Model

As discussed above, the possible separation of the NLOS on-body far field in TM and TE far field components enables a treatment of such scenarios as channel modification of the planar case. To realize the systematic model of Fig. 6-1, we can now use the derived on-body parameters of Chapter 5 to calculate the radiated antenna field. Owing to the underlying field equations, which are based on Bannister's solution and so are applicable to quasi-static ranges, the solution is appropriate for planar path segments $d_{\mathrm{p},1}$ near the antenna. Even for scenarios where the antenna is positioned in regions of small bending radii, the steady adaption of the electromagnetic field enables the description of the field within the quasi-static field range. The EM field along the following NLOS path segment $d_{\mathrm{p},2}$ is than estimated by the cylindrical model and normalized to the underlying LOS values. The general procedure is illustrated in Fig. 6-5 where, on the example of an on-body path around the human trunk the total observation path is systematically divided into a planar and a cylindrical model.

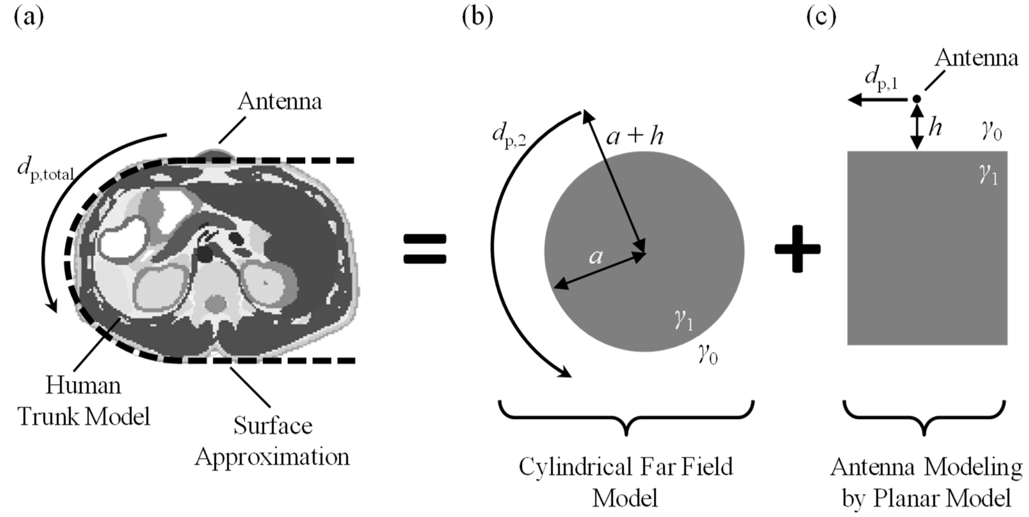
(a)
(b)
(c)
Antenna
$d_{\mathrm{p,total}}$
Human Trunk Model
Surface Approximation
$d_{\mathrm{p},2}$
$a + h$
a
γ_1
γ_0
Cylindrical Far Field Model
Antenna
$d_{\mathrm{p},1}$
h
γ_0
γ_1
Antenna Modeling by Planar Model

Fig. 6-5 On-body antenna and far field modeling: (a) General on-body propagation path $d_{\mathrm{p,total}}$ leading around the human trunk; (b) Cylindrical far field model to model the NLOS path segment $d_{\mathrm{p},2}$; (c) Planar model to model the coupling between antenna/human body and the quasi-static path segment $d_{\mathrm{p},1}$.

As shown in [For10] and [Alv11], the field quantities related to an on-body path around a dissipative dielectric cylindrical surface decay exponential with increasing distances d_p. Knowing this behavior, it enables a direct extraction of the average field attenuation factor from our cylindrical model. To normalize the NLOS description to the LOS model, we can now define the normalization distance d_pn to calculate the related field quantity along the bended path d_p. In case of the TM component, the related model function of the magnitude of the complex electric field is given by

$$E_\mathrm{TM,NLOS} = E_\mathrm{TM,LOS}(d_\mathrm{pn}) \cdot e^{-\alpha_\mathrm{E,TM}(d_\mathrm{p}-d_\mathrm{pn})}, \tag{6.1}$$

where $\alpha_\mathrm{E,TM}$ is the complex attenuation function of the TM field component. Defining the complex TE attenuation function $\alpha_\mathrm{E,TE}$, an equal expression can be given for the TE component with

$$E_\mathrm{TE,NLOS} = E_\mathrm{TE,LOS}(d_\mathrm{pn}) \cdot e^{-\alpha_\mathrm{E,TE}(d_\mathrm{p}-d_\mathrm{pn})}. \tag{6.2}$$

Equations (6.1) and (6.2) can be found for the magnitude values as well as for each field component. Finally, the total electric field results from the combined vector components of the TM and TE field with

$$\mathbf{E}_\mathrm{NLOS} = \mathbf{E}_\mathrm{TM,NLOS} + \mathbf{E}_\mathrm{TE,NLOS}. \tag{6.3}$$

Here, the normalization values $E_\mathrm{TM,LOS}$ and $E_\mathrm{TE,LOS}$ at normalization distance d_pn are calculated by the planar model, i.e. utilizing (5.26), resp. (5.27). In the same way, the magnetic field components can be modeled. Using the Poynting vector, the power flux density can be calculated and, considering (5.29)–(5.31), even the path gain can be obtained in case of non-line-of-sight propagations.

In general, the normalization distance is not equal to the maximum distance segment value $d_\mathrm{p,1}$ as defined by Fig. 6-5. Instead, the propagating wave has to converge from the planar geometry to the cylindrical geometry. Based on our calculations, it seems that this process takes place in terms of surface bound antennas along a distance of around a free space wave length, i.e. the normalization distance d_pn should set to $d_\mathrm{p,1} + \lambda_0$.

6.2.3 Discussion on Channel Parameters as a Function of the Body Geometry

The option to model the electric field quantities, and the linked values, by an intuitive exponential function enables a straightforward discussion of the NLOS channel characteristic. This means that general setup parameters, such as frequency, effective antenna height, polarization, bending radius and tissue type, may be varied, and the resulting change in the attenuation function can be evaluated in terms of NLOS propagations. The discussion of the power flux density seems especially favorable, as it is by (5.32) directly related to the path gain. In conjunction with (6.1) and (6.2), we can define the magnitude of the power flux density by

$$S_{\mathrm{NLOS}} = S_{\mathrm{LOS}}(d_{\mathrm{pn}}) \cdot e^{-|\alpha_{\mathrm{S}}|(d_{\mathrm{p}} - d_{\mathrm{pn}})}, \tag{6.4}$$

where $|\alpha_{\mathrm{S}}|$ is either calculated for the TM or TE case. On the example of a low-profile antenna concept, i.e. the effective antenna height is set to a tenth of a free space wave length, Fig. 6-6 shows a discussion of the attenuation function as a function of the bending radius a for the TM and TE case. The frequency of interest is set to $f = 2.45$ GHz, $f = 5.4$ GHz, and $f = 10$ GHz, while the dielectric properties of the cylinder are assumed to be homogeneous muscle tissue.

As seen from the results of Fig. 6-6, the attenuation decreases with increasing bending radius. While a radius of $a = 0.05$ m is within the range of the radius of a leg, a radius with $a = 0.5$ m tends to represent a slightly bended propagation path above the trunk. If we consider, for instance, the antenna concept of Fig. 5-19, i.e. the frequency is 5.4 GHz and we only consider a TM propagation, the first case shows in comparison to the second case a four times higher attenuation function, while the second case tends to converge to the attenuation behavior of the planar model. In addition, we can observe that the TE case suffers from stronger attenuation effects than the corresponding TM scenario. If we consider the variation in the frequency, the TM propagation link strength benefits from a lower attenuation factor, while the TE case shows the opposite dependency for small bending radii and adapts to the TE behavior for nearly planar propagation conditions.

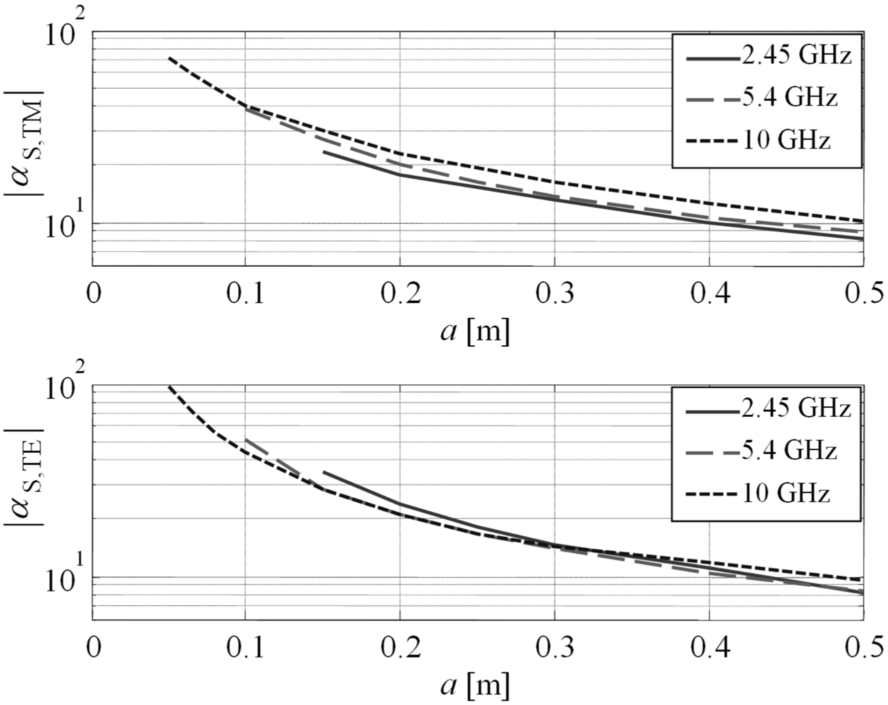

Fig. 6-6 Absolute value of the NLOS attenuation coefficient α_S of the magnitude of the power flux density along an on-body path around a muscle tissue like cylinder with radius a for TM and TE propagations (path height $h = \lambda_0/10$).

6.2.4 Example: On-Body PIFA on Human Trunk

In the following, the planar inverted-F antenna concept of Fig. 5-19 is used to evaluate the theory for a given on-body NLOS scenario. The radiating antenna is positioned on the belly of the human body. The receiving antenna is assumed to be moved around the trunk to the back. The general geometry is shown by an axial cut of the “Duke” voxel phantom in Fig. 6-7 at waist height.

The approximated circumference of the “Duke” model at this cut level is around 0.72 m. Related to the approximated geometry, a planar model is assumed for distances below $d_p = 0.05$ m, while further distances are modeled by a homogeneous muscle tissue like cylinder with radius $a = 0.105$ m. The whole on-body path d_p is estimated to proceed at an effective antenna height of $h \approx \lambda_0/10$ which is approximated by (5.34). The normalization distance is set at $d_{pn} = 0.05 \text{ m} + \lambda_0 \approx 0.1$ m. The general setup is evaluated by the FDTD method as well as by measurements in an anechoic chamber on two different test persons using a vector network analyzer to trace the change of the transmission parameter between both antennas as a function of the distance to obtain the path gain. Corresponding to the measurements on the leg, a minimal coupling between connecting cables and antennas by sheath currents has been minimized as cable positions pointing away from the main link path. Also, before performing each measurement, the position of the cables is varied in order to minimize the influence of the cables on our measurement results. The test persons as well as the voxel model are positioned in such a way that the arms are lifted to the shoulder level to minimize disturbing reflections. The resultant path gain of all methods is shown in Fig. 6-7 and indicates a good applicability of the non-line-of-sight approach that has been developed.

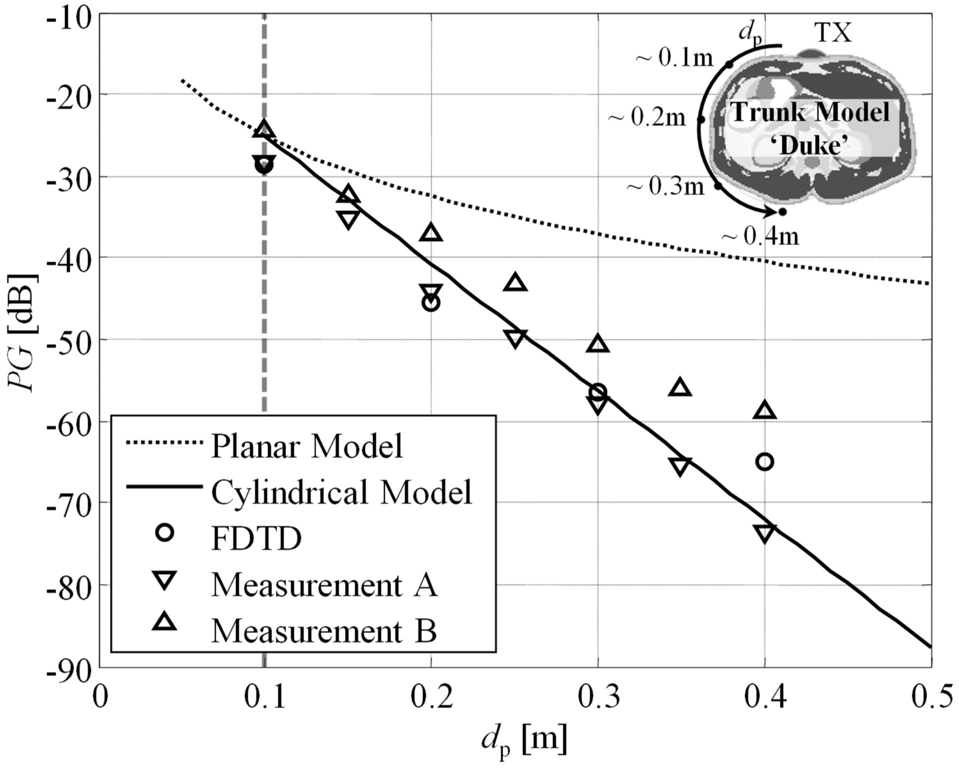

Fig. 6-7 On-body path gain of a planar inverted-F antenna concept around the trunk of the numerical voxel model “Duke” at $f = 5.4$ GHz. Dotted line: Path gain below $d_p = 0.1$ m has been modeled by the antenna parameters of the planar model; Solid line: Distances further than $d_p = 0.1$ m are modeled by the cylindrical model; Circle values: Evaluation values calculated by the FDTD method; Triangle values: Measurements in anechoic chamber.

Chapter 7

Conclusion

This thesis presents an approach that deals with certain key problems to model wearable wireless applications under the aspect of body-centric communications. Hereby, the focus is on a method to derive antenna body-centric parameters that can be used in an intuitive manner, as known, by the well-established free space antenna theory.

The results of the thesis indicate a good applicability of the Bannister model to on-body propagations, especially for high water content tissues like muscle and skin. Moreover, quantities like the numerical distance and the ratio of the space wave to the Norton surface wave are useful measures to evaluate the propagation mechanisms of a certain application field. Particularly advantageous is the fact that the numerical distance offers a direct insight into the body-centric propagation mechanisms, including frequency and media parameters, without the need for the closed solution of related field equations. Furthermore, the ground wave theory enables a determination of optimal coupling conditions, either for the excitation of Norton surface wave or space waves, which are valuable for the purpose of antenna design.

In addition, a method to model the radiated on-body field of arbitrarily shaped antennas by a combined numerical and analytical approach is presented. It includes a definition of the corresponding on-body directivity and on-body effective antenna area. Based on the TM and TE field components, this enables the definition of a 2D on-body radiation pattern, which is discussed through canonical and realistic examples. This antenna de-embedding concept enables the calculation of the on-body path gain under the premise that they can be sufficiently approximated by a homogeneous planar ground. In comparison with entire full-wave simulations of whole on-body links scenarios, including transmitting antenna, channel, and receiving antenna, this approach enables a more flexible testing of different antenna configurations. Finally, it can help us gain a better understanding of which antenna characteristic should be used for a specific on-body channel.

Because of the underlying planar phantom, the given theory is, in the first place, restricted to line-of-sight links. Despite this fact, the results reveal a dominant Norton surface wave component of antennas located in close proximity of the body surface. While the diffraction effects of the space wave component may have no notable contribution to non-line-of-sight links, the surface guided character of the Norton surface wave may help us reach shadowed body regions. For these scenarios, a transfer of the Norton surface wave theory in terms of a bended ground seems desirable, as the dominating wave species seems to be preserved.

To cover non-line-of-sight propagation cases, a dissipative dielectric cylinder model is used to estimate the corresponding radiated electromagnetic field as a function of the bending radii and other exchangeable parameters. The related field quantities can hereby be described by an exponential attenuation function, which can be treated as a related far field channel parameter of the planar model. This adaption allows the characterization of body-worn antennas even in case of non-line-of-sight propagations by TM- and TE-equivalent far field parameters. Moreover, the combination of the LOS and NLOS models enable an evaluation of a huge number of possible on-body link combinations by scalable propagation parameters, while the defined antenna measures can be used to classify the related antenna performance in these scenarios.

Appendix A

A1 Recurrence Formula of the Bessel Equation

The recurrence formula B'_m of a given Bessel or Hankel function of the first or second kind B_m is defined by [Ref_Chew] for cylindrical coordinates as follows:

$$B'_m\left(k_\rho\rho\right)=B_{m-1}\left(k_\rho\rho\right)-\frac{m}{k_\rho\rho}B_m\left(k_\rho\rho\right) \tag{A1.1}$$

$$=-B_{m+1}\left(k_\rho\rho\right)+\frac{m}{k_\rho\rho}B_m\left(k_\rho\rho\right). \tag{A1.2}$$

The derivation of the Function B_m is, therefore, related to its recurrence formula by

$$\frac{\mathrm{d}B_m\left(k_\rho\rho\right)}{\mathrm{d}\rho}=k_\rho\left[B_{m-1}\left(k_\rho\rho\right)-\frac{m}{k_\rho\rho}B_m\left(k_\rho\rho\right)\right]=k_\rho B'_m\left(k_\rho\rho\right). \tag{A1.3}$$

Appendix B

B1 Gabriel Parameters of Human Body Tissues

	ε_∞	$\Delta\varepsilon_1$	$\tau_1(ps)$	α_1	$\Delta\varepsilon_2$	$\tau_2(ns)$	α_2	σ_i	$\Delta\varepsilon_3$	$\tau_3(\mu s)$	α_3	$\Delta\varepsilon_4$	$\tau_4(ms)$	α_4
Aorta	4.00	40.0	8.842	0.10	50	3.183	0.10	0.250	1.0E+5	159.155	0.20	1.0E+7	1.592	0.00
Bladder	2.50	16.0	8.842	0.10	400	159.155	0.10	0.200	1.0E+5	159.155	0.20	1.0E+7	15.915	0.00
Blood	4.00	56.0	8.377	0.10	5200	132.629	0.10	0.700	0.0E+0	159.155	0.20	0.0E+0	15.915	0.00
Bone (Cancellous)	2.50	18.0	13.263	0.22	300	79.577	0.25	0.070	2.0E+4	159.155	0.20	2.0E+7	15.915	0.00
Bone (Cortical)	2.50	10.0	13.263	0.20	180	79.577	0.20	0.020	5.0E+3	159.155	0.20	1.0E+5	15.915	0.00
Brain (Grey Matter)	4.00	45.0	7.958	0.10	400	15.915	0.15	0.020	2.0E+5	106.103	0.22	4.5E+7	5.305	0.00
Breast fat	2.50	3.00	17.680	0.10	15	63.660	0.10	0.010	5.0E+4	454.700	0.10	2.0E+7	13.260	0.00
Cartilage	4.00	38.0	13.263	0.15	2500	144.686	0.15	0.150	1.0E+5	318.310	0.10	4.0E+7	15.915	0.00
Cerebro Spinal Fluid	4.00	65.0	7.958	0.10	40	1.592	0.00	2.000	0.0E+0	159.155	0.00	0.0E+0	15.915	0.00
Cornea	4.00	48.0	7.958	0.10	4000	159.155	0.05	0.400	1.0E+5	15.915	0.20	4.0E+7	15.915	0.00
Eye Tissues (Sclera)	4.00	50.0	7.958	0.10	4000	159.155	0.10	0.500	1.0E+5	159.155	0.20	5.0E+6	15.915	0.00
Fat (Average Infil.)	2.50	9.00	7.958	0.20	35	15.915	0.10	0.035	3.3E+4	159.155	0.05	1.0E+7	15.915	0.01
Gall Bladder Bile	4.00	66.0	7.579	0.05	50	1.592	0.00	1.400	0.0E+0	159.155	0.20	0.0E+0	15.915	0.20
Heart	4.00	50.0	7.958	0.10	1200	159.155	0.05	0.050	4.5E+5	72.343	0.22	2.5E+7	4.547	0.00
Kidney	4.00	47.0	7.958	0.10	3500	198.944	0.22	0.050	2.5E+5	79.577	0.22	3.0E+7	4.547	0.00
Liver	4.00	39.0	8.842	0.10	6000	530.516	0.20	0.020	5.0E+4	22.736	0.20	3.0E+7	15.915	0.05
Lung (Inflated)	2.50	18.0	7.958	0.10	500	63.662	0.10	0.030	2.5E+5	159.155	0.20	4.0E+7	7.958	0.00
Muscle	4.00	50.0	7.234	0.10	7000	353.678	0.10	0.200	1.2E+6	318.310	0.10	2.5E+7	2.274	0.00
Skin (Dry)	4.00	32.0	7.234	0.00	1100	32.481	0.20	0.000	0.0E+0	159.155	0.20	0.0E+0	15.915	0.20
Skin (Wet)	4.00	39.0	7.958	0.10	280	79.577	0.00	0.000	3.0E+4	1.592	0.16	3.0E+4	1.592	0.20
Small Intestine	4.00	50.0	7.958	0.10	10000	159.155	0.10	0.500	5.0E+5	159.155	0.20	4.0E+7	15.915	0.00
Stomach	4.00	60.0	7.958	0.10	2000	79.577	0.10	0.500	1.0E+5	159.155	0.20	4.0E+7	15.915	0.00
Tongue	4.00	50.0	7.958	0.10	4000	159.155	0.10	0.250	1.0E+5	159.155	0.20	4.0E+7	15.915	0.00

Appendix C

C1 Ground Wave Attenuation Factors

As seen from (2.70) and (2.71), the radiated electric and magnetic fields can be broken down into a spatial attenuation term, which is proportional to ρ^{-1}, and a ground wave attenuation function N^{E}, resp. N^{H}. While magnitude of the excitation is directly proportional to the dipole momentum $p = I\ell$, the dipole position and orientation has a major effect on the radiated wave specie and, therefore, affects the connected attenuation factors. As illustrated in Table 2-1, we have to distinguish between two major dipole orientations—a normal orientation $\mathbf{p}_1$ and a tangential orientation $\mathbf{p}_2$—to be capable of describing the radiated field of our basic dipole orientations of Fig. 2-3. The defined factors are based on P. Bannister's solution [Ban84a, Ban84b] of the Sommerfeld problem and are limited to media with $|n^2| \geq 10$ in general.

Normal dipole $\mathbf{p}_1$, attenuation factors of the electric field components:

$$N_{1,\rho}^{\mathrm{E}} = \frac{1}{\gamma_0^2 \rho^2} \Big\{ \left(3 + 3\gamma_0 R_0 + \gamma_0^2 R_0^2\right) \sin(\psi_0) \cos^4(\psi_0) e^{-\gamma_0 R_0} + \\ + \left(3 + 3\gamma_0 R_1 + \Gamma_{\|} \gamma_0^2 R_1^2\right) \sin(\psi_1) \cos^4(\psi_1) e^{-\gamma_0 R_1} + \\ - \frac{2\rho\gamma_1}{n^2} \cos^3(\psi_1) e^{-\gamma_0 R_1} \left[1 + \left(\frac{1 - \Gamma_{\|}}{2} \right) F(w) \gamma_0 R_1 \right] \Big\} \tag{C1.4}$$

$$N_{1,\phi}^{\mathrm{E}} = 0 \tag{C1.5}$$

$$N_{1,z}^{\mathrm{E}} = \frac{-1}{\gamma_0^2 \rho^2} \Big\{ \left[\left(1 - 3\sin^2(\psi_0)\right)\left(1 + \gamma_0 R_0\right) + \gamma_0^2 R_0^2 \cos^2(\psi_0) \right] \cos^3(\psi_0) e^{-\gamma_0 R_0} + \\ + \left[\left(1 - 3\sin^2(\psi_1)\right)\left(1 + \gamma_0 R_1\right) + \Gamma_{\|} \gamma_0^2 R_1^2 \cos^2(\psi_1) \right] \cos^3(\psi_1) e^{-\gamma_0 R_1} + \\ + \left(1 - \Gamma_{\|}\right) F(w) \gamma_0^2 R_1^2 \cos^5(\psi_1) e^{-\gamma_0 R_1} \Big\} \tag{C1.6}$$

Normal dipole, attenuation factors of the magnetic field components:

$$N_{1,\rho}^{\mathrm{H}} = 0 \tag{C1.7}$$

$$\begin{aligned} N_{1,\phi}^{\mathrm{H}} = \frac{1}{\gamma_0 \rho} \Big\{ & \left(1 + \gamma_0 R_0\right) \cos^3(\psi_0) e^{-\gamma_0 R_0} + \\ & - \left(1 + \Gamma_{\|} \gamma_0 R_1\right) \cos^3(\psi_1) e^{-\gamma_0 R_1} + \\ & + \left(1 - \Gamma_{\|}\right) F(w) \gamma_0 R_1 \cos^3(\psi_1) e^{-\gamma_0 R_1} \Big\} \end{aligned} \tag{C1.8}$$

$$N_{1,z}^{\mathrm{H}} = 0 \tag{C1.9}$$

Tangential dipole **p**₂, attenuation factors of the electric field components:

$$\begin{aligned} N_{2,\rho}^{\mathrm{E}} = \frac{1}{\gamma_0^2 \rho^2} \Big\{ & \Big[\left(3\cos^2(\psi_0) - 1\right)\left(1 + \gamma_0 R_0\right) - \gamma_0^2 R_0^2 \sin^2(\psi_0) \Big] \cos^3(\psi_0) e^{-\gamma_0 R_0} + \\ & - \Big[\left(3\cos^2(\psi_1) - 1\right)\left(1 + \gamma_0 R_1\right) - \Gamma_{\|} \gamma_0^2 R_1^2 \sin^2(\psi_1) \Big] \cos^3(\psi_1) e^{-\gamma_0 R_1} + \\ & + \frac{2}{n^2} \left[1 - \gamma_1 R_1 \sin(\psi_1) + \gamma_0 R_1 + \left(\frac{1 - \Gamma_{\|}}{2} \right) F(w) \gamma_0^2 R_1^2 \right] \cos^3(\psi_1) e^{-\gamma_0 R_1} \Big\} \end{aligned} \tag{C1.10}$$

$$\begin{aligned} N_{2,\phi}^{\mathrm{E}} = \frac{1}{\gamma_0^2 \rho^2} \Big\{ & \left(1 + \gamma_0 R_0 + \gamma_0^2 R_0^2\right) \cos^3(\psi_0) e^{-\gamma_0 R_0} + \\ & - \left(1 + \gamma_0 R_1 + \gamma_0^2 R_1^2\right) \cos^3(\psi_1) e^{-\gamma_0 R_1} + \\ & + \frac{2}{n^2} \Big[\left(2 + \gamma_1 R_1 \sin(\psi_1)\right) + \gamma_0 R_1 \left(1 + A + \gamma_1 R_1 \sin(\psi_1)\right) + \\ & \qquad - \sin^2(\psi_1) \left(3 + 3\gamma_0 R_1 + \gamma_0^2 R_1^2\right) \Big] \cos^3(\psi_1) e^{-\gamma_0 R_1} \Big\} \end{aligned} \tag{C1.11}$$

$$
\begin{aligned}
N_{2,z}^{\mathrm{E}} = \frac{1}{\gamma_0^2\rho^2}\Big\{ & \left(3+3\gamma_0 R_0+\gamma_0^2 R_0^2\right)\sin(\psi_0)\cos^4(\psi_0)e^{-\gamma_0 R_0} + \\
& -\left(3+3\gamma_0 R_1+\Gamma_{\|}\gamma_0^2 R_1^2\right)\sin(\psi_1)\cos^4(\psi_1)e^{-\gamma_0 R_1} + \\
& +\frac{2\rho\gamma_1}{n^2}\left[1+\left(\frac{1-\Gamma_{\|}}{2}\right)F(w)\gamma_0 R_1\right]\cos^3(\psi_1)e^{-\gamma_0 R_1}\Big\}
\end{aligned}
\tag{C1.12}
$$

Tangential dipole **p**2, attenuation factors of the magnetic field components:

$$
\begin{aligned}
N_{2,\rho}^{\mathrm{H}} = \frac{-1}{\gamma_0\rho}\Big\{ & \left(1+\gamma_0 R_0\right)\sin(\psi_0)\cos^2(\psi_0)e^{-\gamma_0 R_0} + \\
& -\left(1+\gamma_0 R_1\right)\sin(\psi_1)\cos^2(\psi_1)e^{-\gamma_0 R_1} + \\
& -\frac{2}{\gamma_1 R_1}\left[2+\gamma_0 R_1\left(1+A\right)-\sin^2(\psi_1)\left(3+3\gamma_0 R_1+\gamma_0^2 R_1^2\right)\right]\cos^2(\psi_1)e^{-\gamma_0 R_1}\Big\}
\end{aligned}
\tag{C1.13}
$$

$$
\begin{aligned}
N_{2,\phi}^{\mathrm{H}} = \frac{-1}{\gamma_0\rho}\Big\{ & \left(1+\gamma_0 R_0\right)\sin(\psi_0)\cos^2(\psi_0)e^{-\gamma_0 R_0} + \\
& -\left(1+\Gamma_{\|}\gamma_0 R_1\right)\sin(\psi_1)\cos^2(\psi_1)e^{-\gamma_0 R_1} + \\
& +\frac{2}{\gamma_1 R_1}\left[1+\gamma_0 R_1+\left(\frac{1-\Gamma_{\|}}{2}\right)F(w)\gamma_0^2 R_1^2\right]\cos^2(\psi_1)e^{-\gamma_0 R_1}\Big\}
\end{aligned}
\tag{C1.14}
$$

$$
\begin{aligned}
N_{2,z}^{\mathrm{H}} = \frac{1}{\gamma_0\rho}\Big\{ & \left(1+\gamma_0 R_0\right)\cos^3(\psi_0)e^{-\gamma_0 R_0} + \\
& -\left(1+\gamma_0 R_1\right)\cos^3(\psi_1)e^{-\gamma_0 R_1} + \\
& +\frac{2}{\left(\gamma_1^2-\gamma_0^2\right)R_1^2}\Big[\left(1+\gamma_1 R_1\sin(\psi_1)\right)\left(3+3\gamma_0 R_1+\gamma_0^2 R_1^2\right) + \\
& -\sin^2(\psi_1)\left(15+15\gamma_0 R_1+6\gamma_0^2 R_1^2+\gamma_0^3 R_1^3\right)\Big]\cos^3(\psi_1)e^{-\gamma_0 R_1}\Big\}
\end{aligned}
\tag{C1.15}
$$

Appendix D

D1 Recursive Field Components of the FDTD Method

Corresponding to [Gus06], the recursive functions of the electric field values are

$$\begin{aligned} E^{n+1}_{x,i+\frac{1}{2},j,k} &= \left(\frac{1-\dfrac{\sigma_x \Delta t}{2\varepsilon_x}}{1+\dfrac{\sigma_x \Delta t}{2\varepsilon_x}} \right) E^{n}_{x,i+\frac{1}{2},j,k} + \\ &+ \left(\frac{\dfrac{\Delta t}{\varepsilon_x}}{1+\dfrac{\sigma_x \Delta t}{2\varepsilon_x}} \right) \left(\frac{H^{n+\frac{1}{2}}_{z,i+\frac{1}{2},j+\frac{1}{2},k} - H^{n+\frac{1}{2}}_{z,i+\frac{1}{2},j-\frac{1}{2},k}}{\Delta y} - \frac{H^{n+\frac{1}{2}}_{y,i+\frac{1}{2},j,k+\frac{1}{2}} - H^{n+\frac{1}{2}}_{y,i+\frac{1}{2},j,k-\frac{1}{2}}}{\Delta z} \right), \end{aligned} \tag{D1.16}$$

$$\begin{aligned} E^{n+1}_{y,i,j+\frac{1}{2},k} &= \left(\frac{1-\dfrac{\sigma_y \Delta t}{2\varepsilon_y}}{1+\dfrac{\sigma_y \Delta t}{2\varepsilon_y}} \right) E^{n}_{y,i,j+\frac{1}{2},k} + \\ &+ \left(\frac{\dfrac{\Delta t}{\varepsilon_y}}{1+\dfrac{\sigma_y \Delta t}{2\varepsilon_y}} \right) \left(\frac{H^{n+\frac{1}{2}}_{x,i,j+\frac{1}{2},k+\frac{1}{2}} - H^{n+\frac{1}{2}}_{x,i,j+\frac{1}{2},k-\frac{1}{2}}}{\Delta z} - \frac{H^{n+\frac{1}{2}}_{z,i+\frac{1}{2},j+\frac{1}{2},k} - H^{n+\frac{1}{2}}_{z,i-\frac{1}{2},j+\frac{1}{2},k}}{\Delta x} \right), \end{aligned} \tag{D1.17}$$

$$\begin{aligned} E^{n+1}_{z,i,j,k+\frac{1}{2}} &= \left(\frac{1-\dfrac{\sigma_z \Delta t}{2\varepsilon_z}}{1+\dfrac{\sigma_z \Delta t}{2\varepsilon_z}} \right) E^{n}_{z,i,j,k+\frac{1}{2}} + \\ &+ \left(\frac{\dfrac{\Delta t}{\varepsilon_z}}{1+\dfrac{\sigma_z \Delta t}{2\varepsilon_z}} \right) \left(\frac{H^{n+\frac{1}{2}}_{y,i+\frac{1}{2},j,k+\frac{1}{2}} - H^{n+\frac{1}{2}}_{y,i-\frac{1}{2},j,k+\frac{1}{2}}}{\Delta x} - \frac{H^{n+\frac{1}{2}}_{x,i,j+\frac{1}{2},k+\frac{1}{2}} - H^{n+\frac{1}{2}}_{x,i,j-\frac{1}{2},k+\frac{1}{2}}}{\Delta y} \right). \end{aligned} \tag{D1.18}$$

And the recursive functions of the magnetic field values are

$$H^{n+\frac{1}{2}}_{x,i,j+\frac{1}{2},k+\frac{1}{2}} = H^{n-\frac{1}{2}}_{x,i,j+\frac{1}{2},k+\frac{1}{2}} + \tag{D1.19}$$
$$-\frac{\Delta t}{\mu_x}\left(\frac{E^n_{y,i,j+\frac{1}{2},k+1} - E^n_{y,i,j+\frac{1}{2},k}}{\Delta z} - \frac{E^n_{z,i,j+1,k+\frac{1}{2}} - E^n_{z,i,j,k+\frac{1}{2}}}{\Delta y}\right),$$

$$H^{n+\frac{1}{2}}_{y,i+\frac{1}{2},j,k+\frac{1}{2}} = H^{n-\frac{1}{2}}_{y,i+\frac{1}{2},j,k+\frac{1}{2}} + \tag{D1.20}$$
$$-\frac{\Delta t}{\mu_y}\left(\frac{E^n_{z,i+1,j,k+\frac{1}{2}} - E^n_{z,i,j,k+\frac{1}{2}}}{\Delta x} - \frac{E^n_{x,i+\frac{1}{2},j,k+1} - E^n_{x,i+\frac{1}{2},j,k}}{\Delta z}\right),$$

$$H^{n+\frac{1}{2}}_{z,i+\frac{1}{2},j+\frac{1}{2},k} = H^{n-\frac{1}{2}}_{z,i+\frac{1}{2},j+\frac{1}{2},k} + \tag{D1.21}$$
$$-\frac{\Delta t}{\mu_z}\left(\frac{E^n_{x,i+\frac{1}{2},j+1,k} - E^n_{x,i+\frac{1}{2},j,k}}{\Delta y} - \frac{E^n_{y,i+1,j+\frac{1}{2},k} - E^n_{y,i,j+\frac{1}{2},k}}{\Delta x}\right).$$

Bibliography

[Abb12] Q. H. Abbasi, A. Sani, A. Alomainy, and Y. Hao, “Numerical Characterization and Modeling of Subject-Specific Ultrawideband Body-Centric Radio Channels and Systems for Healthcare Applications,” *Information Technology in Biomedicine, IEEE Transactions on*, Vol. 16, No. 2, pp. 221–227, March 2012.

[Akh10] L. Akhoondzadeh-Asl, P. S. Hall, and Y. Nechayev, “Wave excitation on human body by a short dipole,” *Antennas and Propagation (EuCAP), 2010 Proceedings of the Fourth European Conference on*, 12–16 April 2010.

[Alv11] T. Alves, B. Poussot and J. M. Laheurte, “Analytical Propagation Modeling of BAN Channels Based on the Creeping-Wave Theory,” in *IEEE Transactions on Antennas and Propagation*, Vol. 59, No. 4, pp. 1269–1274, April 2011.

[Bal89] C.A. Balanis, *Advanced Engineering Electromagnetics*, Hoboken, NJ, USA: Wiley, 1989.

[Bal05] C.A. Balanis, *Antenna Theory–Analysis and Design, 3rd ed.* Hoboken, NJ, USA: Wiley, 2005.

[Ban78] P. R. Bannister, “Extension of Quasi-Static Range Finitely Conducting Earth Image Theory Techniques to Other Ranges,” in *IEEE Transactions on Antennas and Propagation*, Vol. AP-26, No. 3, pp. 507–508, 1978.

[Ban79] P. R. Bannister, “Summary of the Image-Theory Expressions for the Quasi-Static Fields of Antennas at or Above the Earth’s Surface,” in *Proceedings IEEE*, Vol. 67, No. 7, pp. 1001–1008., 1979.

[Ban80] P. R. Bannister et al., “Quasi-Static Electromagnetic Fields,” *NUSC Scientific and Engineering Studies*, Naval Underwater System Center, New London, CT, pp. 515, 1980.

[Ban81] P. R. Bannister et al., “Image Theory EM Fields of Horizontal Dipole Antennas in Presence of Conducting Half-Space,” *NUSC Technical Report 6511*, Naval Underwater System Center, New London, CT, Sep. 1981.

[Ban82] P. R. Bannister et al., “The Image Theory EM Fields of Horizontal Dipole Antennas in Presence of a Conducting Half-Space,” *Radio Science*, Vol. 17, No. 5, pp. 1095–1102, 1982.

[Ban84a] P. R. Bannister, “New Formulas That Extend Norton’s Farfield Elementary Dipole Equation to the Quasi-Nearfield Range,” in *NUSC Technical Report 6883*, Naval Underwater Systems Center, New London, CT, 1984.

[Ban84b] P. R. Bannister, “Extension of Finitely Conducting Earth-Image-Theory Results to any Range,” in *NUSC Technical Report 6885*, Naval Underwater Systems Center, New London, CT, 1984.

[Ber14] M. Berg, T. Tuovinen, and E.T. Salonen, “Low-profile antenna with optimal polarization for 2.45 GHz on-body sensor nodes,” *Antennas and Propagation Conference (LAPC), 2014 Loughborough*, pp. 641–643, 10–11 Nov. 2014.

[Cha12] N. Chahat, M. Zhadobov, L. Le Coq, and R. Sauleau, “Wearable Endfire Textile Antenna for On-Body Communications at 60 GHz,” in *Antennas and Wireless Propagation Letters, IEEE*, Vol. 11, pp. 799–802, 2012.

[Cha13] N. Chahat, G. Valerio, M. Zhadobov, and R. Sauleau, “On-Body Propagation at 60 GHz,” Antennas and Propagation, in *IEEE Transaction on*, Vol. 61, No. 4, pp. 1876–1888, April 2013.

[Che90] W.C. Chew, *Waves and Fields in Inhomogeneous Media*, Van Nostrand Reinhold, NY, USA, 1990.

[Chr10] A. Christ, W. Kainz, E. G. Hahn, K. Honegger, M. Zefferer, E. Neufeld, W. Rascher, R. Janka, W. Bautz, J. Chen, B. Kiefer, P. Schmitt, H. Hollenbach, J. Shen, M. Oberle, D. Szczerba, A. Kam, J. W. Guag and N. Kuster, "The Virtual Family—development of surface-based anatomical models of two adults and two children for dosimetric simulations," in *Physics in Medicine and Biology*, Vol. 55, Issue 2, pp. N23–N38, January 2010.

[EMP] EMPIRE XCcel website, [Online], Available: http://www.empire.de

[For10] A. Fort, F. Keshmiri, G. R. Crusats, C. Craeye, C. Oestges, "A Body Area Propagation Model Derived From Fundamental Principles: Analytical Analysis and Comparison With Measurements," in *Antennas and Propagation, IEEE Transactions on*, Vol. 58, No. 2, pp. 503–514, Feb. 2010.

[Gab96a] C. Gabriel, S. Gabriel and E. Corthout: "The dielectric properties of biological tissues: I. Literature survey," *Phys. Med. Biol.* Vol. 41, pp. 2231–2249, 1996.

[Gab96b] S. Gabriel, R. W. Lau and C. Gabriel: "The dielectric properties of biological tissues: II. Measurements in the frequency range 10 Hz to 20 GHz," *Phys. Med. Biol.* Vol. 41, pp. 2251–2269, 1996.

[Gab96c] S. Gabriel, R. W. Lau and C. Gabriel: "The dielectric properties of biological tissues: III. Parametric models for the dielectric spectrum of tissues," *Phys. Med. Biol.* Vol. 41, pp. 2271–2293, 1996.

[Gal11] M. Gallo, P. S. Hall, Q. Bai, Y. I. Nechayev, C. C. Constantinou, and M. Bozzetti, "Simulation and Measurement of Dynamic On-Body Communication Channels," in *Antennas and Propagation, IEEE Transactions on* , Vol. 59, No. 2, pp. 623–630, Feb. 2011.

[Gos14] M. Gosselin, E. Neufeld, H. Moser, E. Huber, S. Farcito, L. Gerber, M. Jedensj, I. Hilber, F. Di Gennaro, B. Lloyd, E. Cherubini, D. Szczerba, W. Kainz and N. Kuster, "Development of a new generation of high-resolution anatomical models for medical device evaluation: the Virtual Population 3.0," in *Physics in Medicine and Biology*, Vol. 59, Issue 18, pp. 5287–5303, June 2014.

[Gri10] M. Grimm, and D. Manteuffel, "Electromagnetic wave propagation on human trunk models excited by half-wavelength dipoles," in *Antennas and Propagation Conference (LAPC), 2010 Loughborough*, pp. 493–496, 8–9 Nov. 2010.

[Gri11] M. Grimm, and D. Manteuffel, "Characterization of Electromagnetic Propagation Effects in the Human Head and its Application to Deep Brain Implants," *International Conference on Electromagnetics in Advanced Applications–Antennas and Propagation in Wireless Communications 2011* (ICEAA-IEEE APWC 2011), Torino, Italy, September 2011.

[Gri12a] M. Grimm, and D. Manteuffel, "Evaluation of the Norton equations for the development of body-centric propagation models," *6th European Conference on Antennas and Propagation (EUCAP)*, Prague, Czech Republic, pp. 311-315, 2012.

[Gri12b] D. Manteuffel, and M. Grimm, "On- and in-body path loss models based on antenna de-embedding," *International Conference on Electromagnetics in Advanced Applications—Antennas and Propagation in Wireless Communications 2012* (ICEAA-IEEE APWC 2012), Cape Town, South Africa, September 2012.

[Gri13a] M. Grimm, and D. Manteuffel, "Discussion of Body Worn Dipole Antennas Based on an Improved De-embedding Approach," *In Antennas and Propagation (EUCAP), 2013 7th European Conference on*, Gothenburg, Sweden, 8-12 April 2013.

[Gri13b] M. Grimm and D. Manteuffel, "Antennas and Propagation for On-, Off- and In-Body Communications," in R.S. Thomä, H. I. Willms, T. Zwick, R. Knöchel, and J. Sachs, *UKoLoS—Ultra-Wideband Radio Technologies for Communications, Localization and Sensor Applications*, InTech, Ch. 7, 2013.

[Gri14a] M. Grimm, and D. Manteuffel, "Far Field Modeling of Body Worn Antennas by the Superposition of Equivalent Electric Sources," in *Antennas and Propagation (EUCAP), 2014 8th European Conference on.*, The Hague, The Netherlands, pp. 1754–1755, April 2014.

[Gri14b] M. Grimm, and D. Manteuffel, "Norton Surface Waves in the Scope of Body Area Networks," in *Antennas and Propagation, IEEE Transaction on*, Vol. 62, No. 5, pp. 2616–2623, May 2014.

[Gri14c] M. Grimm, D. Manteuffel, "Body worn antenna system for health care related on- and off-body communications," *Wireless Mobile Communication and Healthcare (Mobihealth), 2014 EAI 4th International Conference on*, pp. 203–206, 3–5 Nov. 2014.

[Gri15a] M. Grimm, and D. Manteuffel, "On-body far field description by two equivalent electric sources," in *Antennas and Propagation & USNC/URSI National Radio Science Meeting, 2015 IEEE International Symposium on*, pp. 1068–1069, 19–24 July 2015.

[Gri15b] M. Grimm, and D. Manteuffel, "On-Body Antenna Parameters," in *Antennas and Propagation, IEEE Transactions on*, Vol. 63, No. 12, pp. 5812–5821, Dec. 2015.

[Gus06] F. Gustrau, D. Manteuffel: *EM Modeling of Antennas and RF Components for Wireless Communication Systems*, Springer, 1. Auflage, Berlin, 2006.

[Hal06] P. S. Hall, and Y. Hao, *Antennas and Propagation for Body-Centric Wireless Communications*, ISBN 9781580534932, Artech House, 2006.

[Hal10] P. S. Hall, Y. Hao, and S. L. Cotton, "Advances in antennas and propagation for body centric wireless communications," *Antennas and Propagation (EuCAP), 2010 Proceedings of the Fourth European Conference on*, 12–16 April 2010.

[IAP] An Internet Resource for the Calculation of the Dielectric Properties of Body Tissues, The Institute for Applied Physics, Italian National Research Council website. [Online]. Available: http://niremf.ifac.cnr.it/tissprop/

[Iee98] *IEEE Standard Definitions of Terms for Radio Wave Propagation*, IEEE Std 211–1997, 1998.

[ITI] IT'IS Foundation website, [Online]. Whole-Body Human Models, Enhanced Anatomical Models, Available: http://www.itis.ethz.ch/

[Lea09] A. Lea, Ping Hui, J. Ollikainen, and R. G. Vaughan, "Propagation Between On-Body Antennas," in *Antennas and Propagation, IEEE Transactions on*, Vol. 57, No. 11, pp. 3619–3627, Nov. 2009.

[Mic16] K. A. Michalski, and J. R. Mosig, "The Sommerfeld half-space problem revisited: from radio frequencies and Zanneck waves to visible light and Fano modes," *Journal of Electromagnetic Waves and Applications*, Vol. 30, Issue 1, pp. 1–42, 2016.

[Nor37] K. A. Norton, "The Propagation of Radio Waves Over the Surface of the Earth," in *Proceedings of the IRE*, Vol. 24, 1936, pp. 1367–1387; Vol. 25, 1937, pp. 1203–1236.

[Nor41] K. A. Norton, "The Calculation of Ground-Wave Field Intensity over a Finitely Conducting Spherical Earth," in *Proceedings of the IRE*, Vol. 29, No. 12, pp. 623–639, Dec. 1941.

[Pel12] A. Pellegrini, A. Brizzi, L. Zhang, and Y. Hao, "Numerical and experimental analysis of the on-body propagation channel at W band," *Antennas and Propagation (EUCAP), 2012 6th European Conference on*, pp. 750–754, 26–30 March 2012.

[Som09] A. Sommerfeld, “Über die Ausbreitung der Wellen in der drahtlosen Telegraphie,” *Annalen der Physik*, Vol. 28, Issue 4, pp. 665–736, 1909.

[Som26] A. Sommerfeld, “Über die Ausbreitung der Wellen in der drahtlosen Telegraphie,” in *Annalen der Physik*, Vol. 28, pp. 665–737, 1909; Vol. 81, pp. 1135–1153, 1926.

[Str41] J. A. Stratton, *Electromagnetic Theory*, McGraw-Hill Book Company, New York and London, 1941.

[Wai60] J. Wait, “On the excitation of electromagnetic surface waves on a curved surface,” in *IRE Transactions on Antennas and Propagation*, Vol. 8, No. 4, pp. 445–448, July 1960.

[Wai61] J. R. Wait, “The Electromagnetic Fields of a Horizontal Dipole in the Presence of a Conducting Half-Space.” *Canadian Journal of Physics*, Vol. 39, pp. 1017–1028, 1961.

[Wai96] J. R. Wait, *Electromagnetic Waves in Stratified Media*, New York, Pergamon Press, first edition 1962; second enlarged edition 1970; first edition reprinted by IEEE Press 1996, ISBN 9780198592235.

[Wai98] J. R. Wait, “The ancient and modern history of EM ground-wave propagation,” in *Antennas and Propagation Magazine, IEEE*, Vol. 40, No. 5, pp. 7–24, Oct 1998.

[Wey19] H. Weyl, “The Propagation of Electromagnetic Waves Over a Plane Conductor,” *Annalen der Physik*, Vol. 60, pp. 481–500, 1919.

[Wu10] X. Y. Wu, L. Akhoondzadeh-Asl, Z. P. Wang, and P. S. Hall, “Novel Yagi-Uda Antennas for On-Body Communication at 60GHz,” *Antennas and Propagation Conference, Loughborough*, pp. 153–156, 2010.

Curriculum Vitae

Personal Details

Name: Markus Grimm

Date of Birth: 22th November, 1980 in Neumünster (Germany)

Nationality: German

Education

2001 – 2010	Diploma in Electrical Engineering and Information Technology, University of Kiel, Kiel, Germany
2010 – 2015	Research assistant, Working Group of Wireless Communications, University of Kiel, Kiel, Germany
Since 2016	PhD Student, Institute of Microwave and Wireless Systems, Leibniz University Hannover, Hanover, Germany

Additional Qualifications

2010	Project to initialize an EM anechoic chamber, Working Group of Wireless Communications, University of Kiel, Kiel, Germany
2011	Participation at ESoA (European Scholl of Antennas), Queen Mary, University of London, London, United Kingdom